CRUSTAL STRUCTURE OF THE SOUTH FLORIDA BANK DERIVED FROM OCEAN BOTTOM SEISMOMETER REFRACTION PROFILES

Joseph O. Ebeniro
and
William P. O'Brien, Jr.

Institute for Geophysics
The University of Texas at Austin
4920 North IH 35
Austin, Texas 78751

(512) 451-6223

May 1, 1984

This is the final report on refraction experiments that were part of the **SOUTH FLORIDA BANK STUDY**, a project funded under Joint Industry sponsorship.

Principal Investigator: F. Jeanne Shaub

Co-Investigators: Paul L. Donoho
Richard T. Buffler

University of Texas Institute for Geophysics
Technical Report No. 32

ABSTRACT

In March 1982, six seismic refraction lines, 70 to 90 km long, were shot in the southeastern Gulf of Mexico using the advanced Texas digital ocean bottom seismometers. Five lines were on the South Florida bank region in water depths of less than one kilometer and one was in water depth of about 2.4 km off the northern coast of Cuba. After data reduction, first arrival picks were made and least-square lines were fitted to the picks to obtain the apparent velocities and intercept times for the layers. Using these values, flat-layer crustal models have been computed. The two most dominant refractors have apparent velocities of 5.6-5.9 km/sec and 6.2-6.6 km/sec. The top of the 5.6-5.9 km/sec layer varies in depth from 2-5 km below the sea surface and is interpreted to represent the crystalline basement. Alternatively, this layer may constitute a carbonate section with velocities indistinguishable from crustal velocities. Basement rock, at a depth of 3.4 km, was overlain by various carbonate facies in a well in the Pinellas County arch. In the South Florida bank area, the deepest refractor observed has an apparent velocity of about 7.5 km/sec at a depth of 25 km. The absence of any interpretable mantle arrivals in these long refraction profiles on the platform suggests that the crust underlying the South Florida bank platform is continental in nature. Possible mantle arrivals were seen at the ends of the line off the northern coast of Cuba (apparent velocities and depths: 7.7 km/sec and 21 km at the northern end and 8.4 km/sec and 26 km at the southern end), suggesting a mantle that dips strongly to the south towards Cuba. Similar crustal thickness has been observed in a refraction profile just northwest of this line. This deep crust structure compliments the earlier shallow crust structures for this area.

TABLE OF CONTENTS

Introduction 1

Equipment 1

Field Operations 7

Data Processing and Reduction 7

Data Interpretation 12
- Line 1 12
- Line 2 12
- Line 3 15
- Line 4 15
- Line 5 15
- Line 6 19

Regional Synthesis 19

Discussion 23

Conclusions 26

Recommendations 28

Acknowledgments 29

References 30

Appendices
- A Track and Bathymetry for each Line with Shot Coordinates 32
- B Filtered Record Sections 51
- C Tables of Arrival Picks and Travel-time Curves 68
- D Interpreted Velocity-depth Profiles 81

INTRODUCTION

A refraction study using explosives and digital ocean bottom seismometers (OBS) was conducted in the southeastern Gulf of Mexico off south Florida in March of 1982. Six lines (each approximately 90 km long) were shot in the area (Figure 1 and Table 1) using three OBS units per line; four of the lines (Lines 1-4) were on the shelf, one (Line 5) was on the shelf/slope margin and one (Line 6) was in the Florida Straits near Cuba.

The South Florida Bank is a massive submerged carbonate platform of Mesozoic-Cenozoic age that is believed to be the result of slow subsidence that took place from the Jurassic to the Lower Eocene in a restricted shallow water basin. This region historically has been difficult to study using ordinary multichannel seismic reflection techniques because of poor energy penetration and strong back scattering compounded by trapping of low-frequency energy in the shallow near bottom sedimentary layer. Only a limited amount of refraction data has been published for the area (Antoine and Ewing, 1963). In this report we present the OBS refraction data detected by the vertical-component 4.5 Hz geophones and give a regional interpretation.

EQUIPMENT

The digital OBS used in these experiments (Figure 2; Latham et al., 1978; Steinmetz et al.,1979; Nakamura, 1983) consisted of a triaxial geophone system with recording and control electronics housed in a glass sphere 43 cm in diameter that was secured firmly in a heavy square spiked metal frame about 1.2 m on each side. The sensor system consisted of one vertical and two horizontal geophones. A special unit which contained 3 vertical geophones was used as OBS 1 on the first four lines (1-4). The natural frequencies of these geophones were 2.0, 4.5 and 10.0 Hz. The frequency of the vertical-component geophones in all the other units was 4.5 Hz, and the frequency of all horizontal-component geophones was 10.0 Hz.

At deployment, an OBS in its spiked frame was released from the sea surface and allowed to fall to the sea bottom. The spiked frame was designed to firmly lodge in the sea floor upon impact, thus providing good coupling between ground motion and the OBS geophones. Each unit contained electronic clocks and three microprocessors programmed to activate the instrument at a specific time for each shot to detect, digitize and multiplex up to 90 seconds of 3-component data and then to record it on a 4-track cartridge tape. Reference timing information for each OBS was provided by the internal clock which was calibrated against WWV immediately before each deployment and immediately after each recovery. The sampling rate of the instrument was approximately 136 samples/sec (sample interval = 7.344 ms), and the dynamic range was about 96 dB. All OBS units possessed an externally-mounted compass, whose needle locked into place several hours after the OBS reached bottom, allowing us to determine the

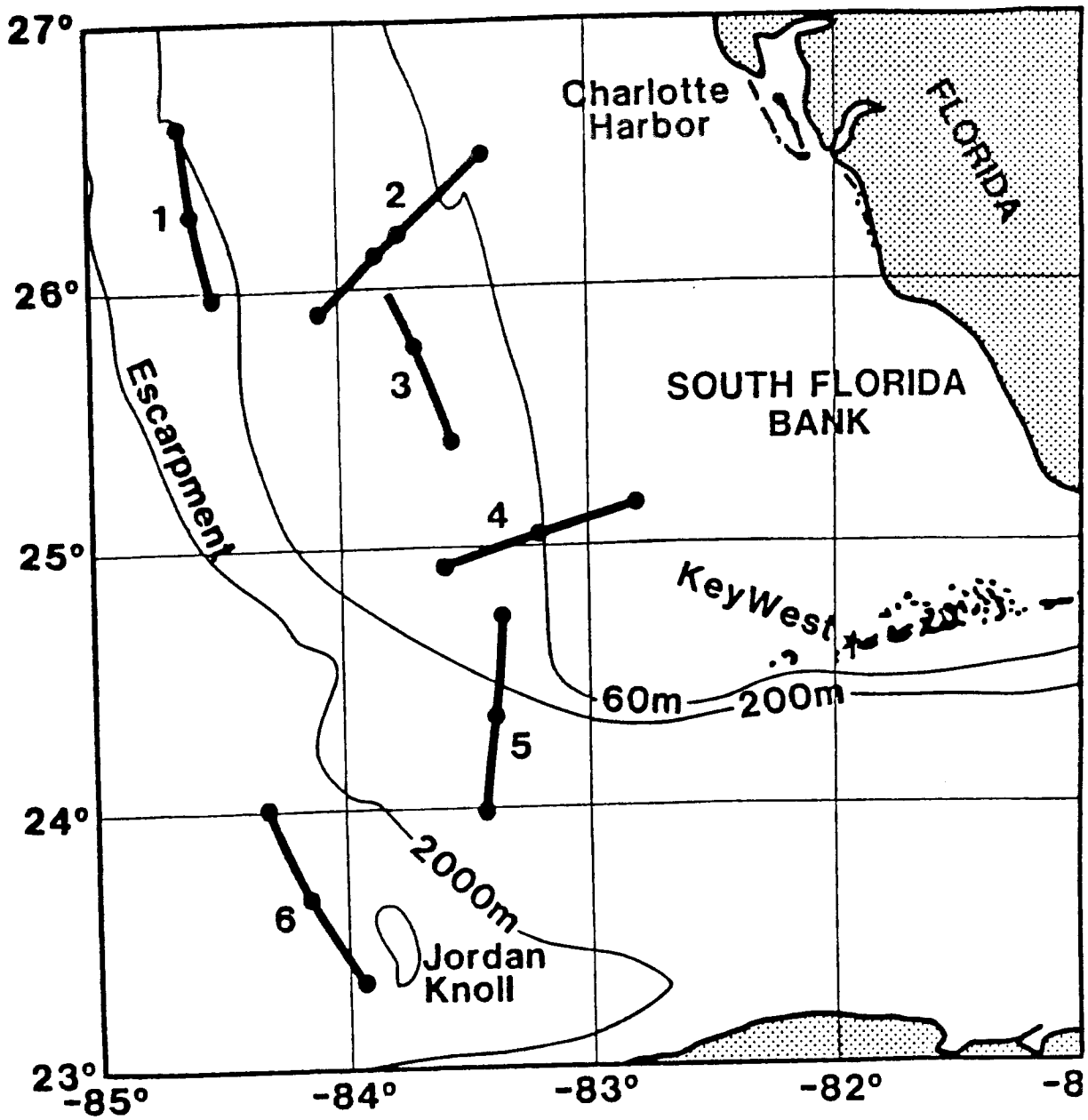

Figure 1. Map of the Southeastern Gulf of Mexico showing the position of the six refraction lines. Large dots indicate the positions of the Ocean Bottom Seismometers (OBS) used in the experiment.

TABLE 1. Summary of all OBS locations and water depths

LINE	OBS	LATITUDE(N)	LONGITUDE(W)	WATER DEPTH(m)
1	1	26°36.10'	84°38.10'	210
	2	26°16.51'	84°34.56'	216
	3	25°57.97'	84°30.89'	214
2	1	25°54.87'	84°03.95'	144
	2	26°12.12'	83°44.55'	75
	3	26°28.81'	83°24.76'	55
3	1	26°07.68'	83°50.01'	99
	2	25°46.39'	83°41.09'	77
	3	25°25.42'	83°32.15'	70
4	1	25°10.07'	82°48.01'	44
	2	25°02.87'	83°11.08'	57
	3	24°55.71'	83°33.93'	68
5	1	24°42.99'	83°19.99'	62
	2	24°21.00'	83°22.03'	558
	3	23°58.99'	83°24.18'	916
6	1	23°20.05'	83°55.31'	2414
	2	23°40.06'	84°07.84'	2403
	3	23°59.87'	84°19.18'	2398

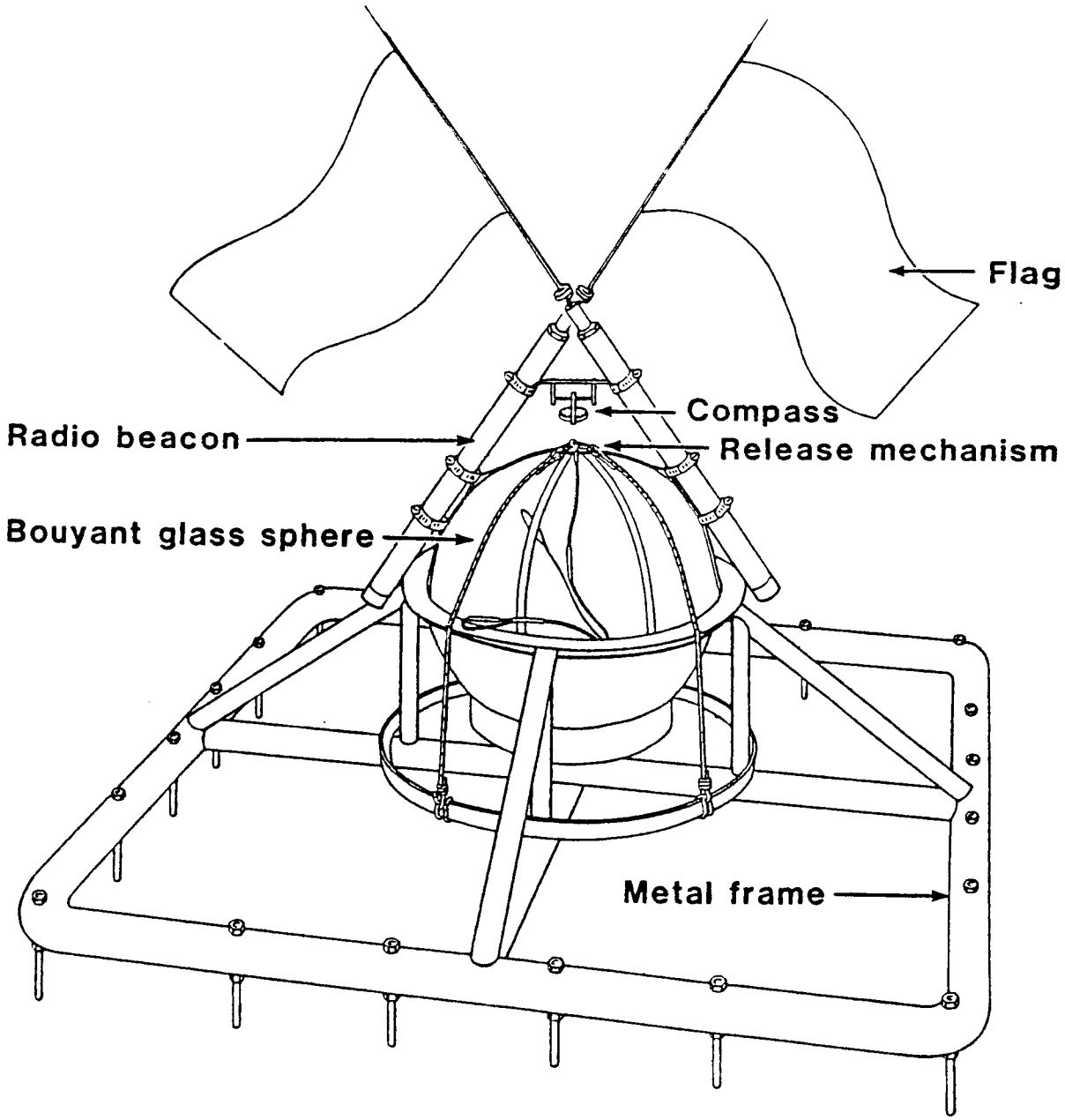

Figure 2. The UTIG OBS used in these experiments mounted in its square spiked anchoring metal frame.

orientation of the two horizontal geophones. Each OBS was programmed so that at the appropriate time an electric current caused the electrochemical dissolution of the stainless steel wire holding the instrument sphere in the heavy frame, allowing the sphere to float to the surface for recovery. Each unit was equipped with strobe lights and two radio beacons that would turn on when the unit surfaced, and small bright flags were attached to the beacon antennas to further aid in locating the surfaced OBS.

The response of the OBS to seafloor motion depends on at least four separate factors: the integrity of the coupling between the OBS frame and the seafloor, the structure and rigidity of the OBS frame itself, the geophone response and the electronic alias filter in the preamplifiers. The output EMF of the geophones used in these experiments was directly proportional to the velocity of ground motion for frequencies above their natural frequency. The EMF generated at frequencies below the natural frequency fell off exponentially with a rolloff of -12 dB/octave. The low-pass alias filter had a corner frequency of about 31 Hz and a rolloff of -24 dB/octave at frequencies above 31 Hz. No resonance tests were made on the frames used in these experiments although a prototype frame was tested extensively (Steinmetz et al., 1979) and found to have its fundamental resonance at 24 Hz. Presumably the frame we used had its resonance frequency above 24 Hz because it was built more rigidly than the prototype frame. The coupling of an OBS frame to the ocean floor is a classic unresolved problem (Sutton et al., 1981).

The unknown coupling factor and the fact that the geophones and electronics were not bench calibrated made it impossible to determine an absolute response for the OBS. The nominal OBS response to ground motion with electronic filter is shown in Figure 3. Note that the passband ranges from the natural frequency to 31 Hz, a broad band which contains most of the signals of interest in this experiment.

The sound sources for each line were 61 explosive shots (DuPont Tovex Extra) ranging in size from 13.6 kg (30 lb) to 81.6 kg (180 lb), which were detonated at five-minute intervals and were distributed (Table 2) so that the largest shots were near the ends of the line.

TABLE 2. Shooting plan used for all lines; the explosive material used was DuPont Tovex Extra.

Shot #	Weight (lb)
1- 6	180
7-28	60
29-34	30
35-55	60
56-61	180

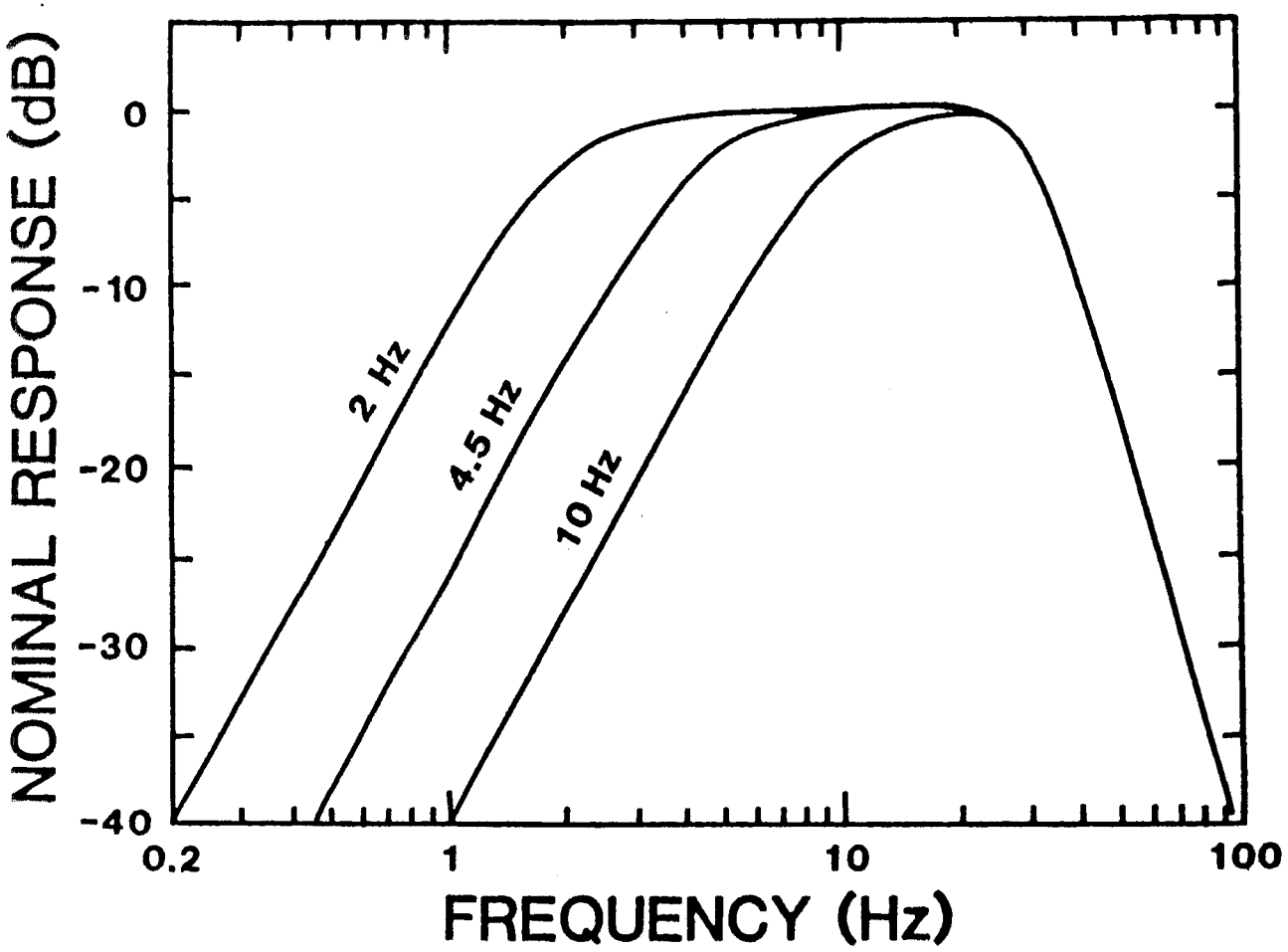

Figure 3. Nominal relative instrument response to ground motion for the geophones and the alais filter of the UTIG OBS units used in the experiment.

FIELD OPERATIONS

The procedure followed for this OBS seismic refraction survey was to deploy three OBS units along a straight line from the R/V Ida Green, then to retrace the line at about 10 knots while dropping explosive charges at five minute intervals (shot-to-shot spacing of about 1.5 km) and finally to recover the surfaced instruments. Bad weather was encountered for Lines 3 and 4 with the result that the shot coverage for Line 3 extended only about 67 km; also on these two lines the Loran-C equipment was unusable at times and we were forced to rely on satellite data for navigation. For the rest of the cruise, however, the distances between each shot and a given OBS and the locations of each OBS were determined using Loran-C navigation data.

Of the 18 OBS units deployed and recovered, 16 recorded useful data; the middle OBS unit (OBS 2) malfunctioned on Lines 1 and 3 and recorded no data. Track lines, bathymetry details and the shot coordinates are shown in Appendix A.

The exact shot times were determined by comparing the recorded signals from a towed hydrophone with the recorded time record from an electronic master clock (calibrated against WWV), taking into account the elapsed time between the actual shot and the detection of the shot by the towed hydrophone. This master clock was also used to determine the drift of each OBS clock during deployment.

DATA PROCESSING AND REDUCTION

The digital data recorded on each 4-track cartridge tape were transferred to 9-track tape in standard SEG-Y trace-sequential format (Barry et al., 1980) incorporating corrections for the shot times and clock drift (discussed above) and the shot-to-hydrophone travel times so that the first sample on each trace (at $t = 0$ sec) corresponded to the actual shot instant. The timing correction for the distance between the shot and the hydrophone was determined using their horizontal separation and the depth of the shot determined from the bubble pulse data using the Rayleigh-Willis equation (Kramer et al., 1968). We used 1.52 km/sec as the velocity of sound in water for these calculations.

The data from the vertical-component geophone of each OBS were analyzed by preparing seismic record sections of all 61 shots. In order to better distinguish the signals from the noise, we experimented with various minimum-phase filters and amplitude scales. For the record sections pictured in this report (see Appendix B), we used a minimum-phase 3-pole Butterworth filter with a 2.5-8 Hz passband, and we scaled all trace amplitudes to a shot-OBS distance

of 10 km and scaled all shot weights to 60 lb using a trace amplitude scale factor (Orcutt et al.; 1976)

$$K = \frac{R}{R_o} \times \left(\frac{W_o}{W}\right)^{0.65} \qquad \text{.....(1)}$$

where R_o = 10 km, W_o= 60 lb, R = shot-OBS distance (km) and W = shot weight (lb).

We made picks of primary and secondary arrivals on the record sections (using both the filtered and gain-applied sections and the raw-data sections) and plotted them versus shot-OBS separation to give travel time curves; tables of the picks and the plotted travel-time curves are given in Appendix C. Points on each curve were fitted (by the method of least squares) to straight line segments from whose slopes and intercepts we calculated the apparent velocities and depths using a flat-layered model of the region.

The application of topographic corrections to refraction data before final reduction improves the accuracy with which the structures, especially the deeper ones, can be deduced. We used the method of topographic correction described by Whitmarsh (1975) and Purdy (1982). For a propagating ray of ray parameter p of a given shot, the time correction δt is defined as the product of a correction coefficient ($\Delta t/\Delta h$) and a distance δh (Figure 4) which is the depth of the reference datum relative to the seafloor at the point where the ray enters the uppermost layer of the crust. That is,

$$\delta t = \text{time correction} = \frac{\Delta t}{\Delta h} \times \delta h \qquad \text{.....(2)}$$

where

$$\frac{\Delta t}{\Delta h} = \frac{(1 - V_w^2 p^2)^{1/2}}{V_w} - \frac{(1 - V_c^2 p^2)^{1/2}}{V_c} \qquad \text{.....(3)}$$

V_w is the water column sounding velocity, V_c is the velocity of the shallowest crust, p is the ray parameter and the distance δh is the vertical distance between the seafloor and the reference datum. The reference datum was chosen to be about halfway between the deepest and the shallowest water depth along the profile line. A major source of error in this correction resides in the choice of the shallowest crustal velocity V_c. Figures 5 and 6 show that the correction coefficient is quite unstable when the ray parameter of the assumed shallow crust is approximately equal to that of the shallowest

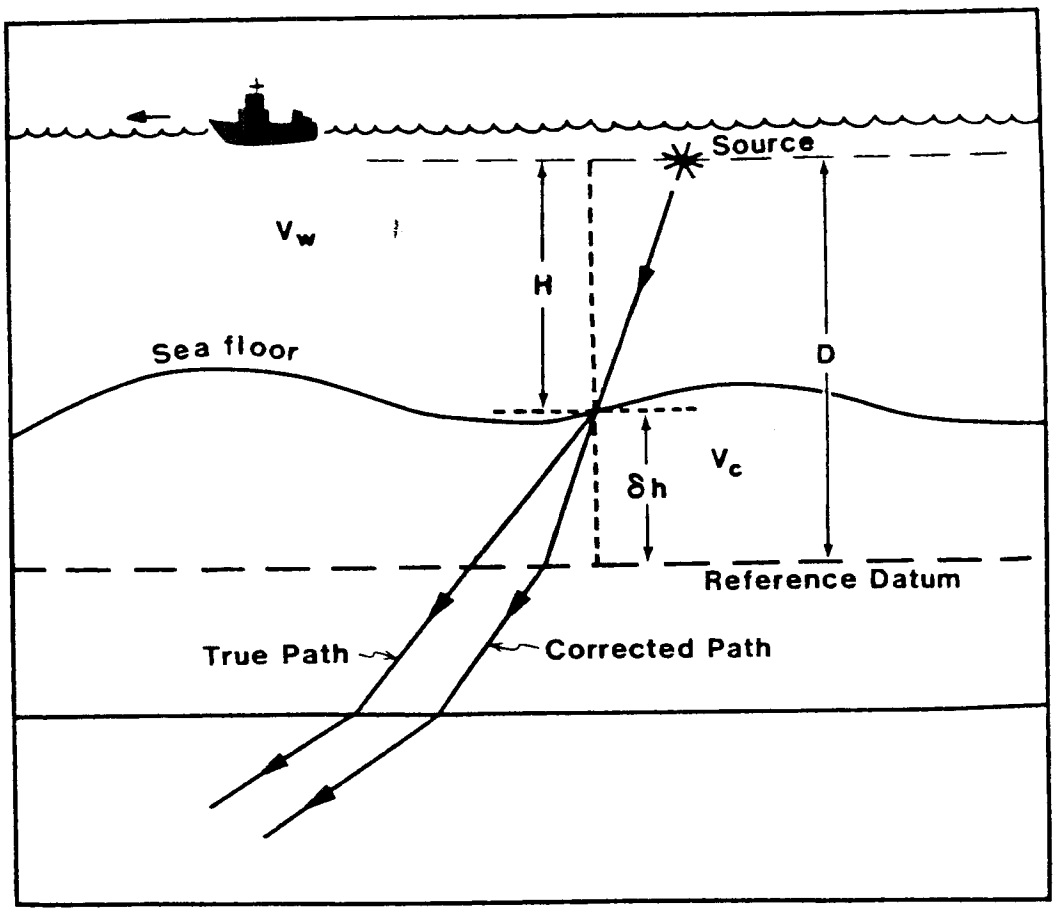

Figure 4. Schematic representation of true and corrected ray path using the datum correction method discussed by Purdy, 1982.

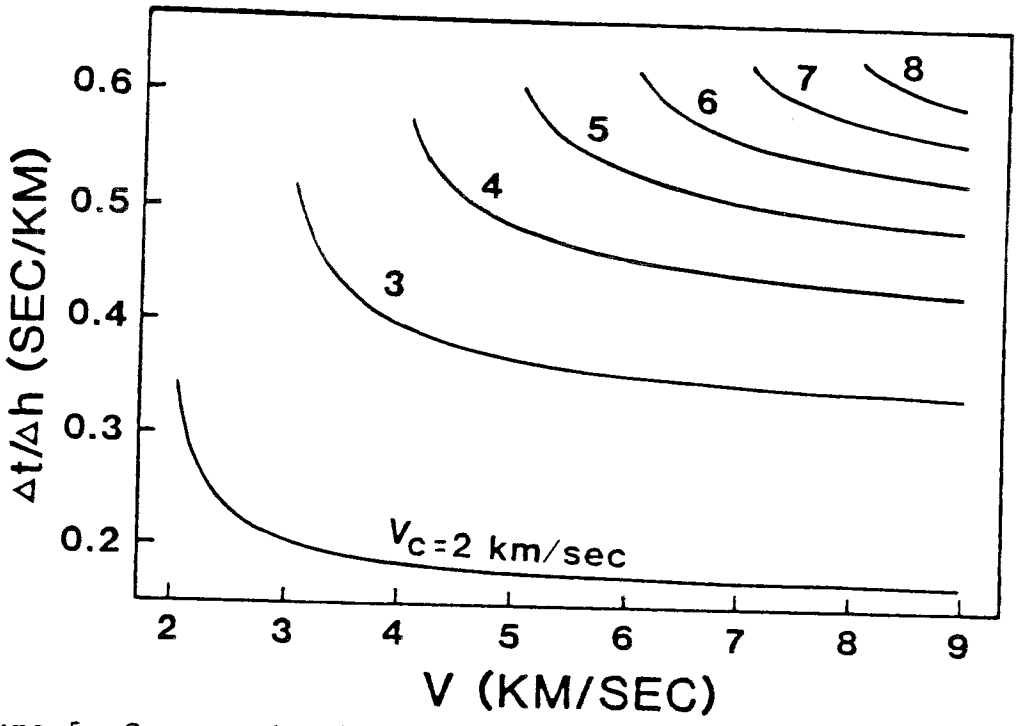

Figure 5. Curves showing the relationship between the correction coefficient and the refracting layer phase velocity for seven values of the shallowest crustal velocity V_C (2 to 8 km/sec in 1 km/sec increments).

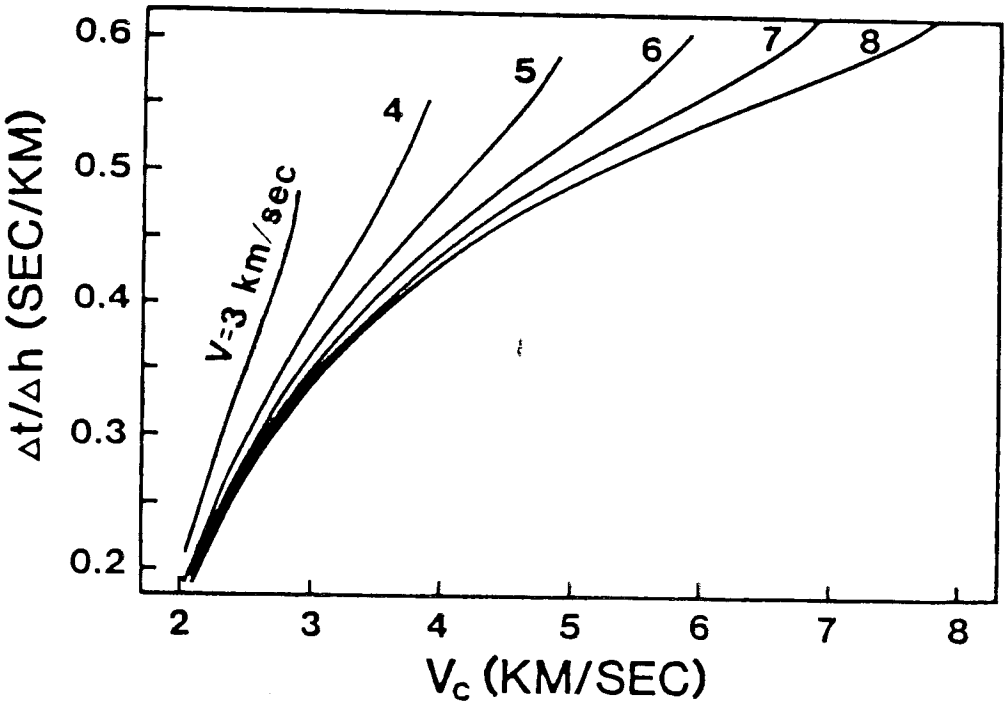

Figure 6. Curves showing the relationship between the correction coefficient and the values of the shallowest crustal velocity V_C for six values of the refracting layer phase velocity (3 to 8 km/sec in 1 km/sec increments).

observed layer. Thus in calculating our time corrections, we assumed top-layer crustal velocities that were at least 1 km/sec less than the velocity of the shallowest observed layer. This assumption made the value of the correction coefficient vary only slightly for all the observed layers, which implied that the magnitude of the computed time correction depended primarily on the amount of the topographic change δh along the profile.

We applied this method to all the records of the six lines. The time corrections obtained for Lines 1-4 were very small and produced reductions in travel times of less than $\pm$8 ms; these corrections were small because of the flatness of the seafloor. The time correction calculated for Line 5 was substantial with values ranging between 0 and $\pm$116 ms; these large time corrections were expected for this line considering the large bathymetric change across the shelf break. The time corrections computed for Line 6 contribute a maximum of about $\pm$32 ms change in the measured travel times.

The record sections shown in Appendix B are the sets of vertical-component OBS data that were recorded by the instruments. To obtain the true velocities and layer thicknesses, the profile has to be reversed. Reversibility of these profiles depends on several conditions being satisfied (Ewing et al., 1937); these conditions include 1) the total reciprocal times must be equal at the end receivers for the profiles, and 2) the intercept times for a single continuous layer measured at the middle OBS must be equal for the two arms of the section. These two conditions were met to within experimental error for most of the deep layers, but in no case were these conditions met for the shallow layers. Reversing only the deep layers gave erroneous results because of the process of computation of true velocities. We tried to force the total reciprocal times to coincide for reverse coverages using least squares, but the calculation resulted in errors which were much larger than the experimental errors.

The unreversibility of this data is probably due to lateral inhomogeneities such as pinchouts and/or intrusions along each line. Furthermore, velocity anomalies at either the shot or the OBS locations or both could have given rise to the incompatible travel times (Warren et al., 1966). Since reversal of the profiles was impossible, we assumed a model of flat homogeneous horizontal layers in order to compute the layer thicknesses. Although the velocity and depth values thus obtained were all apparent, we believe that the true values and the apparent values differ by only very small amounts since the geological setting presents very small dips in most areas of the carbonate platform. One exception is Line 5 where a large change from the apparent values would be realized across the shelf/slope break.

The approach we used with this data set was to plot the unreversed velocity-depth data for each line as shown in Figures 7-12. Each straight line segment denotes the refracting horizon computed for a given apparent velocity, and the large dot associated with each line segment indicates the horizontal location along the line of the point of critical reflection for that layer.

DATA INTERPRETATION

In general, most of the shallow layers were not observed as first arrivals because of the sparseness of the data since shot spacing averaged about 1.5 km. Thus most of the plotted low-velocity shallow layers were derived from nearby shallow reflection interval velocities and thicknesses (UTIG Southeastern Gulf of Mexico Multichannel Seismic Data). Whenever possible, the Antoine and Ewing (1963) shallow refraction results were used as the appropriate shallow layer parameters; their shot spacing averaged about 650 m. Our interpretations of the velocity-depth data (Figures 7-12) for these lines are summarized in Appendix D and discussed in details below.

Line 1

This line was shot in water depths of about 0.2 km. The shallowest layers discernible as first arrivals at OBS 1 and OBS 3 had measured P-wave velocities of 3.04 $\pm$ 0.06 and 2.74 $\pm$ 0.06 km/sec respectively (Figures 7 and D1). The confidence limits shown for the velocities were calculated using 90% student-t statistical analysis. The top 1.65 km/sec layer was measured from the western end of the reflection profile (FLA-1)*. The sedimentary column with velocity 1.6-5.5 km/sec thickens towards the north. The absence of the 4.84 km/sec layer in OBS 3 signifies the pinching out of this layer. The depth to the top of the observed 5.58 $\pm$ 0.06 km/sec layer increases towards the north from 2.0 km at OBS 3 to 3.0 km at OBS 1. A crustal layer of velocity 6.60-6.88 $\pm$ 0.08 km/sec was observed at both OBS positions at depths of 10-11 km.

Line 2

This line was shot at water depths ranging from 55 m at OBS 3 to 144 m at OBS 1, and a shallow feature of this line is the near-bottom presence of a high-velocity layer (Figures 8 and D2). All three OBS units recorded near-offset arrivals from this shallow sediment layer whose velocity ranged from 4.62 $\pm$ 1.66 km/sec at OBS 3 to 5.22 $\pm$ 0.04 km/sec at OBS 1. We assumed the existence of shallow layers with velocities of 1.8 and 2.4 km/sec at OBS 1 (Profile 4 of Antoine and Ewing, 1963). At OBS 2 and OBS 3, these assumed layers had respective velocities of 1.8 and 2.5 km/sec (Antoine and Ewing, 1963; second arrivals from profile 3). The 5.8-5.9 km/sec layer was observed on all the receivers, and the top of this layer was almost flat along the line at about 3.0-4.0 km depth below the sea surface. A crustal layer with velocity of 6.48-

---

* This code is used by UTIG for data management. Informations about all reflection sections mentioned in this report can be obtained from the Data Manager's office by quoting the codes. Phone (512)-458-6484.

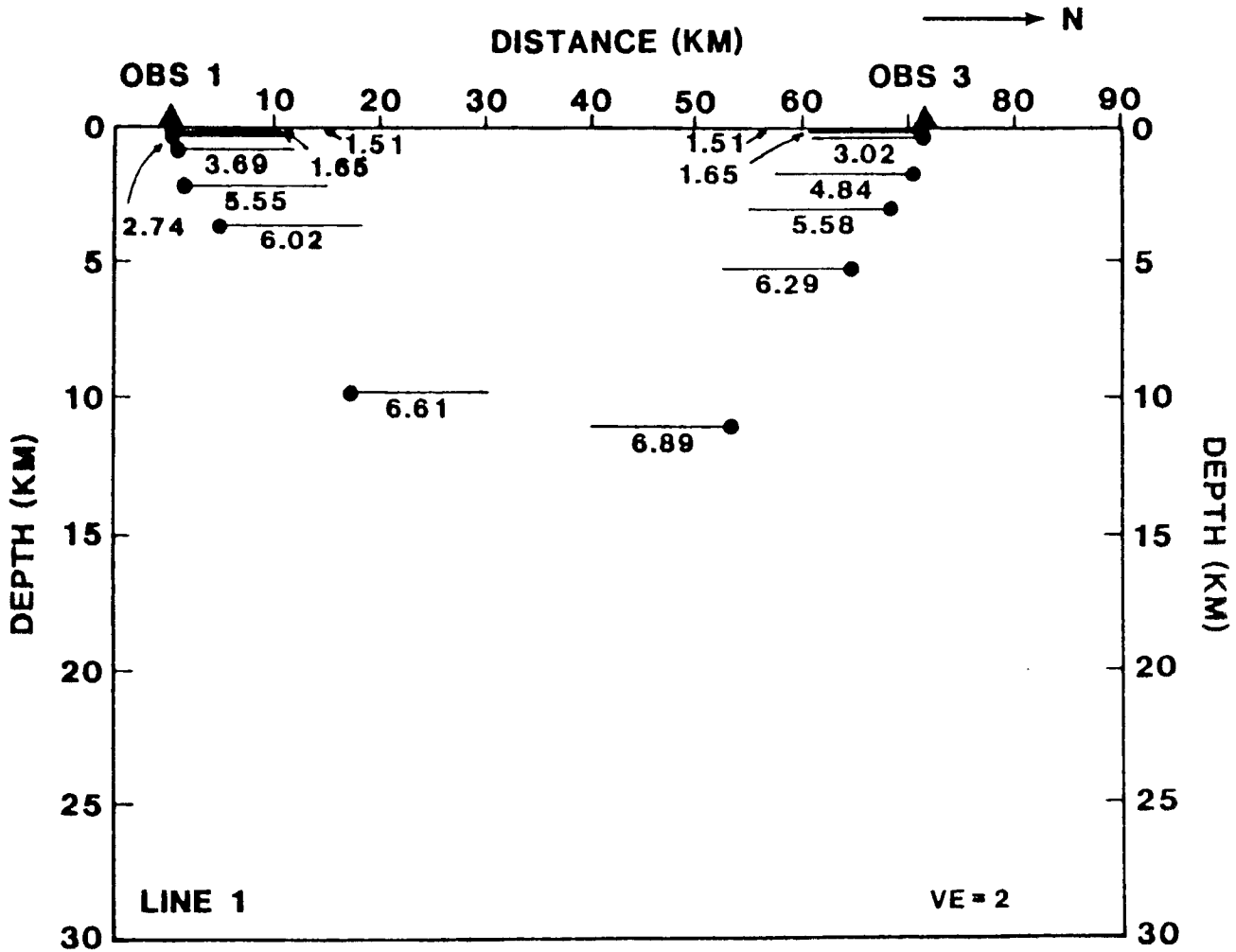

Figure 7. Velocity-depth profiles for Line 1 calculated using a model for a flat-layered homogeneous medium. Large dots show the calculated point of critical reflection, and the horizontal bars extending from the dots represent the refracting interface with the apparent velocity shown below the bar.

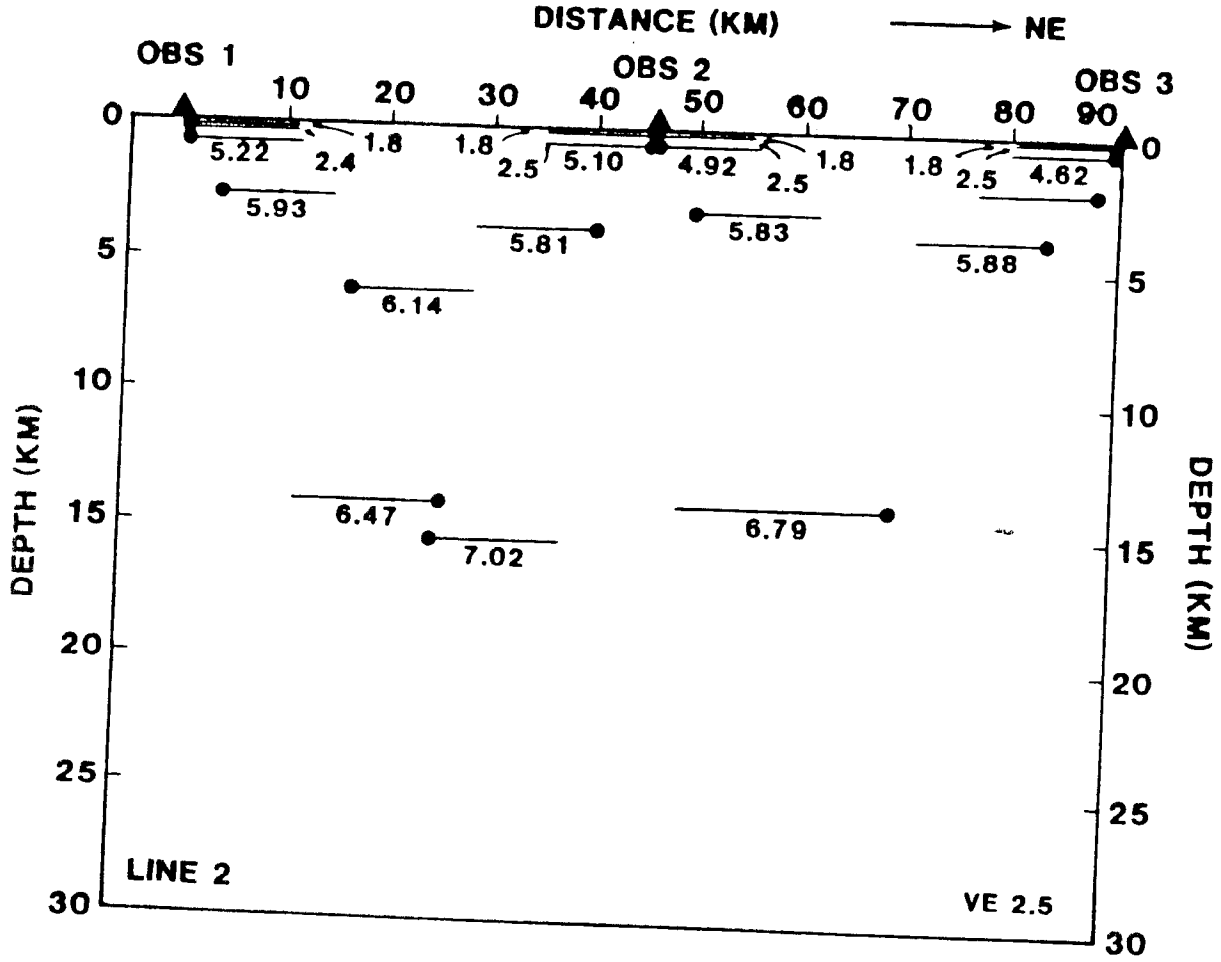

Figure 8. Velocity-depth profiles for Line 2 calculated using a model for a flat-layered homogeneous medium. Large dots and horizontal bars are as defined in the caption to Figure 7.

7.03 ± 0.02 km/sec was recorded at an apparent depth of 14-15 km by the two end OBS units.

Line 3

Line 3 was shot in water depths varying from 99 m at OBS 1 to 70 m at OBS 3 locations. Although this line was planned to be 90 km long, high seas from an unfavorable direction affected the ship speed so that the actual line length was 67 km, and the last shot was positioned 17 km SSE from OBS 1. Because of this long offset, the shallowest layer recorded as a first arrival by OBS 1 had a velocity of 5.54 ± 0.17 km/sec. However, by using the method of reduced travel-time plotting for the later arrivals, layers with velocities 2.35, 3.45 and 4.90 km/sec were found above the 5.54 km/sec layer at the OBS 1 location. Beneath OBS 3, the shallowest layer observable from first arrivals had a velocity of 4.36 ± 0.10 km/sec, and reduced travel-time plots revealed 2.35 and 4.90 km/sec layers. A relatively flat-topped 5.8-5.9 km/sec layer at a depth of about 4.0-4.5 km was observed on both OBS records. Both receivers detected a crustal layer with velocity of 6.33 ± 0.01 km/sec (OBS 1) and 6.79 ± 0.05 km/sec whose apparent depth increased towards the NNW from 9.0 km (OBS 3) to about 13.0 km (OBS 1). The apparent velocity-depth profile is shown in Figures 9 and D3.

Line 4

Line 4 (Figures 10 and D4) was an approximate east-west profile with water depth changing from 44 m at the east end to 68 m at the west. This line lies south and almost parallel to profiles 1-4 of Antoine and Ewing (1963). The shallowest layer recorded in this line had apparent velocities varying from 3.85 ± 0.11 km/sec at OBS 1 to 4.83 ± 0.07 km/sec at OBS 3. The low-velocity layers (2.14, 2.05, 2.18 km/sec) shown in Figure 10 are interval velocities computed from appropriately located reflection stacking velocities from FLA-7. Arrivals from the 5.66-5.95 km/sec layer were recorded by all the receivers. The depth to the top of this layer changed from 1.6 km at the western end of the line (OBS 3) to a maximum of 4 km near the center of the line (OBS 2) and became shallow again at the nearshore end (OBS 1) with a depth of 2.3 km. Beneath this layer, at a depth of about 8.0-9.0 km in the east and 14.0 km in the west, was the 6.38-6.51 ± 0.13 km/sec layer. The top of a deep crustal layer with a velocity of 7.47 ± 0.06 km/sec was recorded only by OBS 3 at a depth of 24.5 km.

Line 5

Line 5 was shot across the shelf edge in water ranging in depth from 62 m (OBS 1) to 916 m (OBS 3), and the line length was about 82 km. The middle OBS was located about 15 km south of the shelf break at a depth of 558 m. The data for this line are summarized in Figures 11 and D5. The shallowest layer velocities were derived from the nearby reflection profiles GT3-69 and FLA-9. The character of the OBS 3 record (figure B13) shows that the 6.67 ± 0.02 km/sec

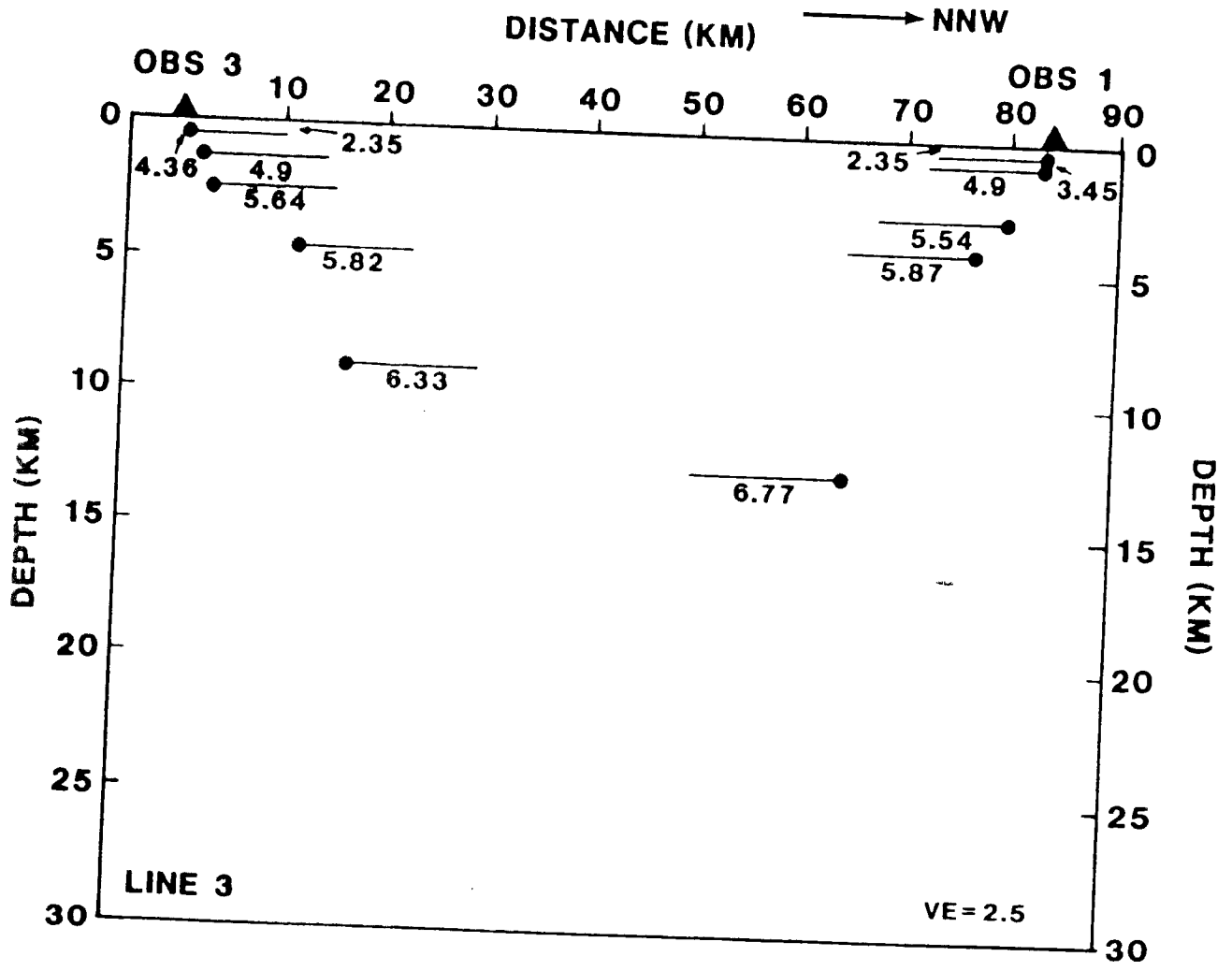

Figure 9. Velocity-depth profiles for Line 3 calculated using a model for a flat-layered homogeneous medium. Large dots and horizontal bars are as defined in the caption for Figure 7.

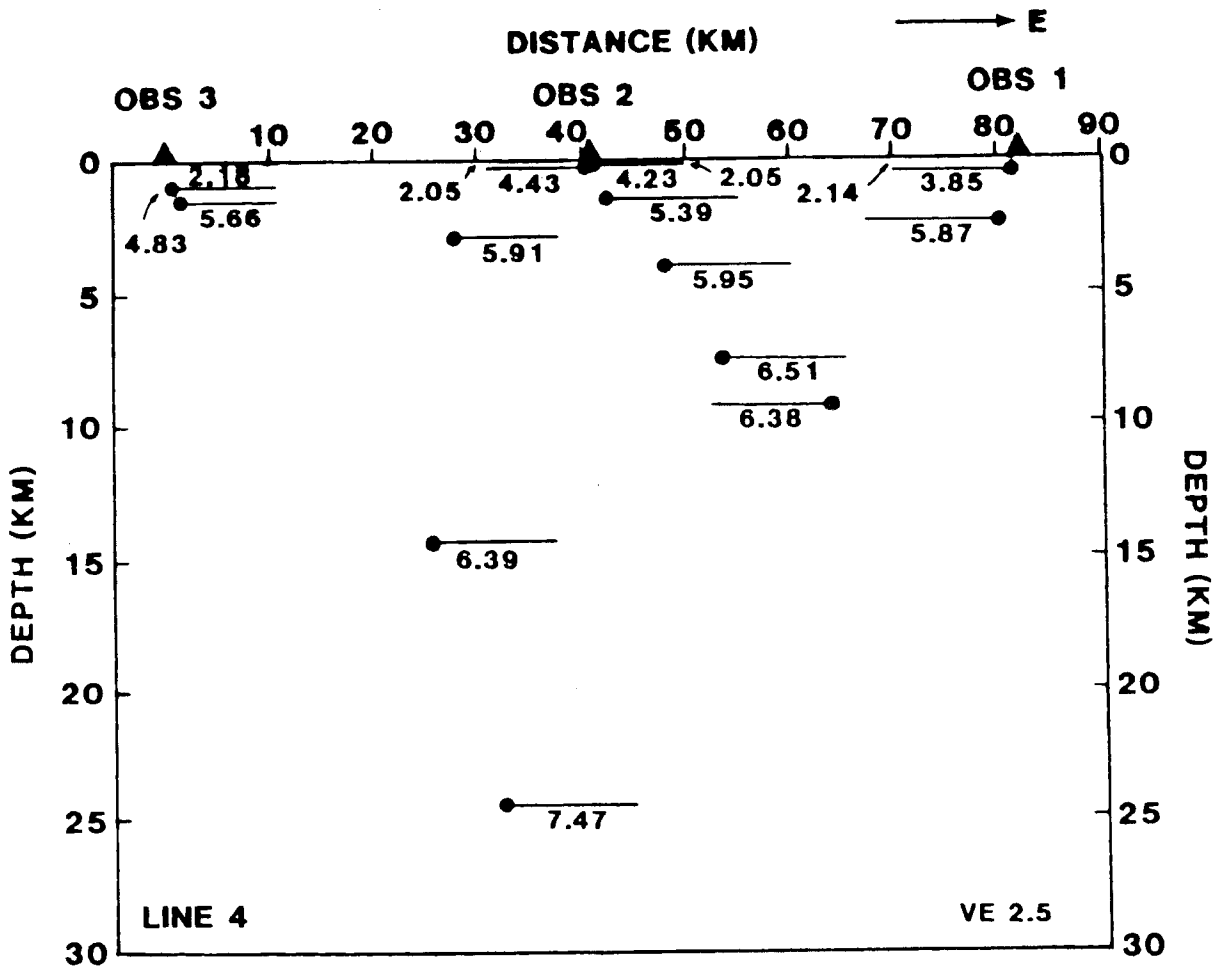

Figure 10. Velocity-depth profiles for Line 4 calculated using a model for a flat-layered homogeneous medium. Large dots and horizontal bars are as defined in the caption for Figure 7.

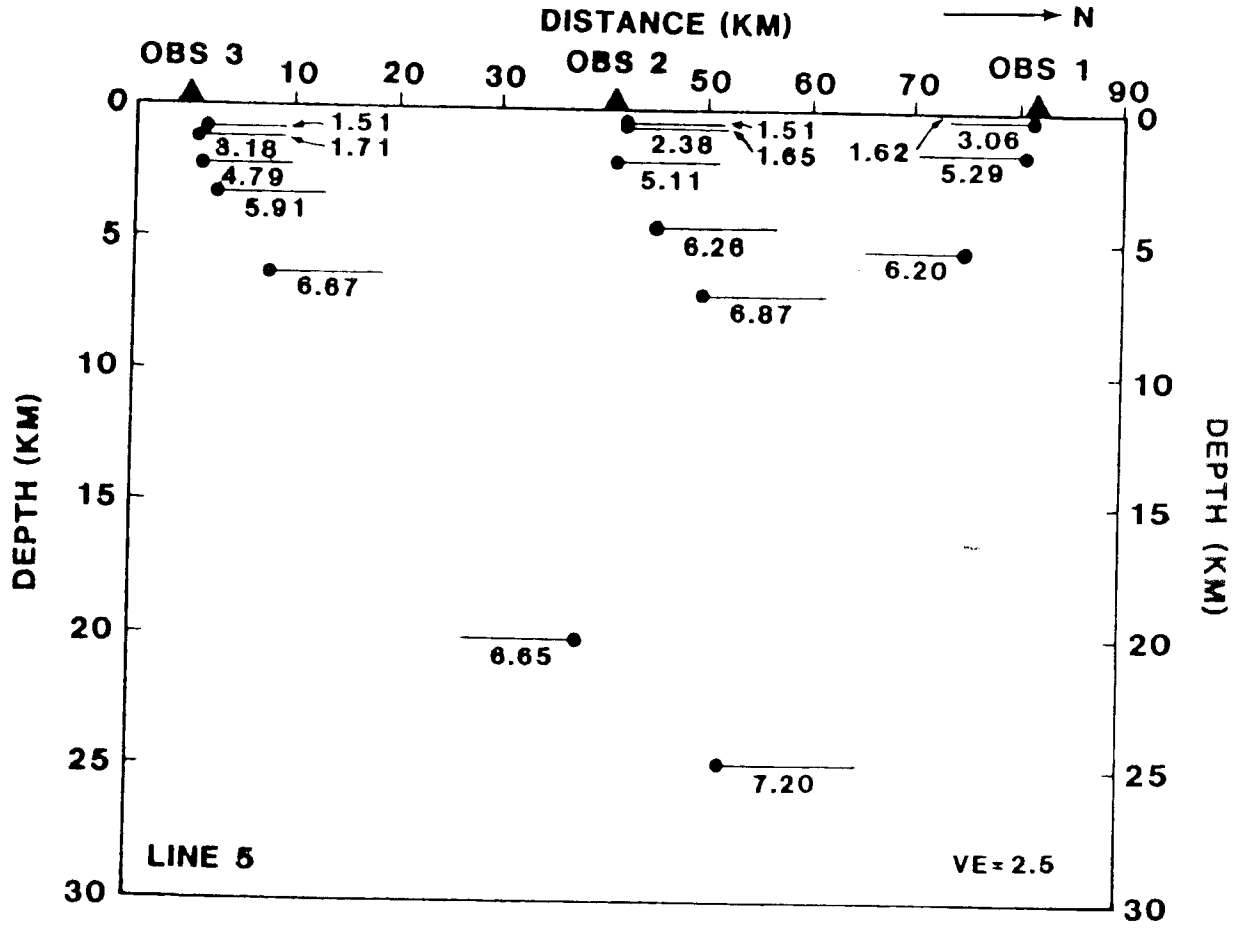

Figure 11. Velocity-depth profiles for Line 5 calculated using a model for a flat-layered homogeneous medium. Large dots and horizontal bars are as defined in the caption for Figure 7.

layer arrivals decreased suddenly in amplitude at about 33 km from the receiver. About 1 second later in the seismogram, another strong arrival with almost the same velocity (6.85 ± 0.02 km/sec) was observed, and this arrival persisted to distances greater than 60 km from the receiver. One interpretation of this feature suggests a basement fault with a one-second throw, but this amount of throw would necessitate a fault with more than 13 km of crustal displacement which may be physically unlikely in this area. Since the records of OBS 1 and OBS 2 never showed this feature, we neglected the observation in our calculations although we mention this problem later in our recommendations. We also observed that the 4.79 ± 0.19 km/sec layer was absent under OBS 2 and OBS 1, thus implying that the layer pinches out towards the north. Arrivals from the observed 6.87 ± 0.05 km/sec layer were recorded only by OBS 2 at a shallow depth of 7 km. A deep crustal layer with velocity of 7.20 ± 0.05 km/sec was observed at a depth of 25 km only at the OBS 3 site.

Line 6

The only deep-water profile, Line 6, was shot north of the Cuban coast in water whose mean depth was 2.4 km. The records from this line are fairly consistent and better in quality than the records from the other lines. The lack of reverberations in the records from OBS 2 and OBS 3 (Figures B15 and B16) suggest that these receivers were on hard surfaces in contrast to the strong reverberations in the records of Lines 1 to 5 (Figures B1-B13) and OBS 1 of Line 6 (Figure B14) which all depict sediment pond locations. Furthermore, the presence of strong water bottom multiples in the records of OBS 2 and OBS 3 supports this notion. The concentration of high-amplitude arrivals detected by OBS 1 at distance ranges of 41-59 km and 68-84 km suggests that the top boundary of the layer causing this amplitude variation is rolling in nature with consequent focusing and defocusing of acoustic energy. This feature is also present in the OBS 3 records. The apparent velocity of this layer, as shown in Figures 12 and D6, is 8.39 ± 0.02 km/sec (OBS 1) and 7.65 ± 0.01 km/sec (OBS 3), and we interpret the top boundary of this layer to be Moho. The shallowest layer recorded as a first arrival was a 2.63 ± 0.32 km/sec layer beneath OBS 3 and a 4.66 ± 0.15 km/sec layer beneath OBS 1. The 1.90 km/sec layer overlying this layer (OBS 1) was computed from the stacking velocity of reflection profile SF-5B. Beneath OBS 2, the shallowest layer recorded had a velocity of 5.03 ± 0.03 km/sec underlying the 2.03 km/sec layer deduced from the reflection profile SF-11.

REGIONAL SYNTHESIS

In order to synthesize and interpret the results of this refraction experiment involving 16 seismometers, we plotted (Figure 13) the occurrence of the various observed apparent velocities using velocity intervals of 0.5 km/sec to demonstrate the most prominent layers of the entire region; this velocity histogram summarizes the interpreted data from Lines 1-5 which were all located in the

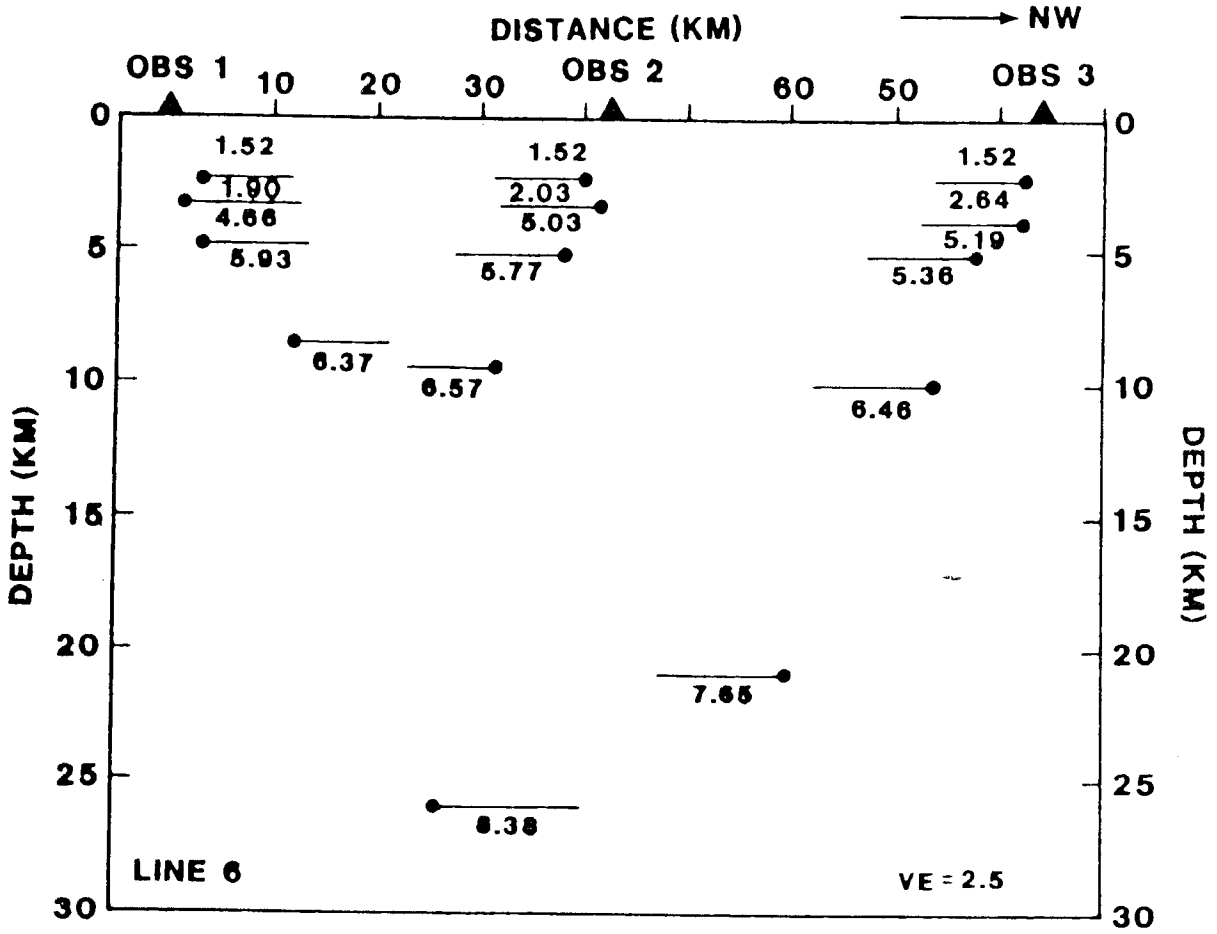

Figure 12. Velocity-depth profiles for Line 6 calculated using a model for a flat-layered homogeneous medium. Large dots and horizontal bars are as defined in the caption for Figure 7.

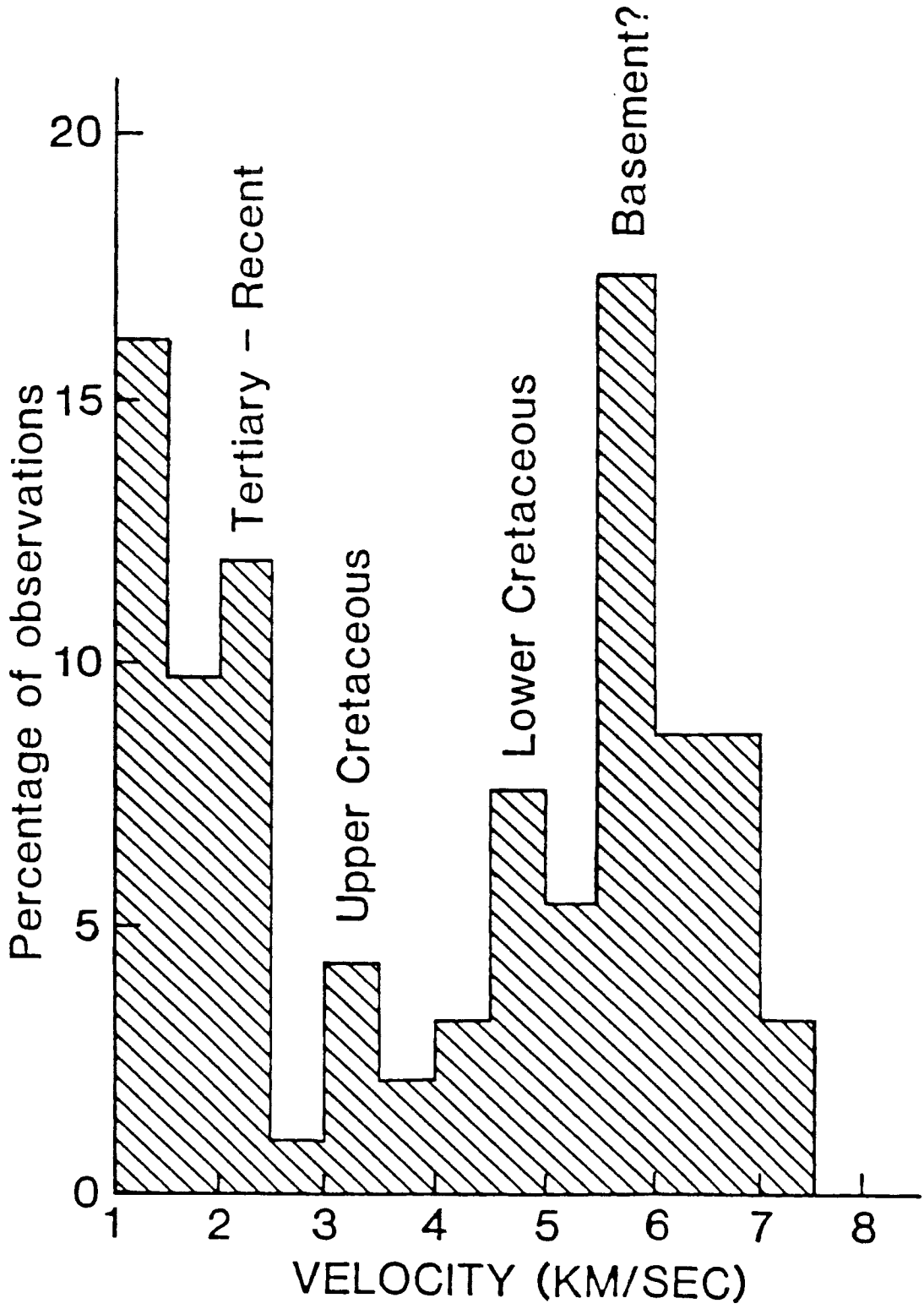

Figure 13. Histogram plot for lines located in the Florida platform (Lines 1 - 5) showing the percentage occurrence of the observed apparent velocities using an interval of 0.5 km/sec. The speculated ages of the layers are also indicated as discussed in the text.

carbonate platform. With the exception of the water column and the shallow sedimentary layers (under 3 km/sec) which were measured mainly by using reflection stacking velocities, the most prominent layers were the 5.5-6.0 km/sec layer (about 18% of the observation), the 6.0-6.5 km/sec layer (about 9% of the observation), the 6.5-7.0 km/sec layer (about 9% of the observation), and the 4.5-5.0 km/sec layer (which made up of about 8% of the observation),

Taking the geologic basement to be the layer that underlies all sedimentary strata, we consider the strongly prominent 5.5-6.0 km/sec layer to be basement for the Florida platform. This velocity range also corresponds to the most prominent refractor of Antoine and Ewing (1963), which they classified as the Precambrian basement which is also seen in several areas of the east coast. Furthermore, well data from a well site near the northeastern end of Line 2 near the Pinellas County Arch located the crystalline basement at a depth of 3.4 km (Buffler et al., 1984) which corresponds well with our depth range of 3.0-4.0 km for the 5.8-5.9 km/sec layer we observed in Line 2. Martin and Case (1975), however, classified their 5.6-6.0 km/sec layer as lower Cretaceous and older rocks overlying a 6.4 km/sec basement. The 5.5-5.7 km/sec sequence could also be interpreted as a carbonate section overlying our 5.8-6.0 km/sec basement layer.

Overlying the basement rock, we generally found a 4.5-5.0 km/sec layer. This layer is analogous to the 4.9 km/sec lower Mesozoic and Paleozoic layer of Antoine and Ewing (1963) and the 4.8-5.1 km/sec lower Cretaceous beds of Martin and Case (1975). However, the thin upper Cretaceous beds that one would expect to find with velocities in the range of 3.0-4.0 km/sec were seldom observed in this experiment; we believe this is a consequence of the large shot spacing and consequent sparseness of the data which made the first-arrival observation of these shallow layers impossible. Another possible explanation for the absence of the 3.0-4.0 km/sec arrivals may be presence of the shallow high velocity (4.5-5.0 km/sec) layer. The Tertiary-to-recent deposits with velocities ranging from 1.7 to 2.6 km/sec which are prominent in Figure 13 generally were not observed in the refraction data but were deduced from the stacking velocities of the nearby reflection profiles. Antoine and Ewing correlated these beds with stratigraphic units on the Florida peninsula using well data.

The crustal layer with a velocity of 6.6-6.8 km/sec was observed at depths ranging from 10-15 km. This layer corresponds to the 6.8 km/sec layer of Antoine and Ewing (1963) which they derived from second arrivals at a depth of 14 km. This layer was also observed at a shallower depth of about 7.0 km beneath Line 5 where we infer that it corresponds to the southernmost extension of the Sheffield arch. The arch is a basement high that may be associated with a diabasic intrusive situated several kilometers to the northwest of this line (Shaub, personal communication). It is interesting to note that in no case was the crust-mantle boundary (Moho) observed in the platform for this set of profiles which suggests that the mantle is at a depth of at least 30 km under the Florida platform. This is consistent with the notion that thick continental crust underlies the Florida platform.

The deep-water line (Line 6) can be considered as a southeastward continuation of OBS refraction Line 12 of Ibrahim et al. (1981). In general, the same sequence of layers was observed in both experiments. Results from both experiments show that the sedimentary column is virtually flat with velocities ranging from 1.9 km/sec at the water bottom to 5.4 km/sec at a depth of about 7.0 km. We found the underlying acoustic basement (velocity of 5.4-6.0 km/sec) to be approximately flat just as it was in their experiment. Beneath the basement we observed a crustal layer, 6-15 km thick (thickening towards the south), with a velocity ranging from 6.4-6.6 km/sec. We observed a well-defined Moho at both ends of Line 6 with apparent mantle velocities of 7.7 km/sec (OBS 3 - north) and 8.4 km/sec (OBS 1 - south). The corresponding true velocity for the mantle may range from 7.9 to 8.1 km/sec and indicates a Moho dipping towards Cuba. The depth of our observed Moho ranged from 21 km at the north end (OBS 3) to 26 km at the south end (OBS 1) about 20 km north of the Cuban coast. This compares well with the observations of Ibrahim et al. (1981) where they observed a mantle at a depth of 18 km with a velocity of 8.1 km/sec and strongly dipping towards the south.

DISCUSSION

The refraction results obtained from the five lines on the carbonate platform were combined to produce the generalized north-south cross-section shown in Figure 14.

The shallow sedimentary layers have velocities between 1.7 and 3.2 km/sec with an average thickness of about 1.4 km, and they thicken only slightly towards both the north and the south. Underlying the top sedimentary layer in the middle of the section is a lens of sediment with a velocity range of 4.4-4.9 km/sec whose thickness varies from about 0.5 km at both ends of the lens to about 2.0 km at the center of Florida basin; we consider this lens to be lower Cretaceous in age. The 4.8 km/sec layer observed north of the Pinellas County arch is probably made of late Jurassic-Cenozoic carbonate and evaporite deposits which have a uniform thickness towards the north and grade to the NNW into terrigenous deposits (Uchupi, 1975). Underlying this unit is the 5.3-5.7 km/sec layer which has a maximum thickness of about 2.0 km just south of the Pinellas arch. This layer we interpret to be a late Jurassic sequence.

We interpret the 5.6 km/sec layer found north of the Pinellas County arch, as basement, but in most cases we took the basement to be the 5.8-5.9 km/sec layer. Thus, we take the 5.6-6.0 km/sec layer that underlies the whole sedimentary sequence and whose thickness varies from 2.5 km at the Sheffield arch to a maximum of almost 10.0 km immediately north of this arch to be the basement layer for the region. Figure 15 shows a depth contour map for the top of this layer. The 5.5-5.7 km/sec layer may alternatively be interpreted to constitute a carbonate section in the basin whose velocities remain indistinguishable from those of the crust.

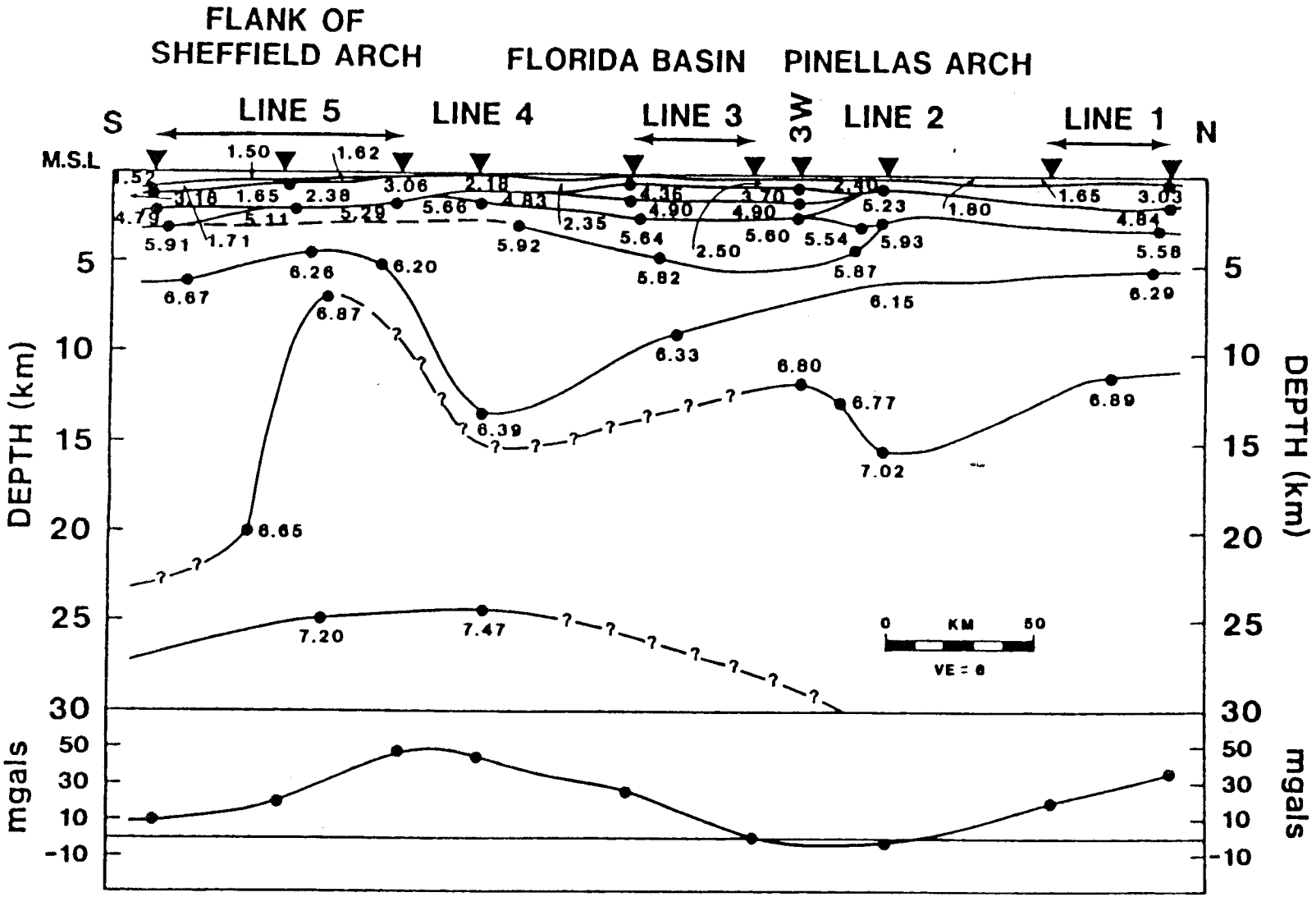

Figure 14. Composite north-south geologic cross-section of the carbonate platform deduced using Lines 1-5. The positions of the prominent geologic features are indicated in the section.

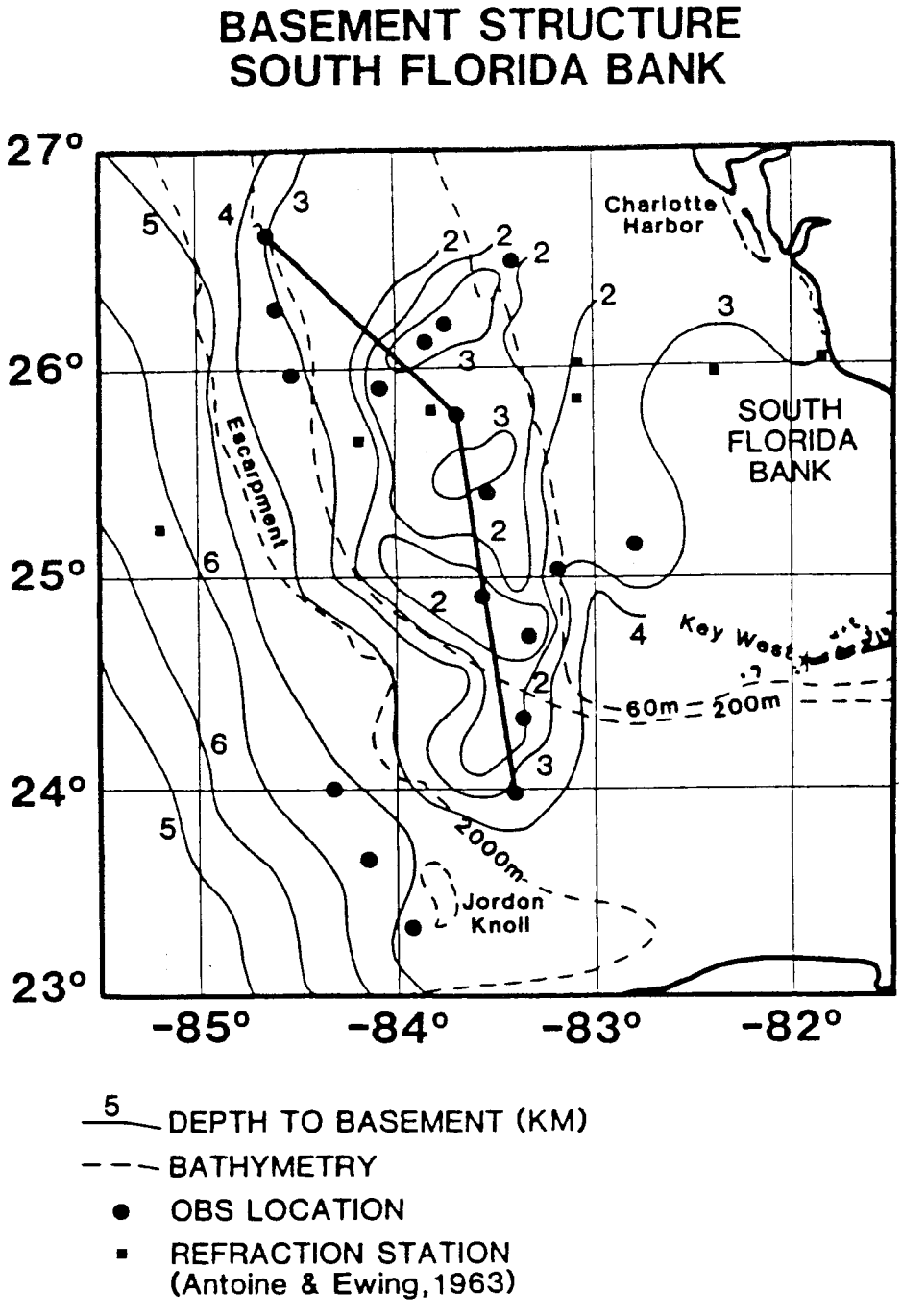

ure 15. Depth contour map of the interpreted basement for the Florida carbonate platform.

Underlying the basement layer is the upper crustal layer with velocities of 6.2-6.6 km/sec. This layer is strongly deformed by a suggested diabasic intrusive in the south. The free-air gravitational signature (Figure 16) of this intrusive is displaced to the NW. South of this intrusive, this crustal layer has a thickness in excess of 20 km. To the north of the intrusive, the crustal thickness varies from 2.0-9.0 km reaching a maximum just north of the Pinellas County arch. A lower crustal layer with velocities ranging from 6.8 to 7.0 km/sec underlies the upper crust in some areas. We speculate that most of the major tectonic events originated within the crustal layer.

In general, three major structures are reflected in this generalized cross-section:

1) the Pinellas County arch to the north where the basement depth is between 3.0 and 4.0 km;

2) a thick sedimentary column with a maximum thickness of about 5 km south of the Pinellas arch; this column contains sediment lenses whose thicknesses increase from 0.5 km near the arches to 2.0 km at the center of the basin; and

3) the Sheffield arch to the south which is possibly a diabase intrusive that helps to determine the size of the carbonate platform itself.

CONCLUSION

Until now, the deep structures underneath the Florida platform have eluded the reflection seismologist. However, as the results of this experiment demonstrate, useful information about the regional crustal structure can be gathered in this difficult region using OBS refraction surveys.

We observed that the most prominent and extensive group of arrivals characterizing all data sets on the carbonate platform had apparent P-wave velocities in the 5.5-6.0 km/sec range. The apparent depth to the top of this strongly-refracting layer varied from 2 km near the Pinellas County arch to 5 km in the basin, and the apparent depth to this layer at one OBS site near a well on Line 2 was in close agreement to the actual drilled depth to crystalline crust. We interpret this layer to be the top of crystalline basement, although an alternative interpretation of continuous shallow marine carbonate sequence cannot be ruled out. In no cases in the Florida Basin were we able to detect the crust-mantle boundary with the 90 km refraction lines.

In the deep-water area off northern Cuba the crust-mantle boundary was detected at both ends of Line 6; it dipped toward Cuba from an apparent depth of 21 km at the north end of the line to 26 km at the south end of the line.

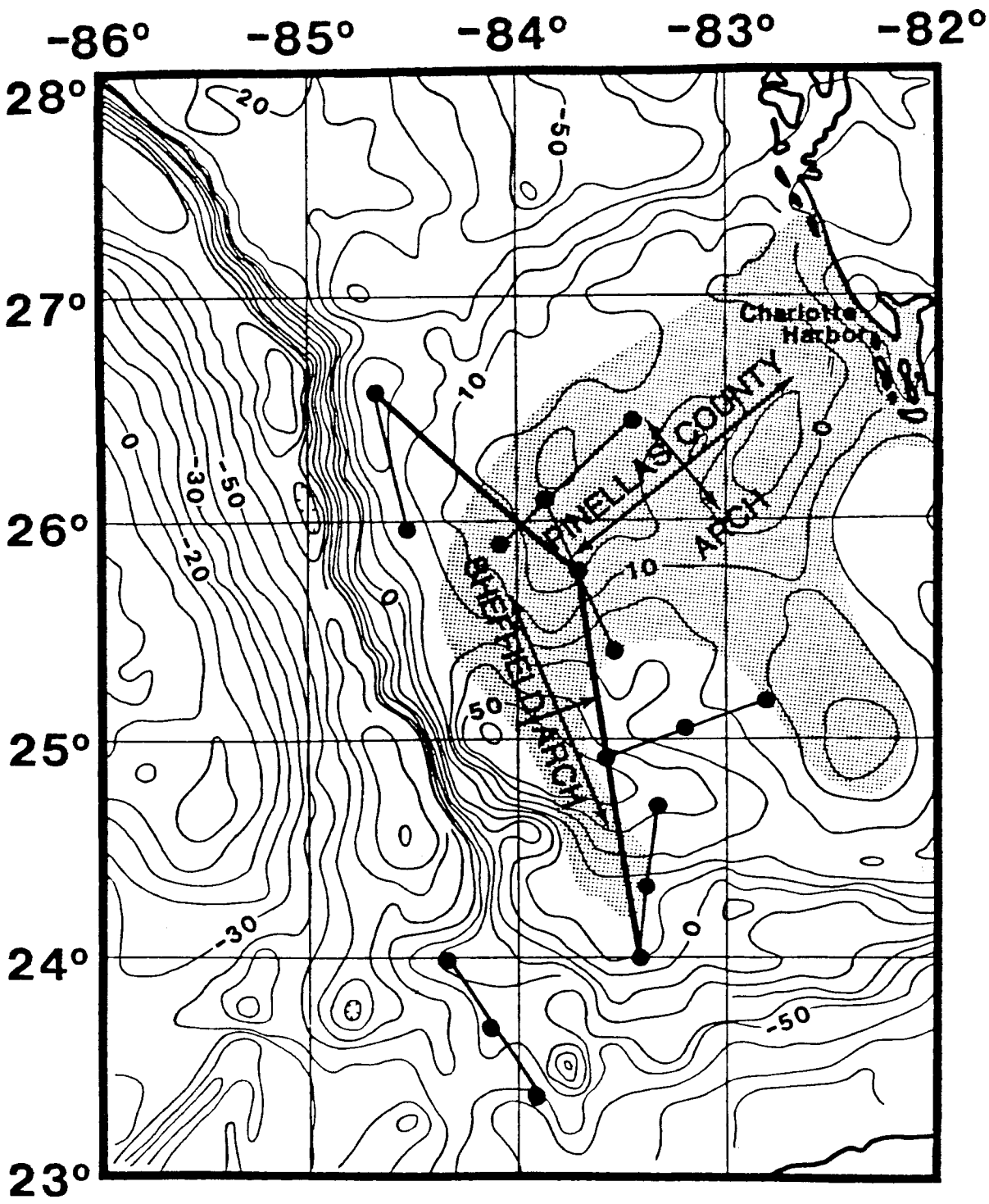

ure 16. Free-air gravity anomaly map for the Southeastern Gulf of Mexico modified from Klitgord and Popenoe (in press) showing the positions of the Pinellas County and the Sheffield arches. The location of the six refraction lines and the N-S cross-section have also been indicated.

Besides the P-waves used in this study to determine the geological structure, other types of waves were recorded by the OBS which could be used for exploration purposes. For instance, our preliminary studies have shown that the loose sediment layer in this area provided an efficient waveguide that trapped much of the low-frequency energy from our shots that we needed for deep penetration.

RECOMMENDATIONS

This experiment was successful in defining the top of the basement, thereby demonstrating the advantage of the refraction method to the reflection method for this area. However, several problems remain that could be addressed by more detailed studies. 1) The survey lines were too far apart and in no case did we have any two lines crossing each other to aid in the determination of the 3-dimensional extent of the mapped structures. 2) The survey lines were not long enough to permit the determination of the base of the crust, thus making it difficult to define the nature of the crust in the region. 3) The shots were so sparsely spaced that the shallow crustal structure could not be mapped. 4) The natural frequency of the horizontal geophones (10 Hz) was too high for the signals of interest (2-8 Hz), and the use of sets of geophones with unequal frequencies made it difficult to study particle motion. 5) We could not carry out meaningful amplitude studies on the existing data because of variations in the source signals from the fused shots of various weights.

Recent developments in UTIG OBS seismometry have made it feasible to address the above questions. We would like to conduct further refraction studies in the South Florida Bank region and would make the following recommendations for planning such an experiment.

1) The lines should be chosen to form a tighter overlapping grid with tie points, and survey lines to be shot near the shelf break should be configured as strike lines rather than dip lines.

2) Each line should be longer than 90 km and large explosive shots should be detonated near each end, in order to determine the depth to Moho.

3) The bulk of shooting on each line should be done with large high-capacity airguns with a shot spacing of 70-100 m in order to generate data sets whose high spatial redundancy would permit the use of advanced data processing techniques.

4) The primary OBS units to be used on the lines should contain a single-component geophone (4.5 Hz prefered). This would allow a recording capacity exceeding 1200 shots.

5) The lines should be supplemented with three-component OBS units each containing matched three orthogonal geophones. Identification of arrival phases such as shear-wave, Stoneley-wave or dispersed Rayleigh waves would then be greatly enhanced.

ACKNOWLEDGEMENTS

We would like to recognize Captain Allen Zschiesche and the crew of the R/V Ida Green for their efficient handling of all ship-related details and to give credit to Paul L. Donoho who designed these OBS units and who also ably served as Chief Scientist for this cruise. The technical success of the operation is due in large part to the efforts of Paul McPherson. Subir Chatterjee provided assistance during processing of the data and valuable geological perspectives during the interpretation of the results. This refraction study is part of a program for studying the South Florida Bank region under the direction of Jeanne Shaub. We wish to acknowledge the helpful suggestions of Yosio Nakamura concerning the processing and interpretation of the data, and to thank him for his careful reading of this manuscript. Finally, we thank the following organizations for their continued support of this program: Chevron Oil Field Research Company, Cities Service, Elf Aquitaine Oil and Gas, EXXON Production Research Company, Gulf Oil Company, Pennzoil Exploration and Production Company, Phillips Petroleum Company, Shell Oil Company, and Union Oil Company.

REFERENCES

Antoine, J. and J. Ewing,1963, Seismic Refraction Measurements on the Margins of the Gulf of Mexico: J. Geophys. Res. 68, pp. 1975-1996.

Barry, K.M., D. A. Cavers and C. W. Kneale,1980, Recommended Standards for Digital Tape Formats, in Digital Tape Standards: Society of Exploration Geophysicists, Tulsa, pp. 22-30.

Buffler, Richard T., Stanley D. Locker, Clint D. Cagle, William B. Sawyer, John C. Crowe and Ronald L. Phair (in press), Gulf of Mexico, Ocean Margin Drilling Program Regional Atlas Series, Atlas 6: Marine Science International, Woods Hole, Mass.

Ewing, Maurice, George P. Woollard and A. C. Vine,1939, Geophysical Investigations in the Emerged and Submerged Atlantic Coastal Plain, Part III: Barnegat Bay, New Jersey Section, Bull. Geol. Soc. Amer. 50, pp. 257-296.

Ibrahim, A. K., J. Carye, G. Latham and R. T. Buffler,1981, Crustal Structure in Gulf of Mexico from OBS Refraction and Multi-channel Reflection Data: Am. Assoc. Pet. Geol. Bull. 65, pp. 1207-1229.

Klitgord, K. D., and P. Popenoe, (in press), Florida: A Jurassic Transform Plate Boundary: Jour. Geophys. Research.

Kramer, F. S., R. A. Peterson and W. C. Walker,1968, Seismic Energy Sources Handbook: Bendix-United Geophysical Corp.

Latham, G., P. Donoho, K. Griffiths, A. Roberts and A. K. Ibrahim,1978, The Texas Ocean-Bottom Seismograph: Proc. Offshore Technology Conf., OTC#3233, pp. 1467-1476.

Martin, R.B., and J.E.Case, 1975, Geophysical Studies in the Gulf of Mexico: The ocean Basins and Margins, Vol. 3, A.E.M. Nairn and F.G. Stehli, eds., Plenum Publishing Corporation, New York, pp. 65-105.

McFarlan, E. Jr., (in preparation), Lower Cretaceous Geology, Gulf of Mexico Basin, in Decade of North Americal Geology Synthesis Volume, J. A. Salvador and R. T. Buffler, eds.; G. S. A., Boulder,Colorado.

Nakamura, Yosio, 1983, Development of an Advanced Ocean-Bottom Sensor System: Technical Report, Office of Naval Research Contract No. N00014-77-C-0606, Institute for Geophysics, Austin.

Orcutt, J. A., L. N. B. Kennett and L. M. Dorman, 1976, Structure of the East Pacific Rise from an Ocean Bottom Seismometer Survey: Geophys. J. R. astr. Soc. 45, pp. 305-320.

Purdy, G.M., 1982, The Correction for Travel Time Effects of Seafloor Topography in the Interpretation of Marine Seismic Data: Jour. Geophys. Res. Vol. 87, No. B10, pp. 8389-8396.

Steinmetz, R. L., P. L. Donoho, J. D. Murff and G. V. Latham, 1979, Coupling of a Strong Motion Ocean Bottom Seismometer: Proc. Offshore Technology Conf., OTC 3615, pp. 2235-2249.

Sutton, G. H., F. K. Duennebier, B. Iwatake, 1981, Coupling of Ocean Bottom Seismometers to Soft Bottoms: Marine Geophys. Res., 5, pp. 35-51.

Uchupi, E., 1975, Physiography of the Gulf of Mexico and Caribbean Sea: The Ocean Basins and Margins, Vol. 3, A.E.M.Nairn and F.G. Stehli, eds., Plenum Publishing Corporation, New York, pp. 1-64.

Warren, D. H., J. H. Healy and W. H. Jackson, 1966, Crustal Seismic Measurements in Southern Mississippi: J. Geophys. Res., 71, pp. 3437-3458.

Whitmarsh, R.B., 1975, Axial Intrusion Zone beneath the Median Valley of the Mid Atlantic Ridge at 37° N Detected by Explosion Seismology: Geophys. J.R. Astro. Soc., Vol. 42, pp. 189-215.

APPENDIX A

Tract and Bathymetry for each line with shot coordinates

Line 1 33

Line 2 36

Line 3 39

Line 4 42

Line 5 45

Line 6 48

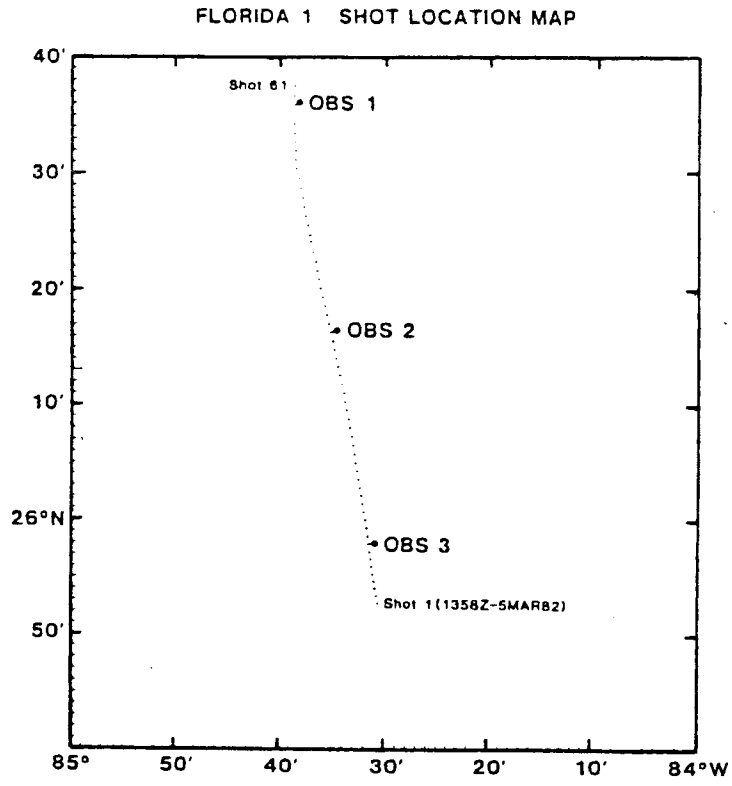

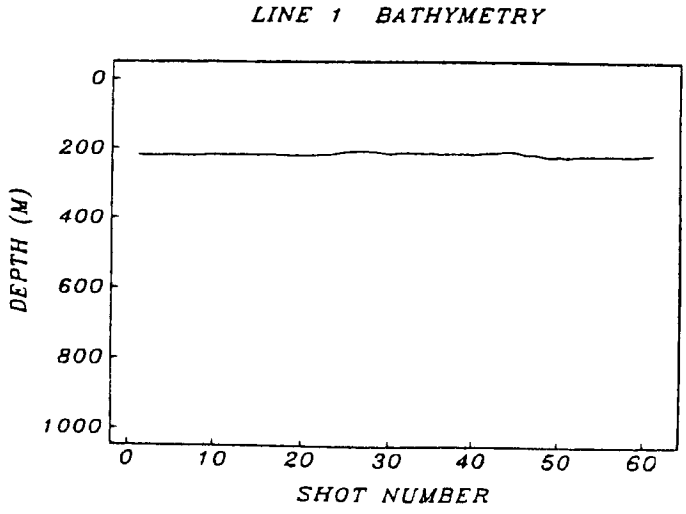

Figure A1. OBS and shot location details (top) and bathymetry (bottom) for Line 1.

TABLE A1. Line 1 shot coordinates and water depths.

SHOT	LATITUDE	LONGITUDE	WATER DEPTH(m)
1	25°52.73'	84°30.61'	218
2	25°53.39'	84°30.74'	219
3 DUD	25°54.02'	84°30.87'	219
4	25°54.63'	84°31.00'	219
5	25°55.27'	84°31.09'	218
6	25°55.93'	84°31.20'	219
7	25°56.59'	84°31.28'	219
8	25°57.24'	84°31.40'	219
9	25°57.94'	84°31.50'	218
10	25°58.60'	84°31.61'	218
11	25°59.31'	84°31.70'	216
12	26°00.01'	84°31.82'	216
13	26°00.71'	84°31.95'	218
14	26°01.40'	84°32.07'	216
15	26°02.12'	84°32.20'	218
16 DUD	26°02.80'	84°32.32'	218
17	26°03.52'	84°32.45'	218
18	26°04.29'	84°32.59'	219
19	26°04.98'	84°32.73'	219
20	26°05.74'	84°32.84'	219
21	26°06.52'	84°32.99'	219
22	26°07.30'	84°33.12'	218
23	26°08.06'	84°33.27'	216
24	26°08.82'	84°33.40'	212
25	26°09.57'	84°33.60'	209
26	26°10.30'	84°33.75'	207
27	26°11.03'	84°33.88'	205
28	26°11.83'	84°34.07'	209
29	26°12.59'	84°34.27'	210
30	26°13.36'	84°34.46'	214
31	26°14.08'	84°34.61'	210
32	26°14.84'	84°34.79'	210

Line 1 shot data (cont'd)

SHOT	LATITUDE	LONGITUDE	WATER DEPTH(m)
33	26°15.58'	84°34.95'	210
34	26°16.36'	84°35.14'	212
35	26°17.08'	84°35.33'	210
36	26°17.83'	84°35.50'	214
37	26°18.61'	84°35.71'	212
38	26°19.39'	84°35.90'	212
39*	26°20.15'	84°36.08'	212
40	26°20.91'	84°36.26'	214
41	26°21.64'	84°36.40'	210
42	26°22.43'	84°36.55'	210
43	26°23.28'	84°36.76'	207
44	26°24.19'	84°36.98'	205
45	26°24.74'	84°37.09'	207
46	26°25.56'	84°37.26'	214
47	26°26.37'	84°37.48'	214
48 DUD	26°27.14'	84°37.65'	219
49	26°27.91'	84°37.80'	223
50	26°28.74'	84°37.99'	219
51	26°29.54'	84°38.15'	223
52	26°30.42'	84°38.45'	219
53*	26°31.18'	84°38.47'	219
54*	26°31.95'	84°38.50'	219
55	26°32.70'	84°38.54'	219
56	26°33.44'	84°38.61'	219
57	26°34.24'	84°38.61'	219
58	26°35.01'	84°38.62'	219
59	26°35.84'	84°38.61'	219
60	26°36.65'	84°38.63'	216
61	26°37.45'	84°38.60'	214

*Best estimate fix -- determined after the experiment by interpolation of available Loran-C and satellite data.

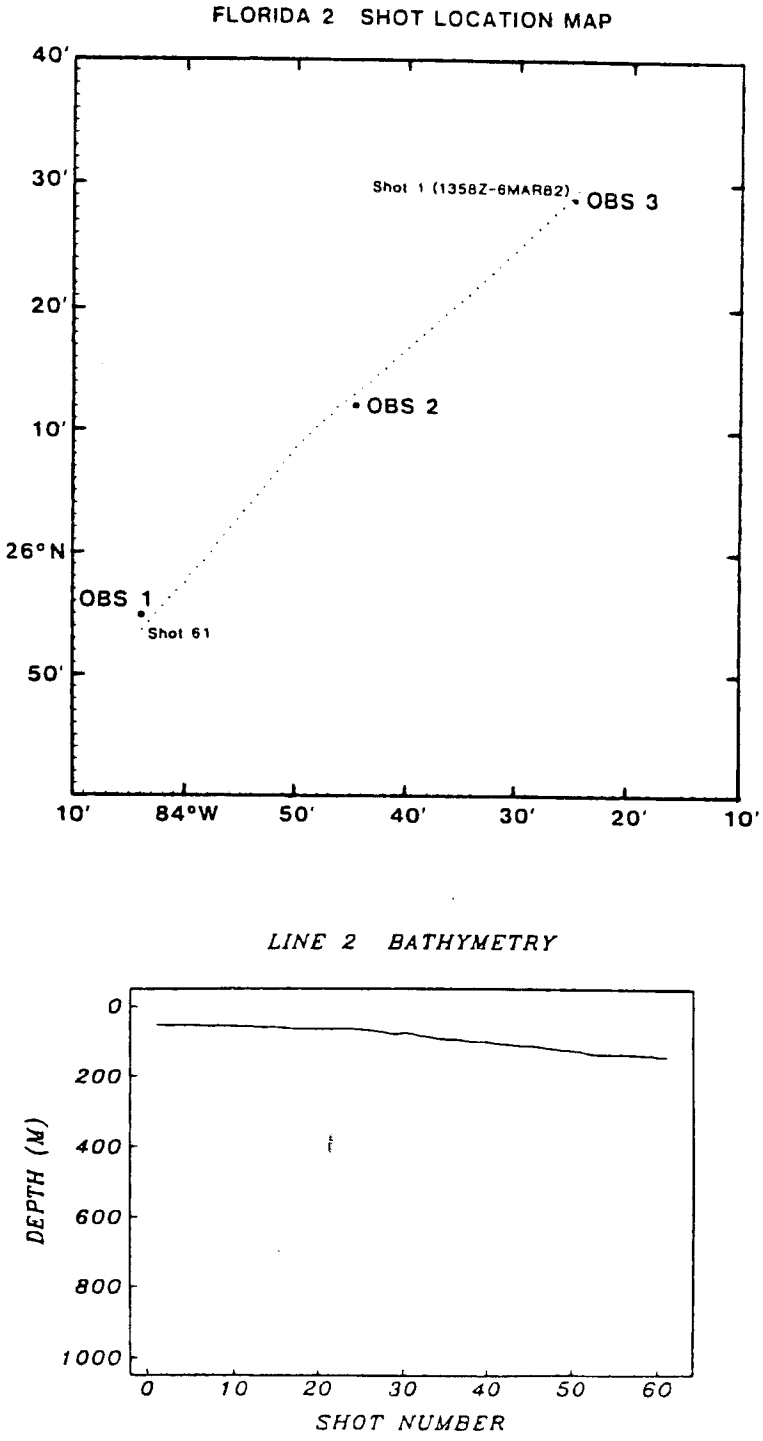

Figure A2. OBS and shot location details (top) and bathymetry (bottom) for Line 2.

TABLE A2. Line 2 shot coordinates and water depths.

SHOT	LATITUDE	LONGITUDE	WATER DEPTH(m)
1*	26°29.53'	83°24.45'	53
2 DUD	26°28.91'	83°25.16'	53
3	26°28.26'	83°25.86'	53
4	26°27.74'	83°26.56'	53
5	26°27.11'	83°27.24'	53
6	26°26.53'	83°27.93'	55
7	26°25.90'	83°28.66'	55
8	26°25.31'	83°29.39'	55
9	26°24.68'	83°30.05'	55
10	26°24.09'	83°30.79'	57
11*	26°23.50'	83°31.47'	57
12	26°22.92'	83°32.16'	57
13	26°22.35'	83°32.91'	59
14	26°21.79'	83°33.60'	60
15	26°21.18'	83°34.27'	60
16	26°20.67'	83°34.99'	62
17	26°20.14'	83°35.71'	64
18	26°19.59'	83°36.44'	64
19	26°19.04'	83°37.12'	64
20	26°18.47'	83°37.78'	64
21	26°17.96'	83°38.46'	64
22	26°17.40'	83°39.16'	64
23	26°16.91'	83°39.82'	64
24	26°16.33'	83°40.52'	64
25	26°15.79'	83°41.20'	66
26	26°15.19'	83°41.86'	68
27	26°14.66'	83°42.59'	70
28	26°14.07'	83°43.23'	75
29	26°13.55'	83°43.99'	79
30	26°13.00'	83°44.71'	75
31*	26°12.50'	83°45.45'	77
32	26°11.99'	83°46.21'	84
33	26°11.35'	83°46.77'	86

Line 2 shot data (cont'd)

SHOT	LATITUDE	LONGITUDE	WATER DEPTH(m)
34	26°10.86'	83°47.50'	91
35	26°10.34'	83°48.14'	93
36	26°09.75'	83°48.73'	93
37	26°09.21'	83°49.38'	95
38	26°08.62'	83°50.01'	99
39	26°07.96'	83°50.55'	99
40	26°07.34'	83°51.15'	101
41	26°06.63'	83°51.71'	104
42	26°06.00'	83°52.30'	106
43*	26°05.33'	83°52.90'	110
44*	26°04.67'	83°53.50'	112
45*	26°04.00'	83°54.11'	112
46*	26°03.34'	83°54.73'	113
47*	26°02.67'	83°55.33'	117
48*	26°02.00'	83°55.94'	121
49 DUD*	26°01.35'	83°56.54'	123
50	26°00.70'	83°57.16'	124
51	26°00.10'	83°57.70'	128
52	25°59.32'	83°58.37'	134
53 DUD	25°58.77'	83°58.99'	135
54	25°58.15'	83°59.60'	137
55*	25°57.50'	84°00.20'	135
56*	25°56.86'	84°00.80'	137
57*	25°56.23'	84°01.43'	137
58*	25°55.59'	84°02.04'	139
59*	25°54.95'	84°02.65'	139
60*	25°54.31'	84°03.27'	143
61*	25°53.68'	84°03.88'	143

* Best estimate fix -- determined after the experiment by interpolation of available Loran-C and satellite data.

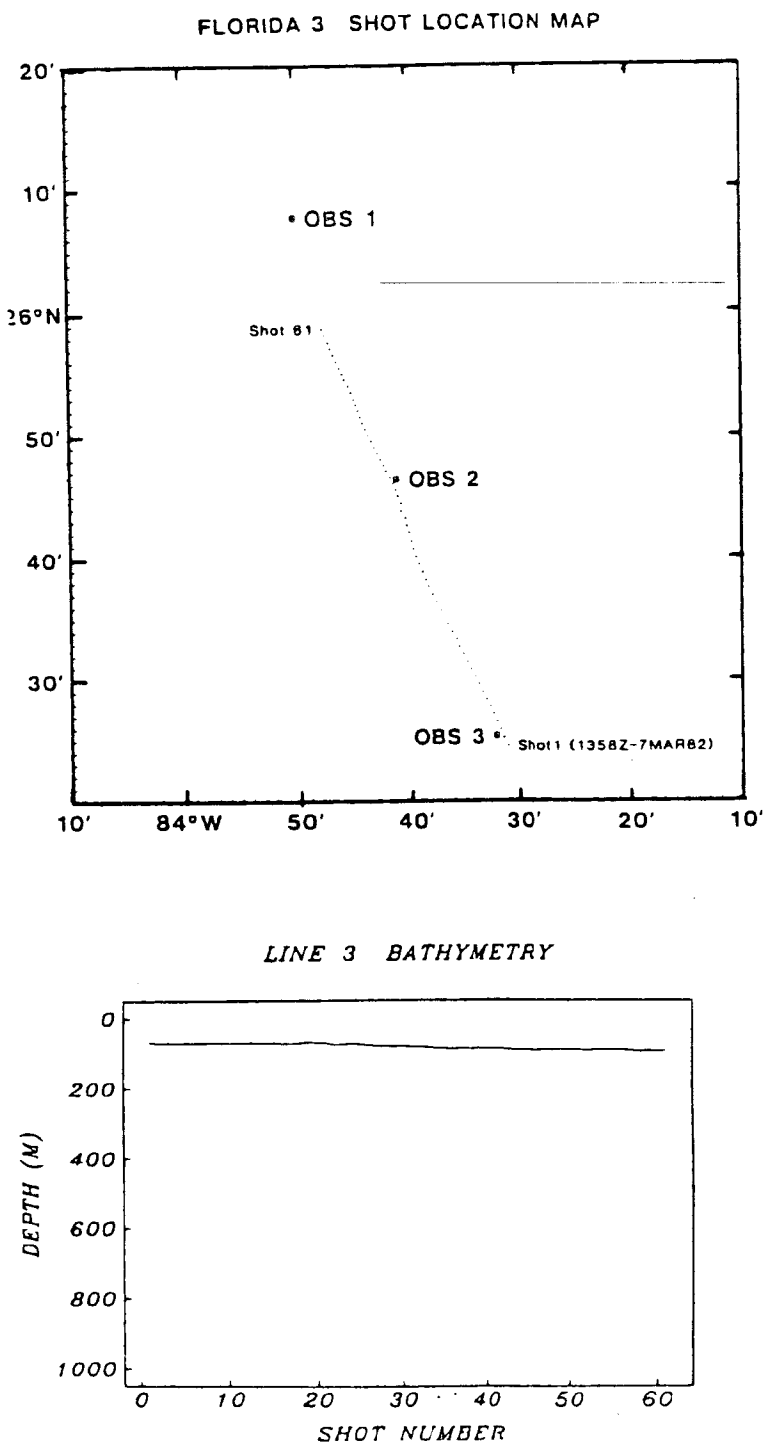

Figure A3. OBS and shot location details (top) and bathymetry (bottom) for Line 3.

TABLE A3. Line 3 shot coordinates and water depths.

SHOT	LATITUDE	LONGITUDE	WATER DEPTH(m)
1	25°24.61'	83°31.06'	68
2	25°25.29'	83°31.42'	70
3	25°25.98'	83°31.72'	70
4	25°26.60'	83°32.05'	70
5	25°27.23'	83°32.41'	70
6	25°27.84'	83°32.70'	71
7	25°28.39'	83°33.05'	71
8	25°29.00'	83°33.40'	70
9	25°29.65'	83°33.74'	71
10	25°30.25'	83°34.08'	71
11	25°30.89'	83°34.44'	71
12	25°31.49'	83°34.79'	71
13	25°32.17'	83°35.15'	71
14	25°32.79'	83°35.52'	71
15	25°33.38'	83°35.78'	70
16	25°34.01'	83°36.18'	73
17	25°34.63'	83°36.57'	73
18	25°35.23'	83°36.89'	71
19	25°35.77'	83°37.24'	68
20	25°36.43'	83°37.59'	70
21	25°37.05'	83°37.96'	71
22	25°37.68'	83°38.29'	77
23	25°38.24'	83°38.56'	75
24	25°38.89'	83°38.85'	73
25	25°39.57'	83°39.15'	75
26	25°40.14'	83°39.40'	77
27	25°40.81'	83°39.64'	79
28	25°41.40'	83°39.82'	79
29	25°42.10'	83°40.02'	79
30	25°42.68'	83°40.21'	79
31	25°43.28'	83°40.34'	82
32	25°43.84'	83°40.71'	82

Line 3 shot data (cont'd)

SHOT	LATITUDE	LONGITUDE	WATER DEPTH(m)
33	25°44.45'	83°40.72'	84
34	25°45.02'	83°40.99'	86
35	25°45.51'	83°41.20'	86
36	25°46.03'	83°41.45'	88
37	25°46.54'	83°41.73'	86
38	25°47.07'	83°42.04'	88
39*	25°47.53'	83°42.29'	86
40	25°48.04'	83°42.60'	88
41	25°48.54'	83°42.86'	86
42	25°49.04'	83°43.14'	88
43	25°49.56'	83°43.39'	90
44	25°50.02'	83°43.70'	90
45	25°50.52'	83°43.97'	91
46 DUD	25°51.01'	83°44.19'	93
47*	25°51.52'	83°44.37'	91
48	25°52.02'	83°44.59'	90
49	25°52.51'	83°44.81'	91
50	25°52.93'	83°44.99'	91
51	25°53.52'	83°45.20'	91
52	25°54.02'	83°45.47'	93
53	25°54.57'	83°45.79'	91
54	25°55.01'	83°46.01'	91
55	25°55.48'	83°46.22'	91
56	25°56.02'	83°46.47'	91
57	25°56.57'	83°46.76'	93
58	25°57.10'	83°46.99'	95
59	25°57.57'	83°47.19'	93
60	25°58.18'	83°47.47'	95
61	25°58.69'	83°47.71'	93

* Best estimate fix -- determined after the experiment by interpolation of available Loran-C and satellite data.

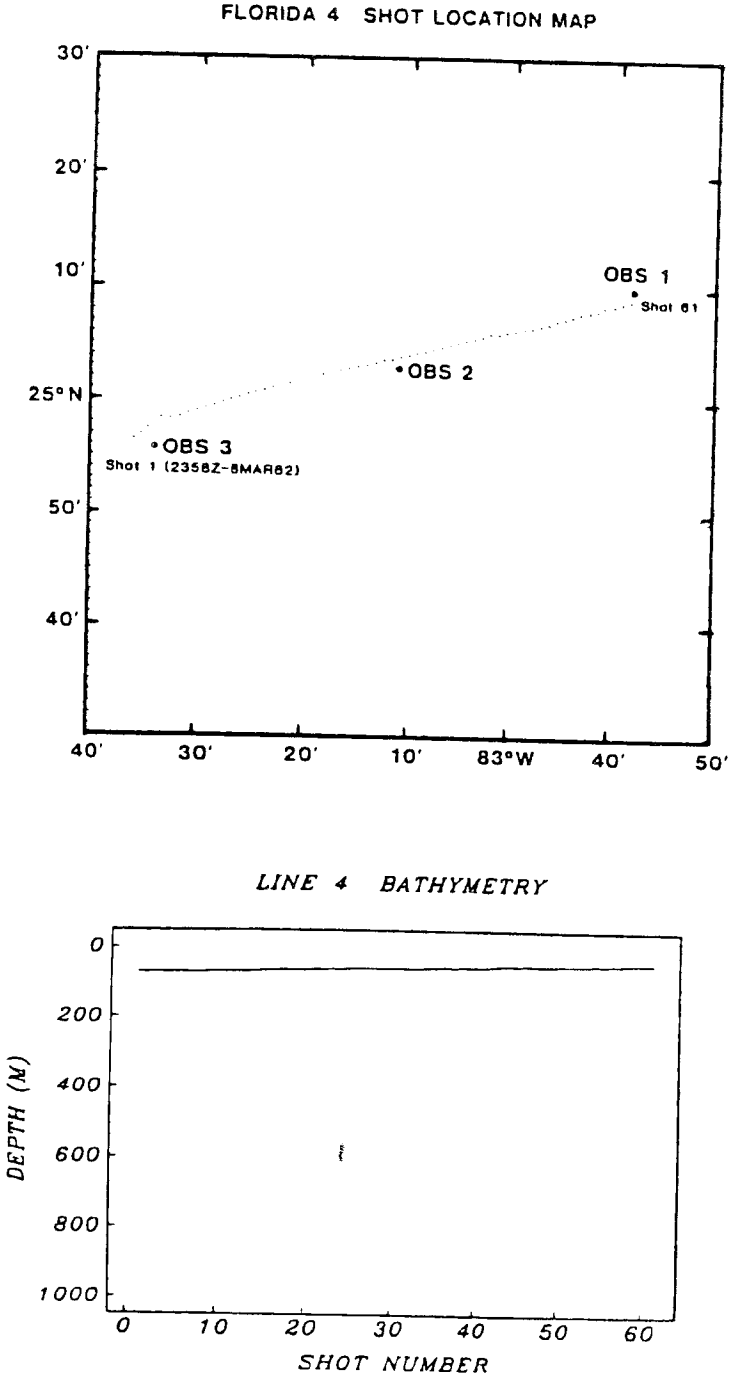

Figure A4. OBS and shot location details (top) and bathymetry (bottom) for Line 4.

TABLE A4. Line 4 shot coordinates and water depths.

SHOT	LATITUDE	LONGITUDE	WATER DEPTH(m)
1	24°56.45'	83°35.88'	70
2	24°56.91'	83°35.24'	70
3	24°57.44'	83°34.63'	71
4	24°58.01'	83°34.04'	70
5	24°58.36'	83°33.38'	70
6	24°58.27'	83°32.54'	70
7	24°58.46'	83°31.66'	70
8	24°58.77'	83°30.90'	70
9	24°59.02'	83°30.06'	68
10	24°59.25'	83°29.29'	68
11	24°59.46'	83°28.49'	68
12	24°59.77'	83°27.71'	68
13	24°59.98'	83°26.93'	68
14	25°00.21'	83°26.13'	68
15	25°00.50'	83°25.30'	66
16	25°00.71'	83°24.57'	66
17	25°00.86'	83°23.76'	64
18	25°01.13'	83°23.00'	64
19	25°01.33'	83°22.20'	64
20	25°01.50'	83°21.39'	64
21	25°01.67'	83°20.58'	62
22	25°01.89'	83°19.83'	62
23	25°02.12'	83°19.02'	62
24	25°02.30'	83°18.26'	62
25	25°02.46'	83°17.41'	60
26	25°02.68'	83°16.63'	60
27	25°02.84'	83°15.87'	60
28	25°03.02'	83°15.02'	59
29	25°03.15'	83°14.17'	59
30	25°03.33'	83°13.32'	59
31	25°03.61'	83°12.58'	59
32	25°03.68'	83°11.76'	59

Line 4 shot data (cont'd)

SHOT	LATITUDE	LONGITUDE	WATER DEPTH(m)
33	25°03.90'	83°10.93'	59
34	25°04.08'	83°10.16'	57
35	25°04.29'	83°09.39'	57
36	25°04.39'	83°08.54'	55
37	25°04.60'	83°07.80'	57
38	25°04.81'	83°06.93'	55
39	25°05.03'	83°06.16'	55
40	25°05.23'	83°05.36'	55
41	25°05.46'	83°04.58'	55
42	25°05.59'	83°03.69'	53
43	25°05.78'	83°02.88'	51
44	25°06.07'	83°02.10'	51
45	25°06.08'	83°01.25'	51
46	25°06.25'	83°00.45'	49
47	25°06.39'	82°59.63'	51
48	25°06.56'	82°58.78'	51
49	25°06.65'	82°57.91'	51
50	25°06.86'	82°57.12'	49
51	25°07.04'	82°56.31'	49
52	25°07.33'	82°55.55'	48
53	25°07.53'	82°54.72'	48
54	25°07.74'	82°53.98'	46
55	25°07.95'	82°53.16'	48
56	25°08.12'	82°52.28'	46
57	25°08.24'	82°51.52'	46
58	25°08.58'	82°50.85'	44
59	25°08.70'	82°49.93'	44
60	25°08.91'	82°49.12'	44
61	25°09.12'	82°48.32'	44

*Best estimate fix -- determined after the experiment by interpolation of available Loran-C and satellite data.

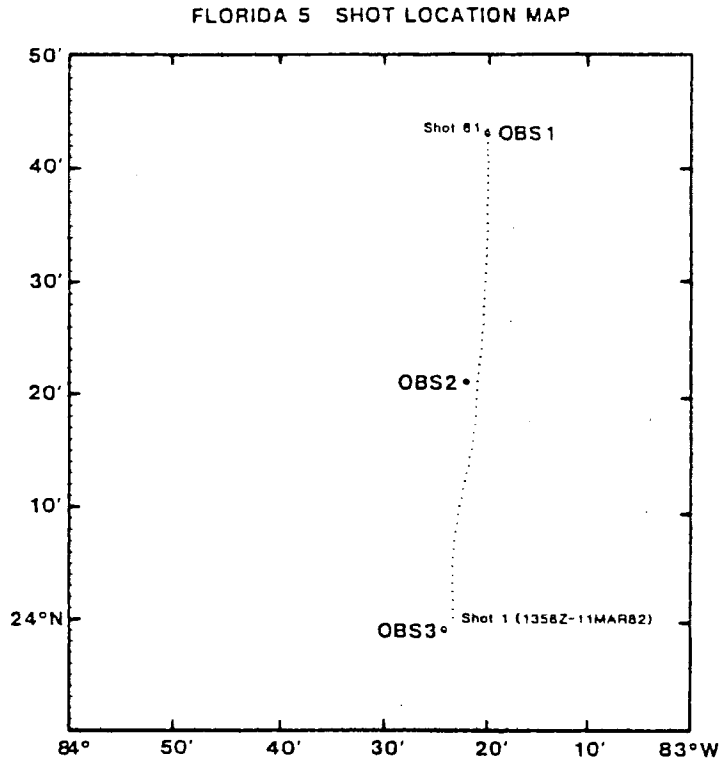

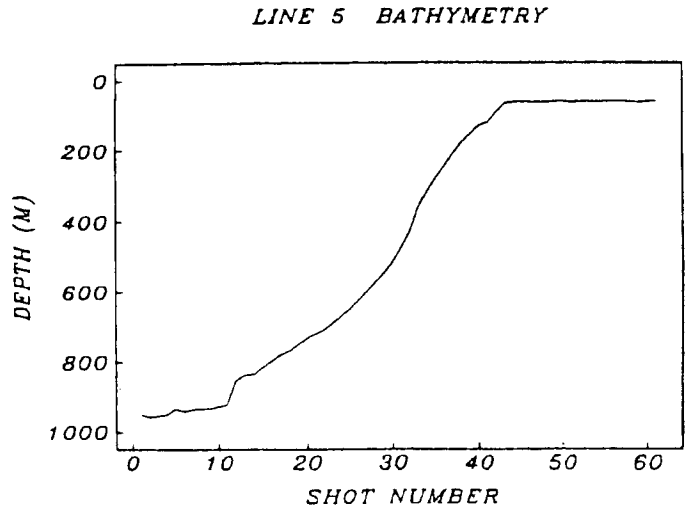

Figure A5. OBS and shot location details (top) and bathymetry (bottom) for Line 5.

TABLE A5. Line 5 shot coordinates and water depths.

SHOT	LATITUDE	LONGTIDUE	WATER DEPTH(m)
1	24°00.12'	83°23.31'	951
2	24°00.89'	83°23.33'	957
3	24°01.69'	83°23.30'	953
4	24°02.48'	83°23.35'	949
5	24°03.24'	83°23.35'	933
6	24°03.95'	83°23.36'	940
7	24°04.76'	83°23.36'	935
8	24°05.53'	83°23.31'	931
9	24°06.30'	83°23.27'	933
10	24°07.03'	83°23.17'	925
11	24°07.80'	83°23.06'	920
12	24°08.55'	83°22.89'	850
13	24°09.37'	83°22.81'	836
14	24°10.09'	83°22.65'	832
15	24°10.77'	83°22.48'	814
16	24°11.56'	83°22.38'	796
17	24°12.28'	83°22.18'	779
18	24°12.98'	83°21.99'	768
19	24°13.62'	83°21.82'	750
20	24°14.39'	83°21.69'	732
21	24°15.11'	83°21.51'	721
22	24°15.83'	83°21.42'	710
23	24°16.54'	83°21.30'	690
24	24°17.25'	83°21.21'	668
25	24°18.05'	83°21.12'	649
26	24°18.83'	83°21.11'	622
27	24°19.57'	83°21.07'	598
28	24°20.30'	83°21.01'	571
29	24°21.06'	83°20.99'	543
30	24°21.79'	83°20.87'	512
31	24°22.56'	83°20.78'	470

Line 5 shot data (cont'd)

SHOT	LATITUDE	LONGITUDE	WATER DEPTH(m)
32	24°23.27'	83°20.67'	428
33	24°24.00'	83°20.59'	358
34	24°24.75'	83°20.53'	315
35	24°25.45'	83°20.50'	278
36	24°26.22'	83°20.38'	243
37	24°27.02'	83°20.36'	207
38	24°27.78'	83°20.37'	179
39	24°28.48'	83°20.29'	154
40	24°29.26'	83°20.25'	130
41	24°29.99'	83°20.20'	121
42	24°30.78'	83°20.16'	90
43	24°31.58'	83°20.15'	66
44	24°32.27'	83°20.09'	64
45	24°33.01'	83°20.06'	62
46	24°33.77'	83°20.03'	64
47*	24°34.50'	83°19.99'	64
48	24°35.18'	83°19.98'	64
49	24°35.99'	83°20.02'	62
50	24°36.76'	83°20.02'	62
51	24°37.40'	83°19.95'	64
52	24°38.07'	83°19.95'	62
53	24°38.67'	83°19.94'	62
54	24°39.31'	83°19.94'	64
55	24°39.91'	83°19.94'	62
56	24°40.51'	83°19.92'	62
57	24°41.09'	83°19.97'	62
58	24°41.61'	83°19.99'	64
59	24°42.19'	83°19.95'	64
60	24°42.81'	83°19.99'	62
61	24°43.39'	83°19.96'	62

* Best estimate fix -- determined after the experiment by interpolation of available Loran-C and satellite data.

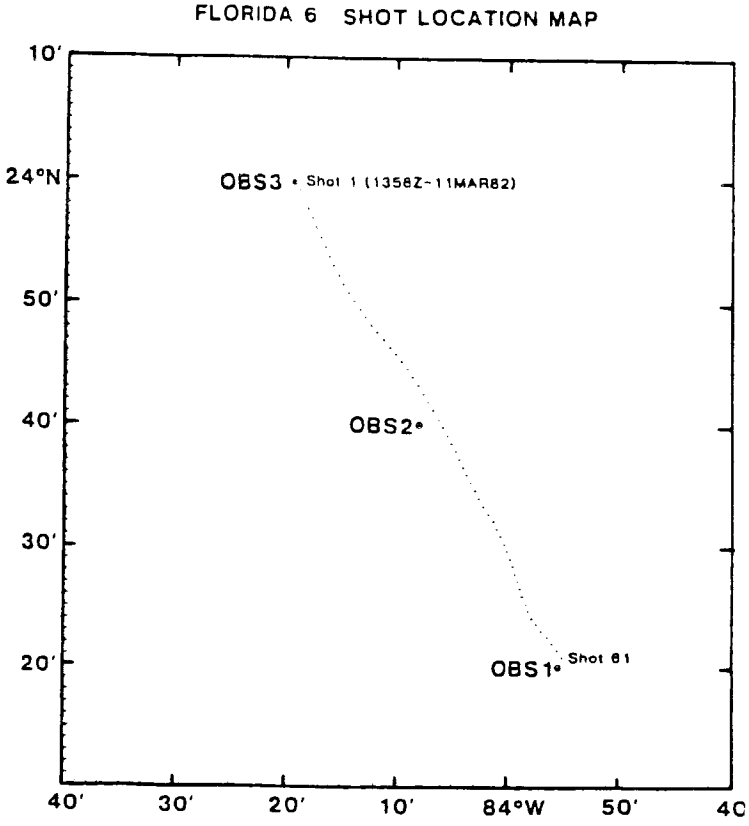

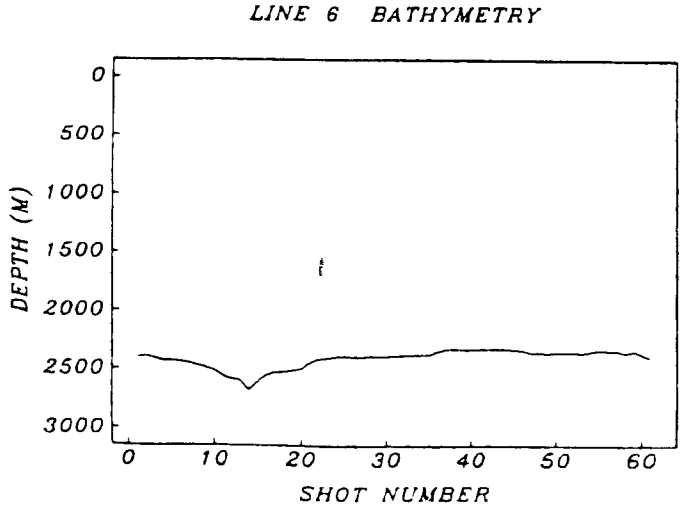

Figure A6. OBS and shot location details (top) and bathymetry (bottom) for Line 6.

TABLE A6. Line 6 shot coordinates and water depths.

SHOT	LATITUDE	LONGITUDE	WATER DEPTH(m)
1	23°59.92'	84°19.05'	2396
2	23°59.21'	84°18.69'	2383
3	23°58.47'	84°18.30'	2405
4*	23°57.72'	84°17.95'	2427
5	23°56.95'	84°17.55'	2425
6 DUD	23°56.23'	84°17.17'	2429
7	23°55.39'	84°16.76'	2444
8	23°54.62'	84°16.36'	2464
9	23°53.84'	84°15.98'	2487
10	23°53.10'	84°15.58'	2509
11	23°52.31'	84°15.14'	2551
12*	23°51.60'	84°14.67'	2579
13	23°50.88'	84°14.21'	2588
14	23°50.22'	84°13.70'	2676
15	23°49.54'	84°13.13'	2610
16	23°48.95'	84°12.68'	2544
17	23°48.29'	84°12.14'	2520
18	23°47.69'	84°11.63'	2519
19	23°47.09'	84°11.05'	2509
20	23°46.40'	84°10.44'	2495
21	23°45.87'	84°09.99'	2444
22	23°45.24'	84°09.47'	2412
23	23°44.62'	84°08.94'	2403
24	23°43.94'	84°08.45'	2392
25	23°43.29'	84°07.96'	2385
26	23°42.60'	84°07.48'	2391
27	23°41.94'	84°07.05'	2391
28	23°41.30'	84°06.63'	2385
29	23°40.51'	84°06.14'	2385
30	23°39.90'	84°05.73'	2383
31	23°39.22'	84°05.36'	2380
32	23°38.56'	84°04.97'	2376

Line 6 shot data (cont'd)

SHOT	LATITUDE	LONGITUDE	WATER DEPTH(m)
33	23°37.91'	84°04.60'	2374
34	23°37.23'	84°04.26'	2372
35	23°36.59'	84°03.91'	2369
36	23°35.97'	84°03.58'	2341
37	23°35.34'	84°03.24'	2321
38	23°34.69'	84°02.88'	2319
39	23°34.08'	84°02.52'	2323
40	23°33.44'	84°02.11'	2323
41	23°32.80'	84°01.67'	2319
42	23°32.23'	84°01.25'	2319
43	23°31.61'	84°00.90'	2319
44	23°31.00'	84°00.54'	2317
45	23°30.38'	84°00.23'	2325
46	23°29.77'	83°59.96'	2328
47	23°29.11'	83°59.68'	2352
48	23°28.50'	83°59.44'	2354
49	23°27.86'	83°59.25'	2359
50	23°27.24'	83°59.03'	2350
51	23°26.62'	83°58.82'	2354
52	23°25.98'	83°58.60'	2354
53	23°25.33'	83°58.28'	2358
54	23°24.76'	83°58.05'	2347
55	23°24.15'	83°57.74'	2332
56	23°23.68'	83°57.33'	2337
57	23°23.11'	83°56.85'	2339
58	23°22.59'	83°56.32'	2359
59	23°22.06'	83°55.88'	2339
60	23°21.49'	83°55.41'	2372
61	23°20.91'	83°54.96'	2396

* Best estimate fix -- determined after the experiment by interpolation of available Loran-C and satellite data.

APPENDIX B

Filtered record sections

This appendix contains a complete set of seismic record sections made with the 4.5 Hz geophone OBS units from Lines 1-6. Each section has been amplitude trace-gained and filtered using 2.5-8 Hz minimum phase filter as discussed in the text.

Line 1 52

Line 2 54

Line 3 57

Line 4 59

Line 5 62

Line 6 65

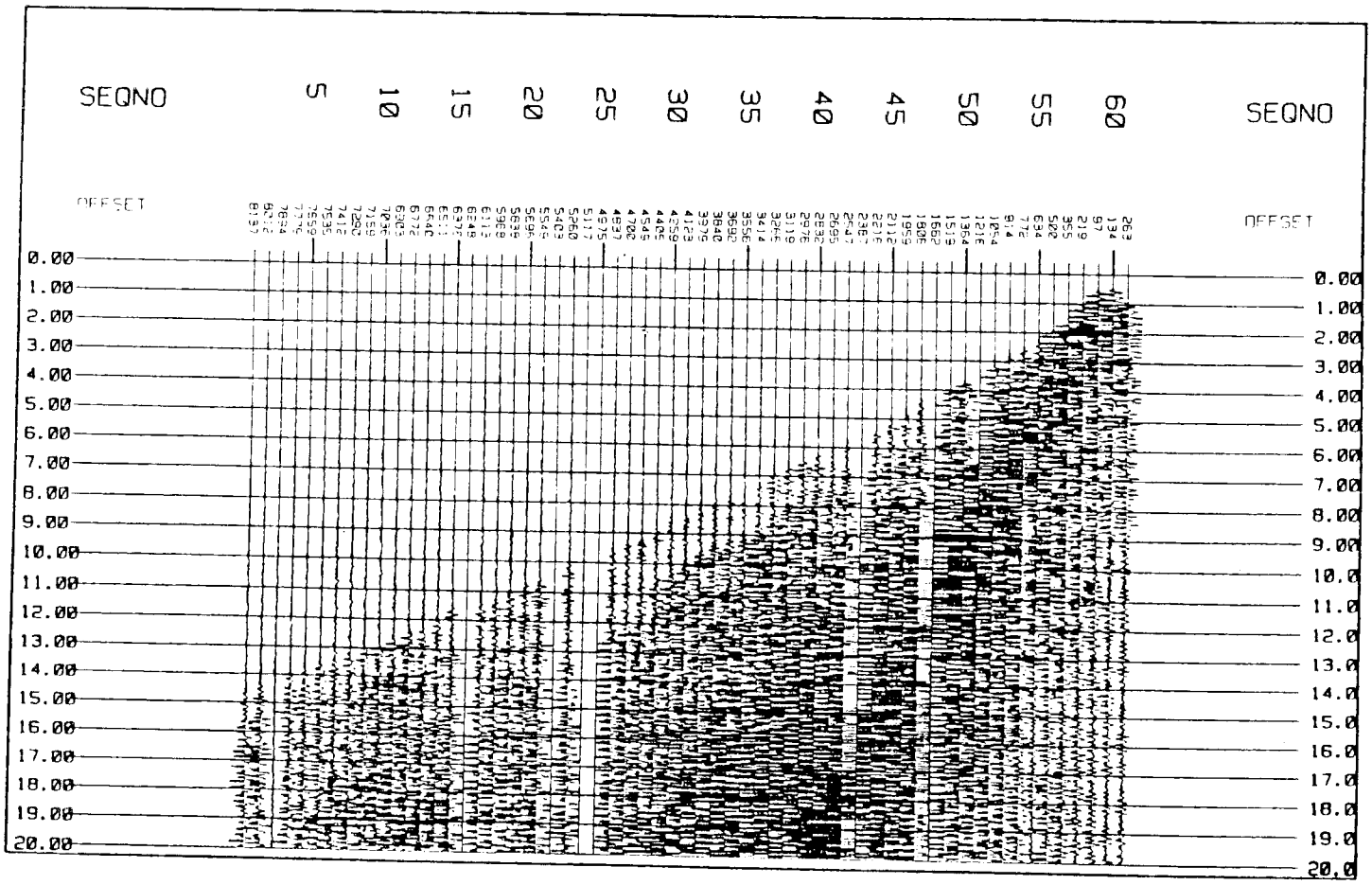

Figure B1. Amplitude gained and filtered data for Line 1, OBS 1.

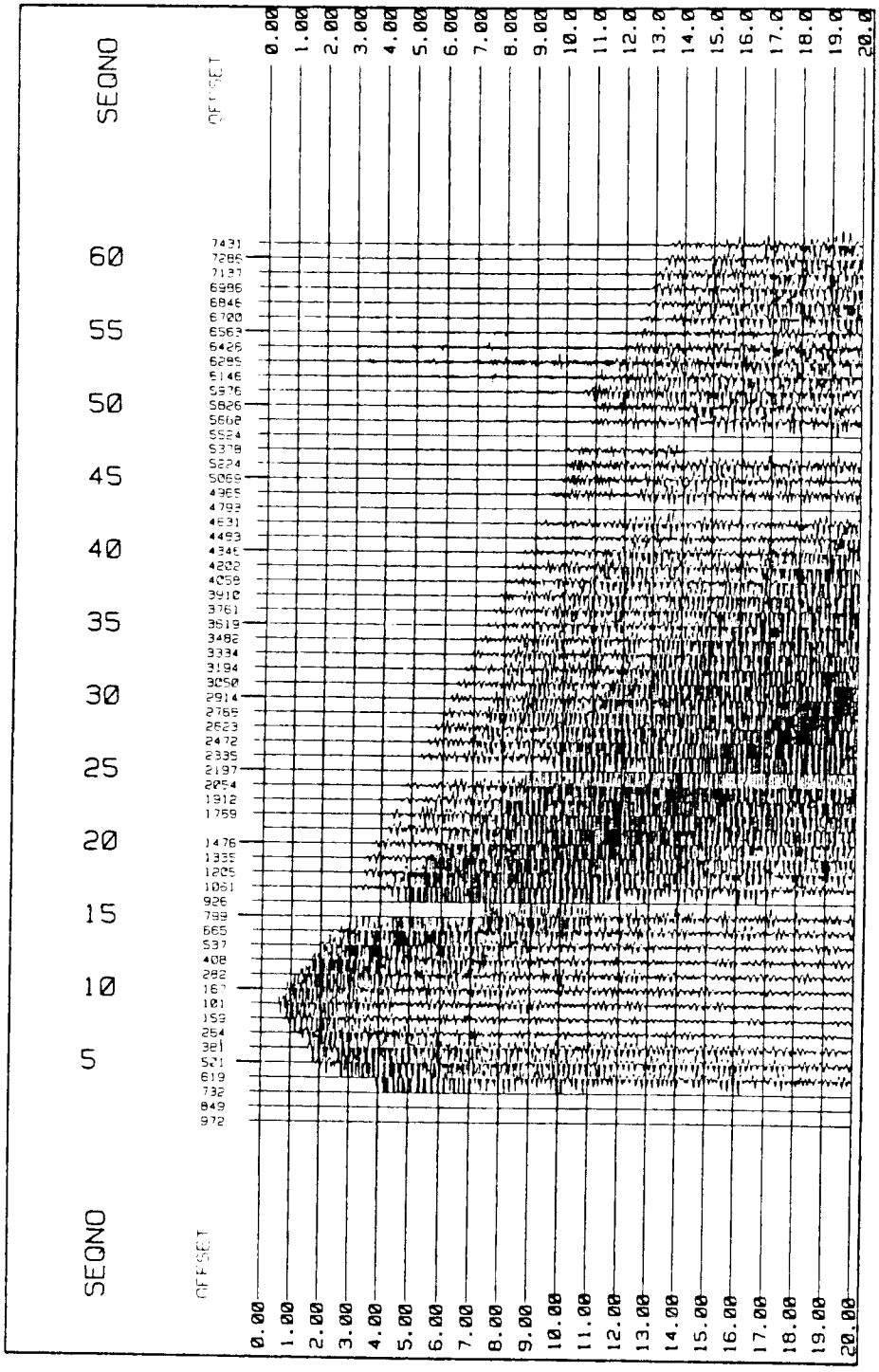

Figure B2. Amplitude gained and filtered data for Line 1, OBS 3.

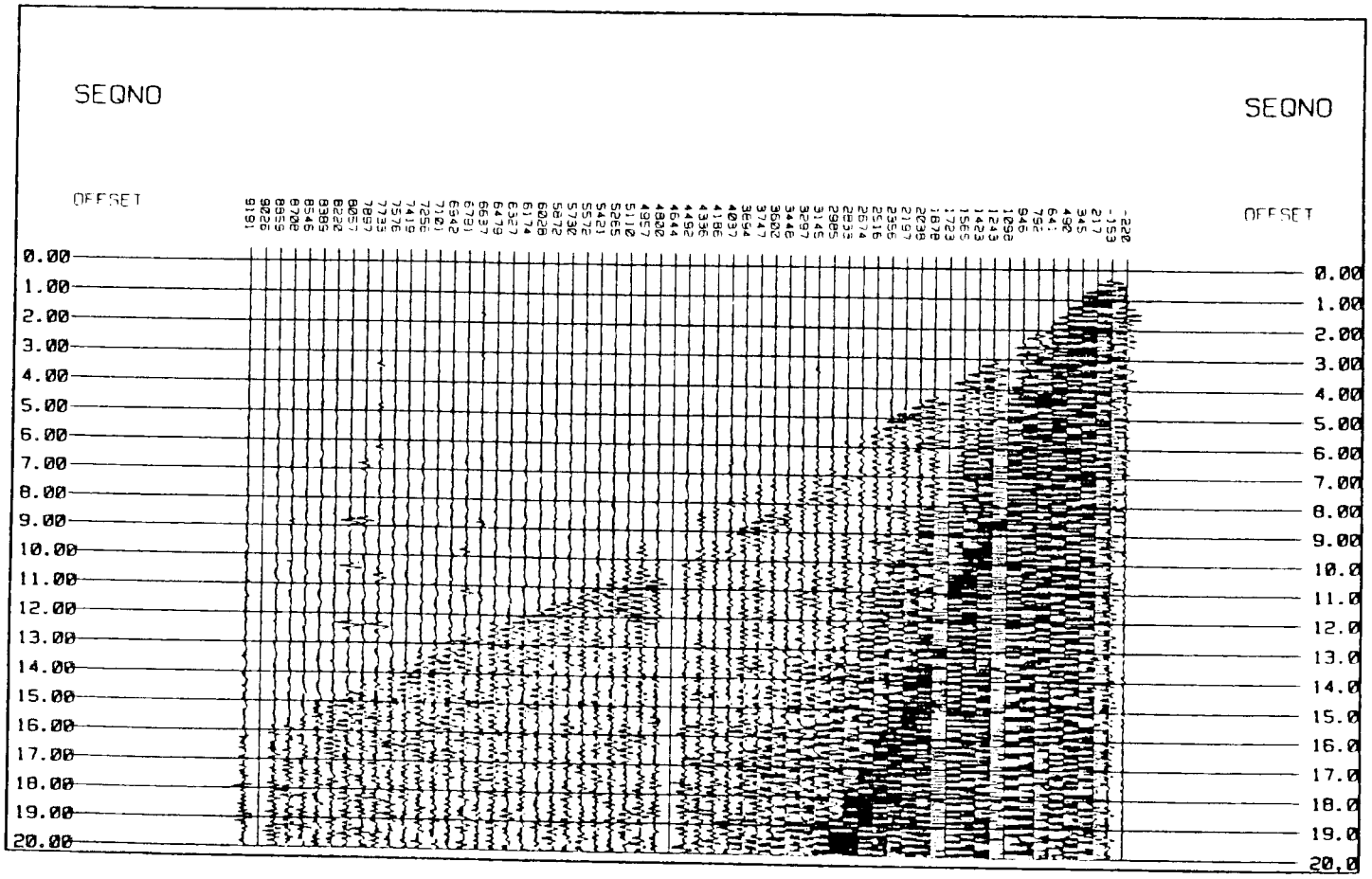

Figure B3. Amplitude gained and filtered data for Line 2, OBS 1.

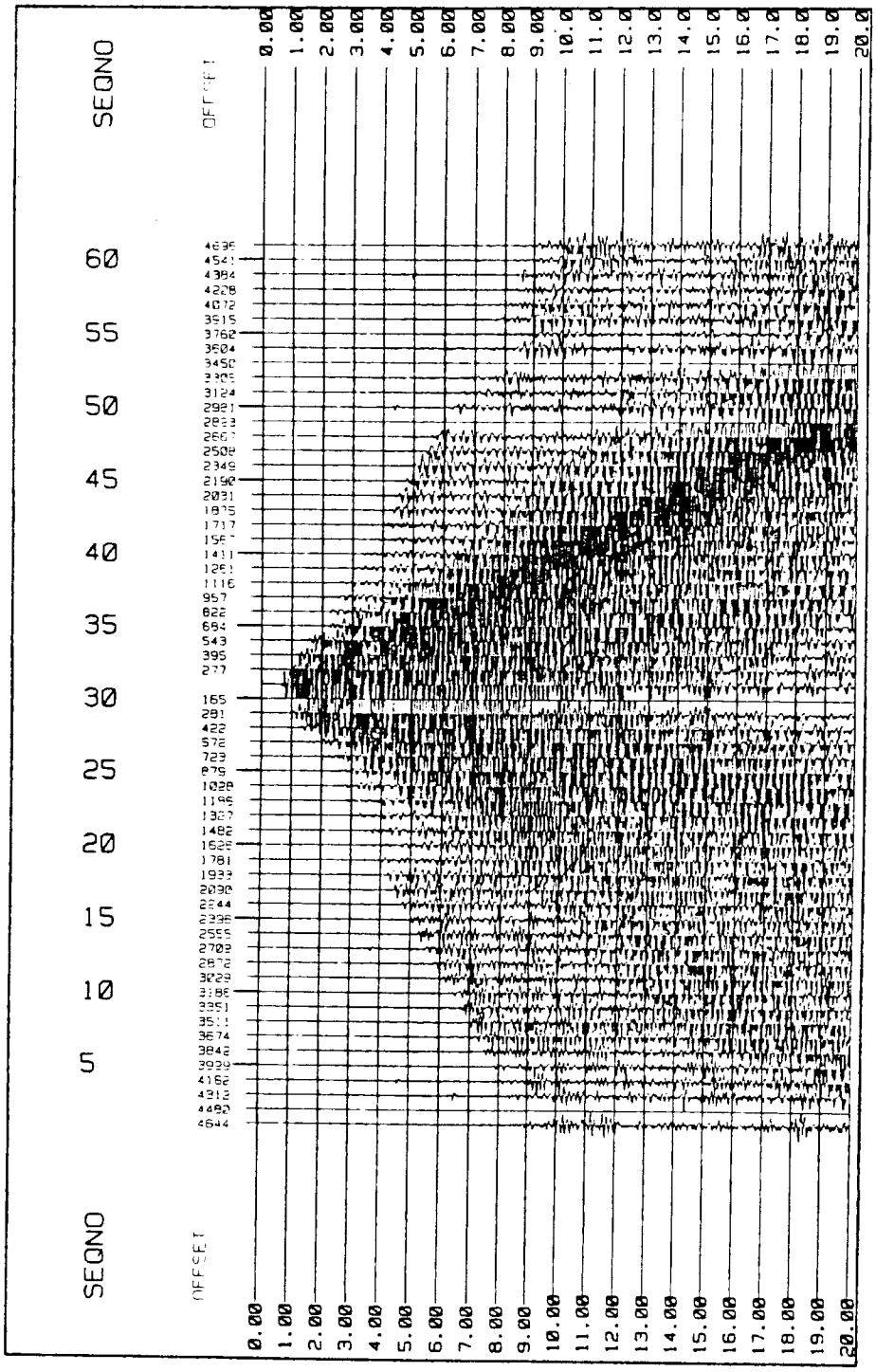

Figure B4. Amplitude gained and filtered data for Line 2, OBS 2.

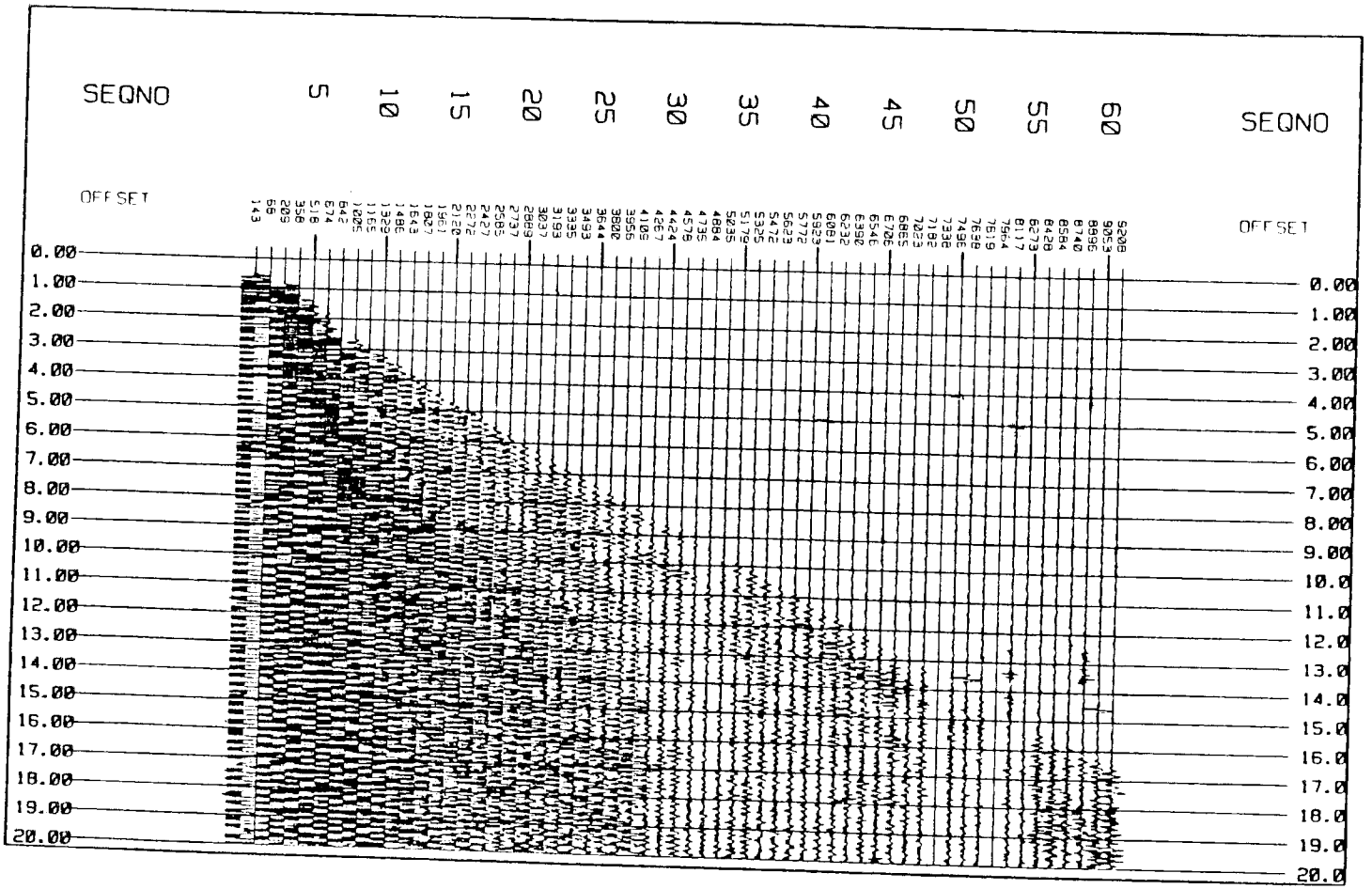

Figure B5. Amplitude gained and filtered data for Line 2, OBS 3.

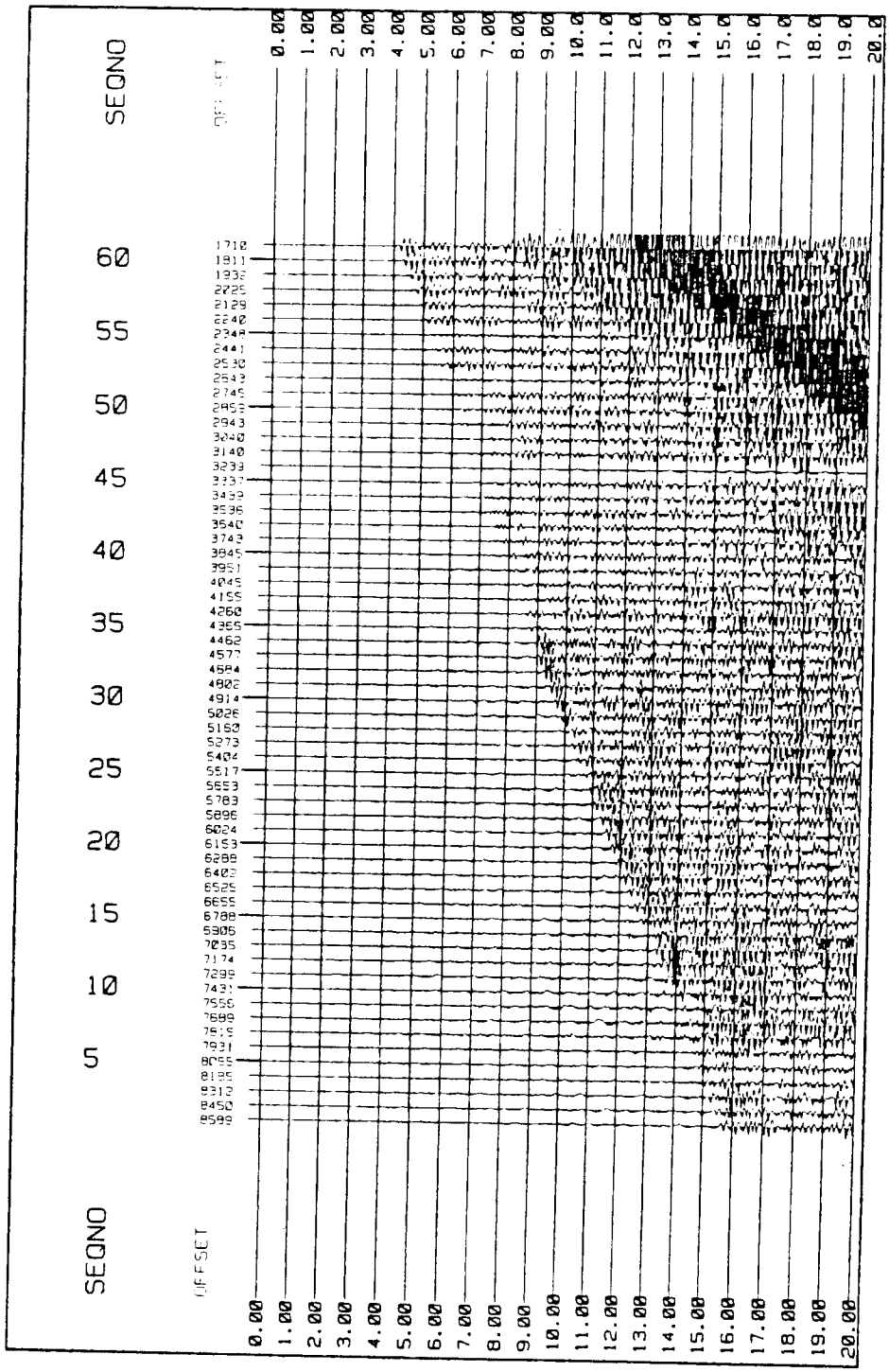

Figure B6. Amplitude gained and filtered data for Line 3, OBS 1.

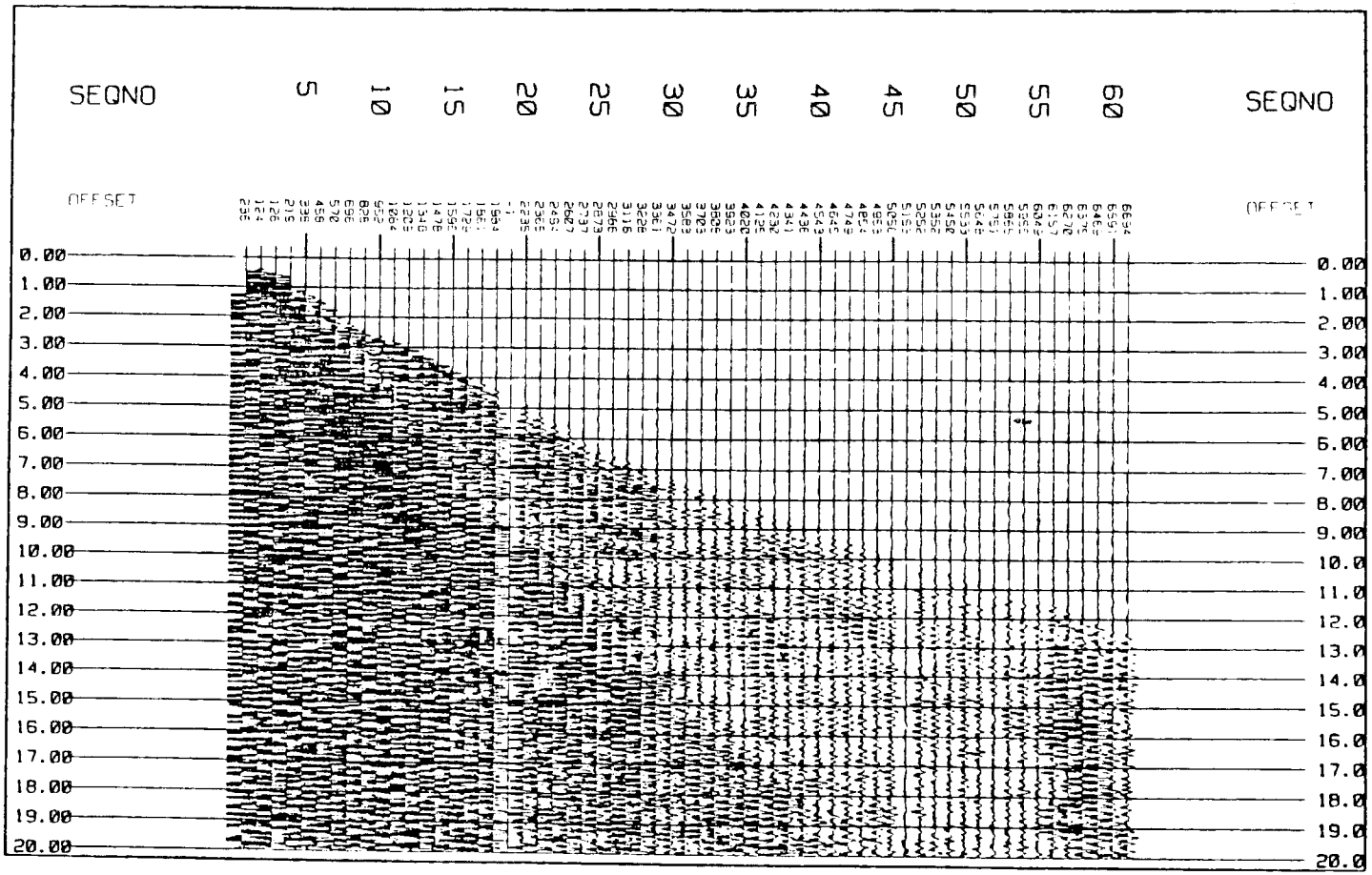

Figure B7. Amplitude gained and filtered data for Line 3, OBS 3.

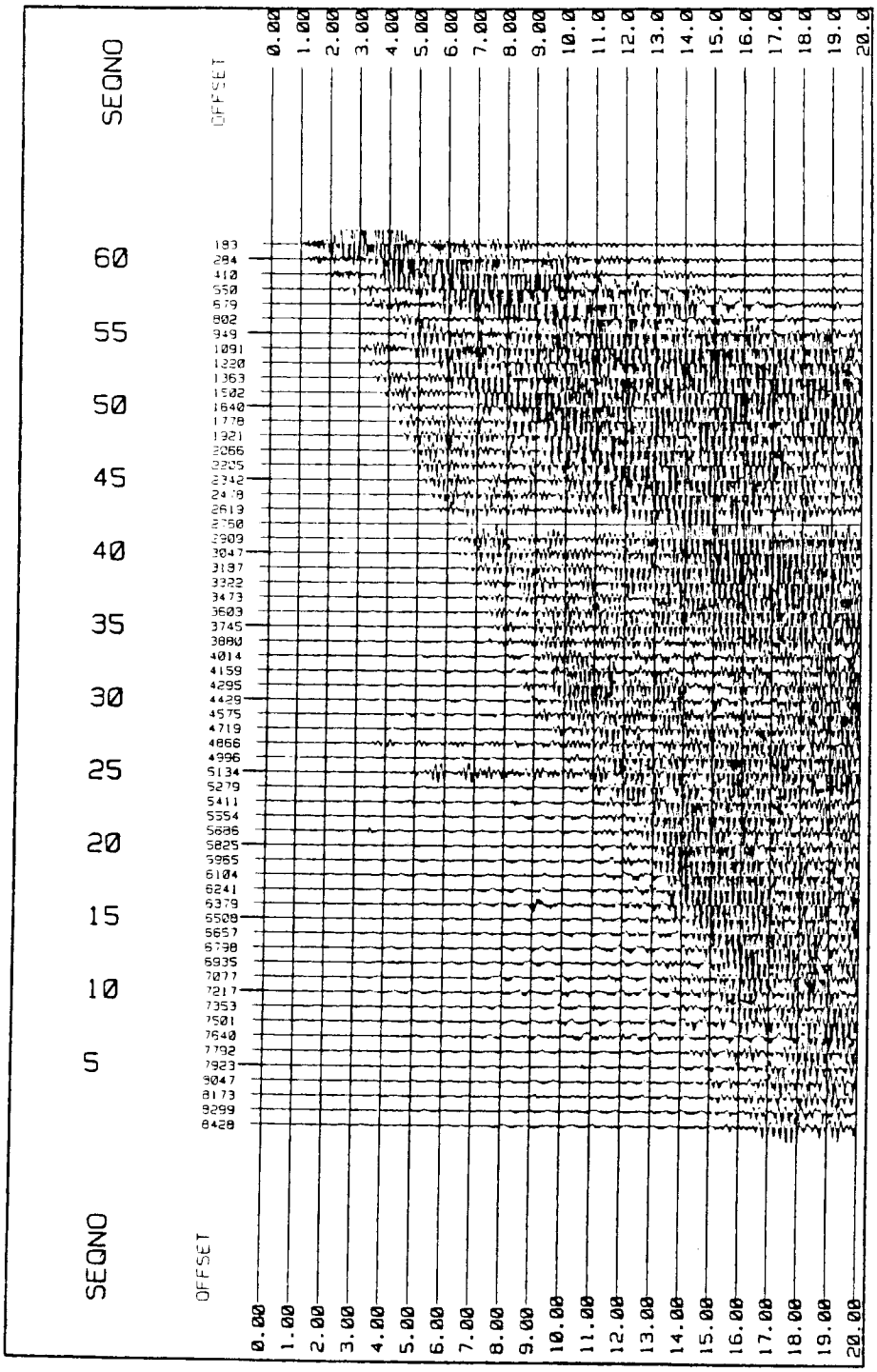

Figure B8. Amplitude gained and filtered data for Line 4, OBS 1.

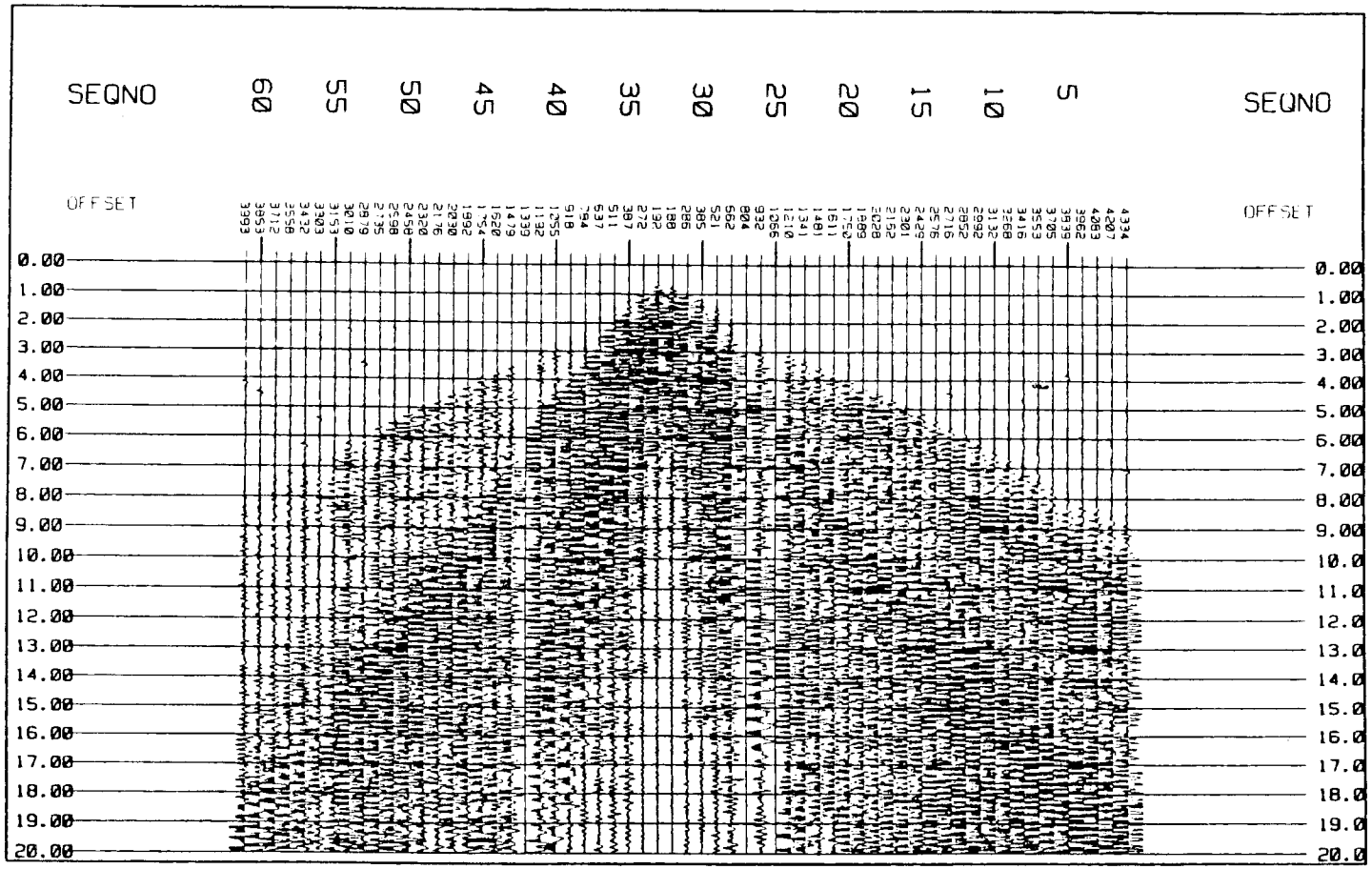

Figure B9. Amplitude gained and filtered data for Line 4, OBS 2.

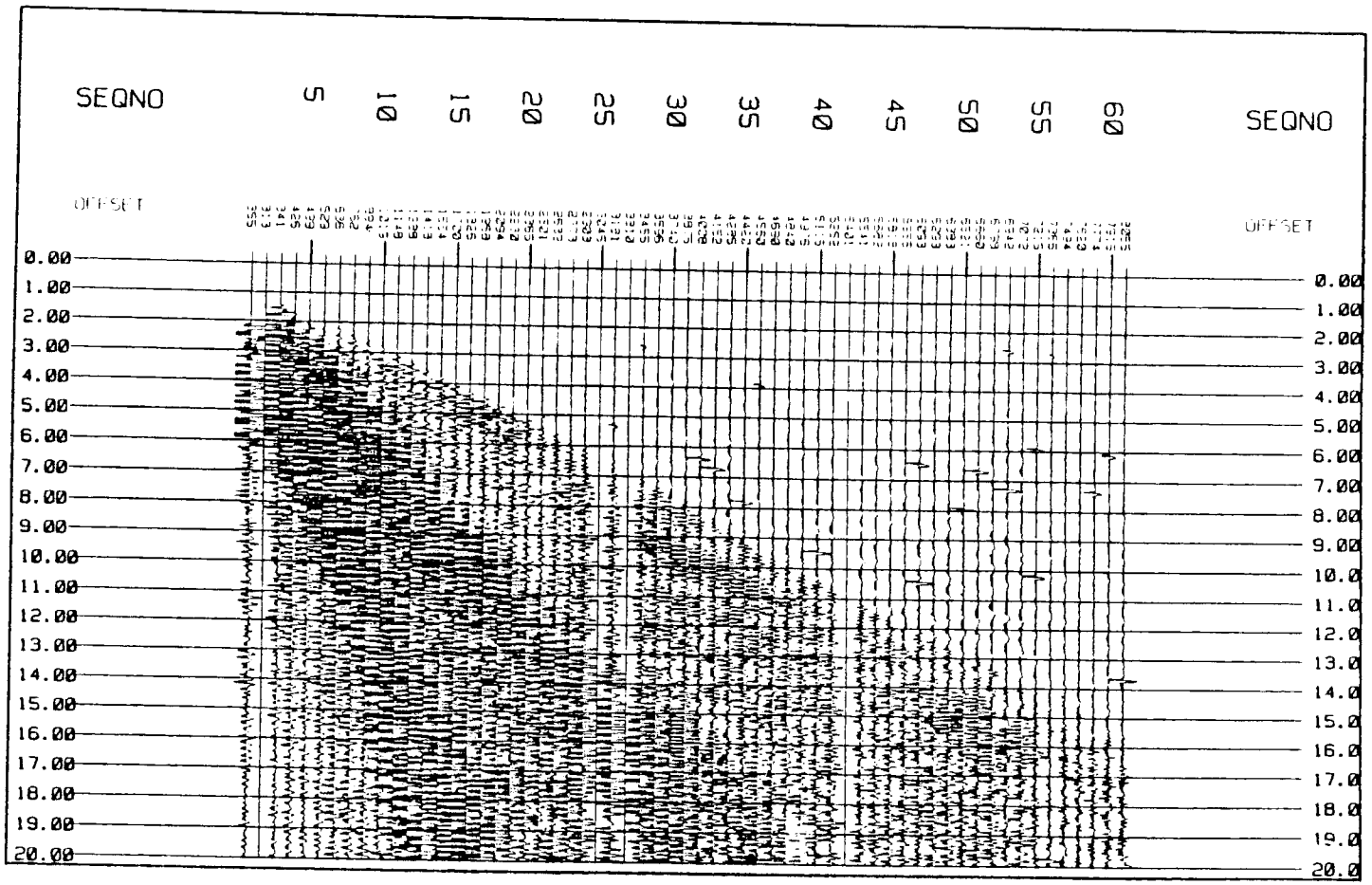

Figure B10. Amplitude gained and filtered data for Line 4, OBS 3.

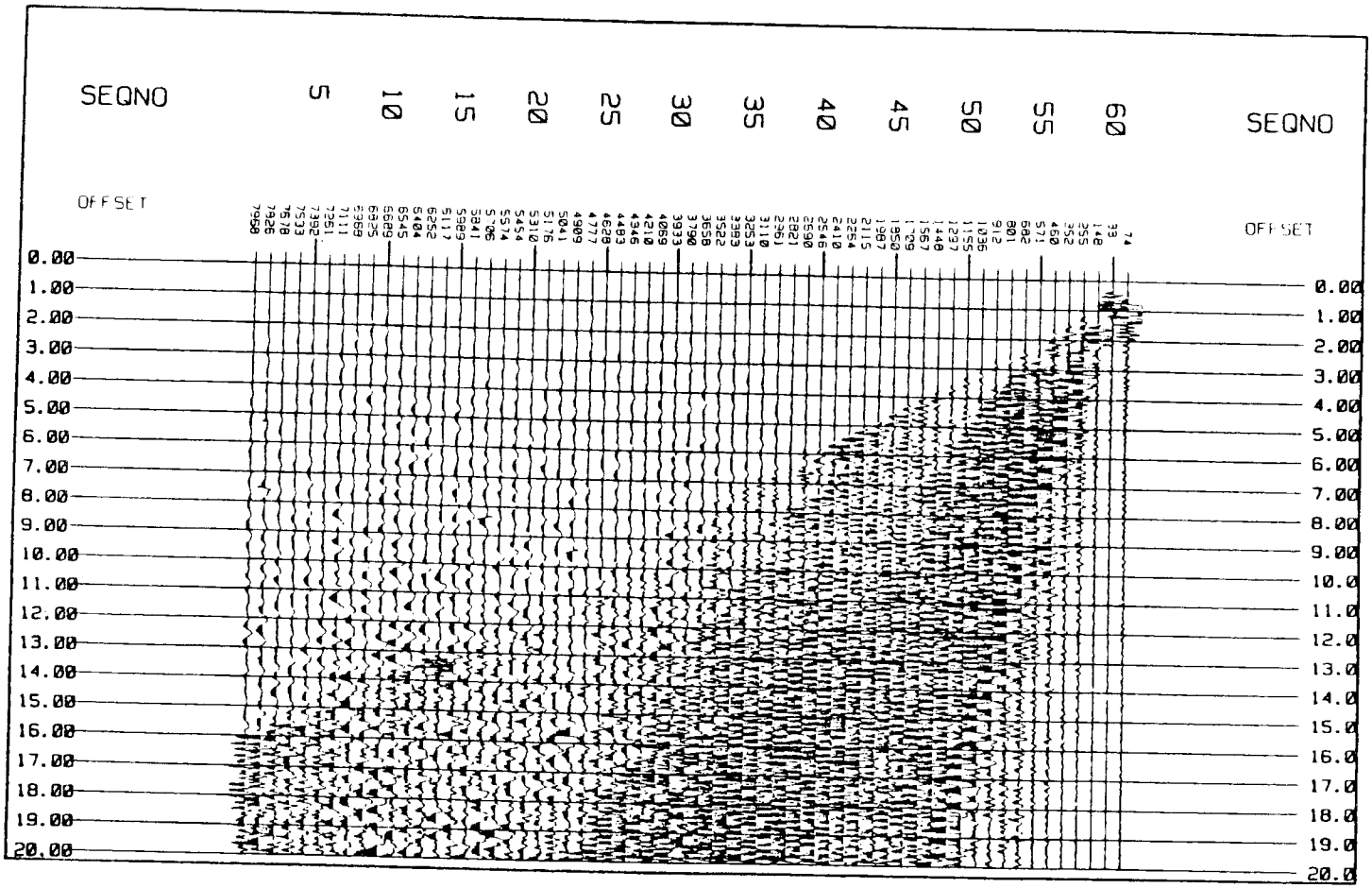

Figure B11. Amplitude gained and filtered data for Line 5, OBS 1.

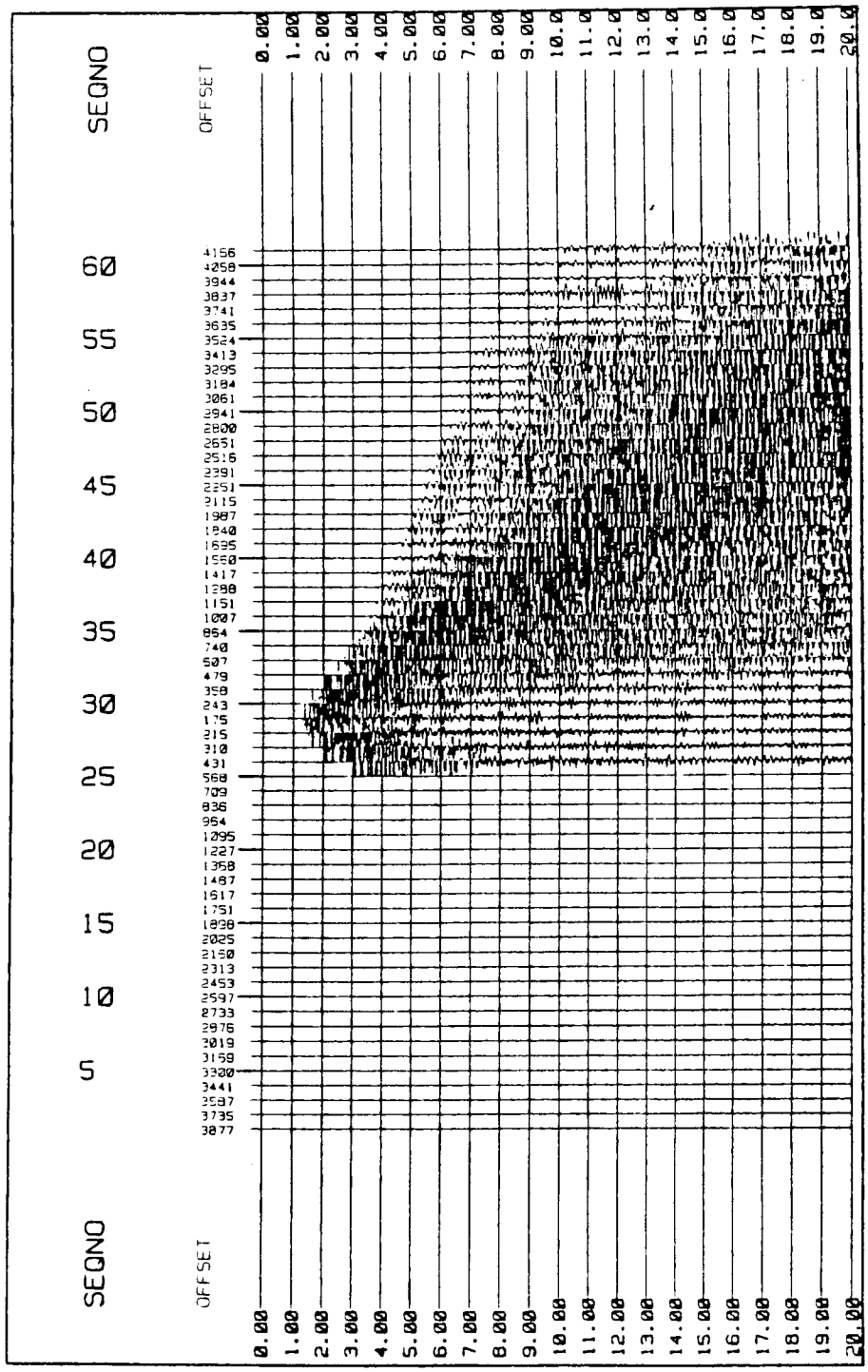

Figure B12. Amplitude gained and filtered data for Line 5, OBS 2.

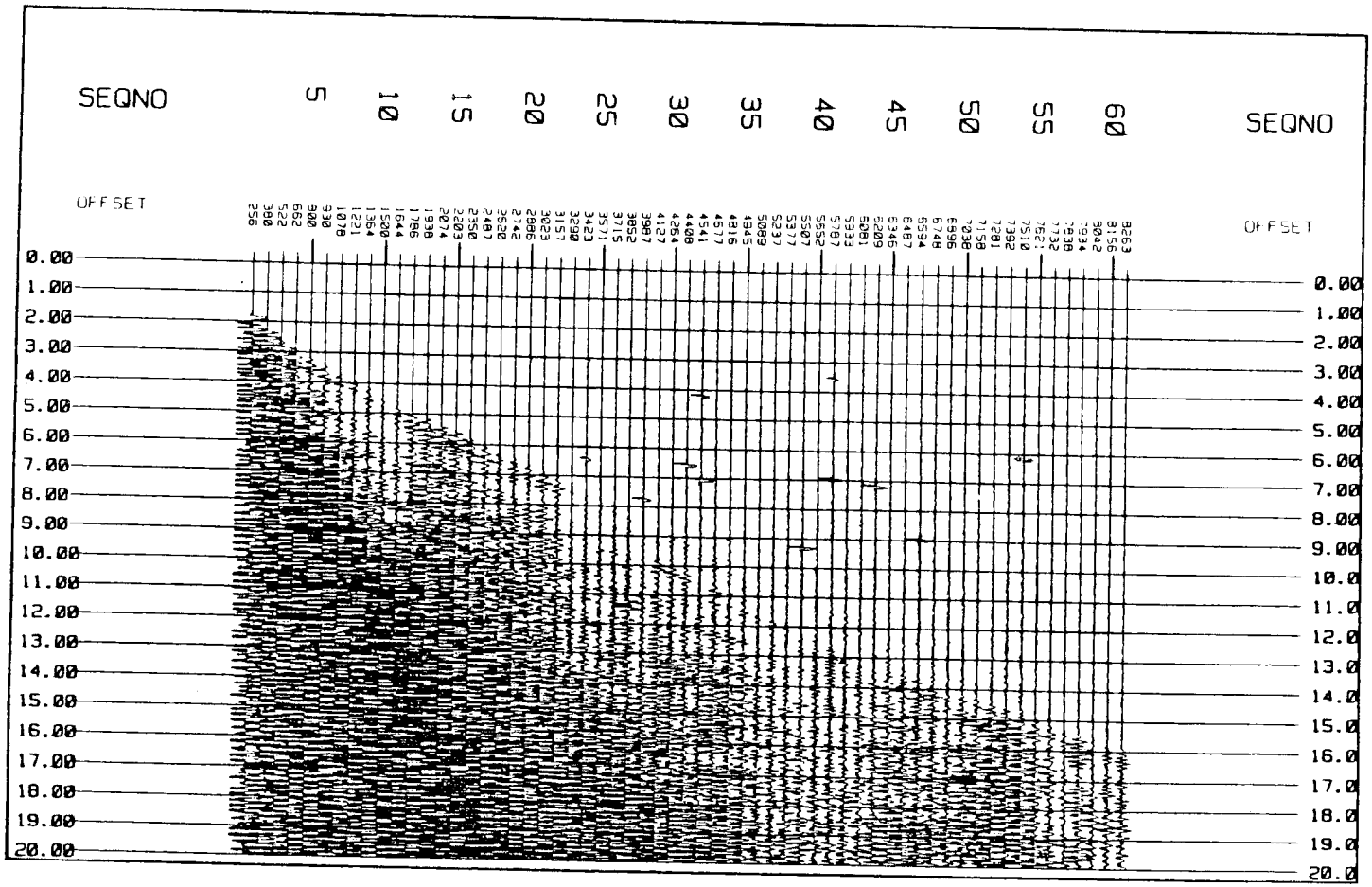

Figure B13. Amplitude gained and filtered data for Line 5, OBS 3.

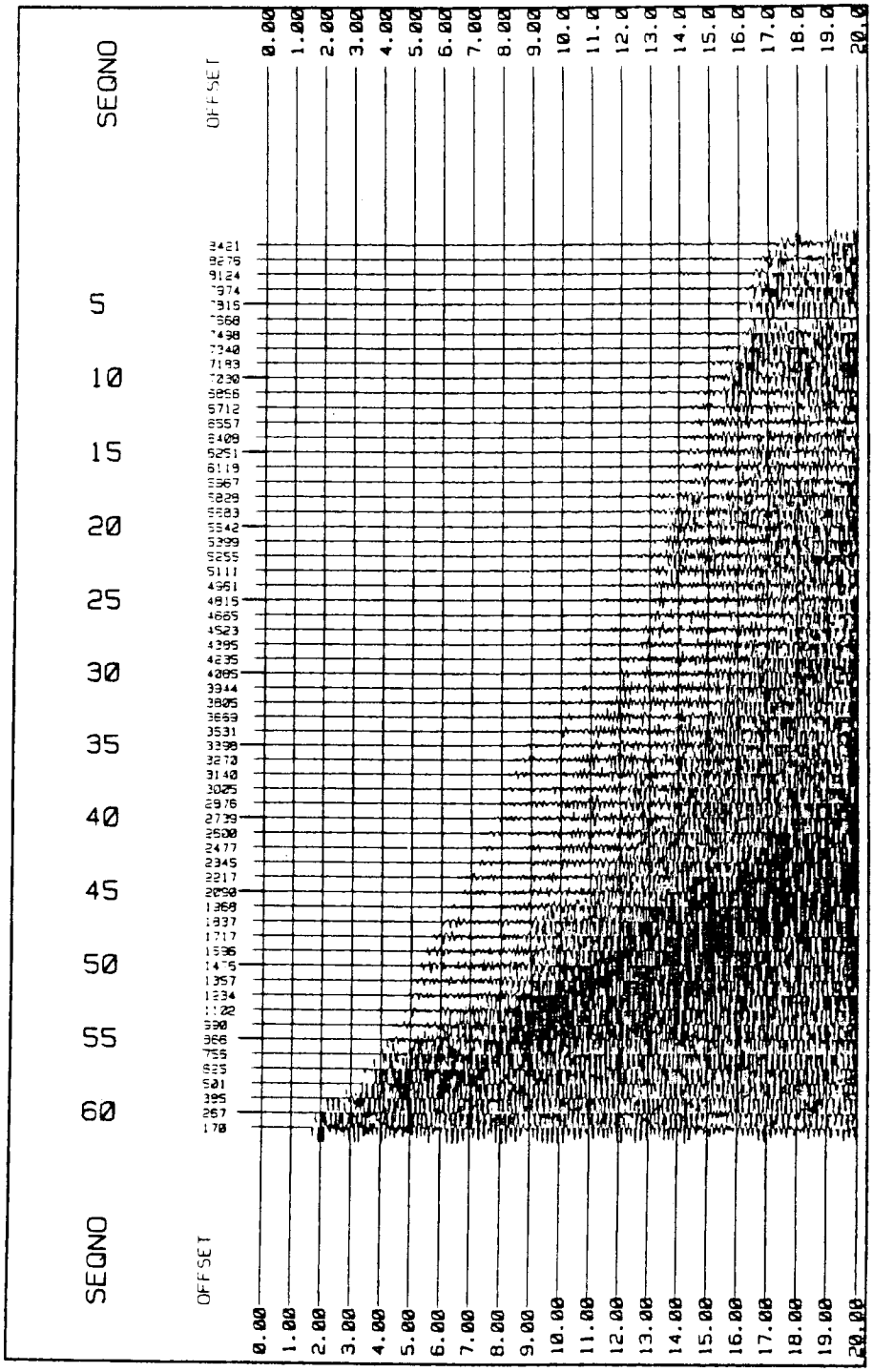

Figure B14. Amplitude gained and filtered data for Line 6, OBS 1.

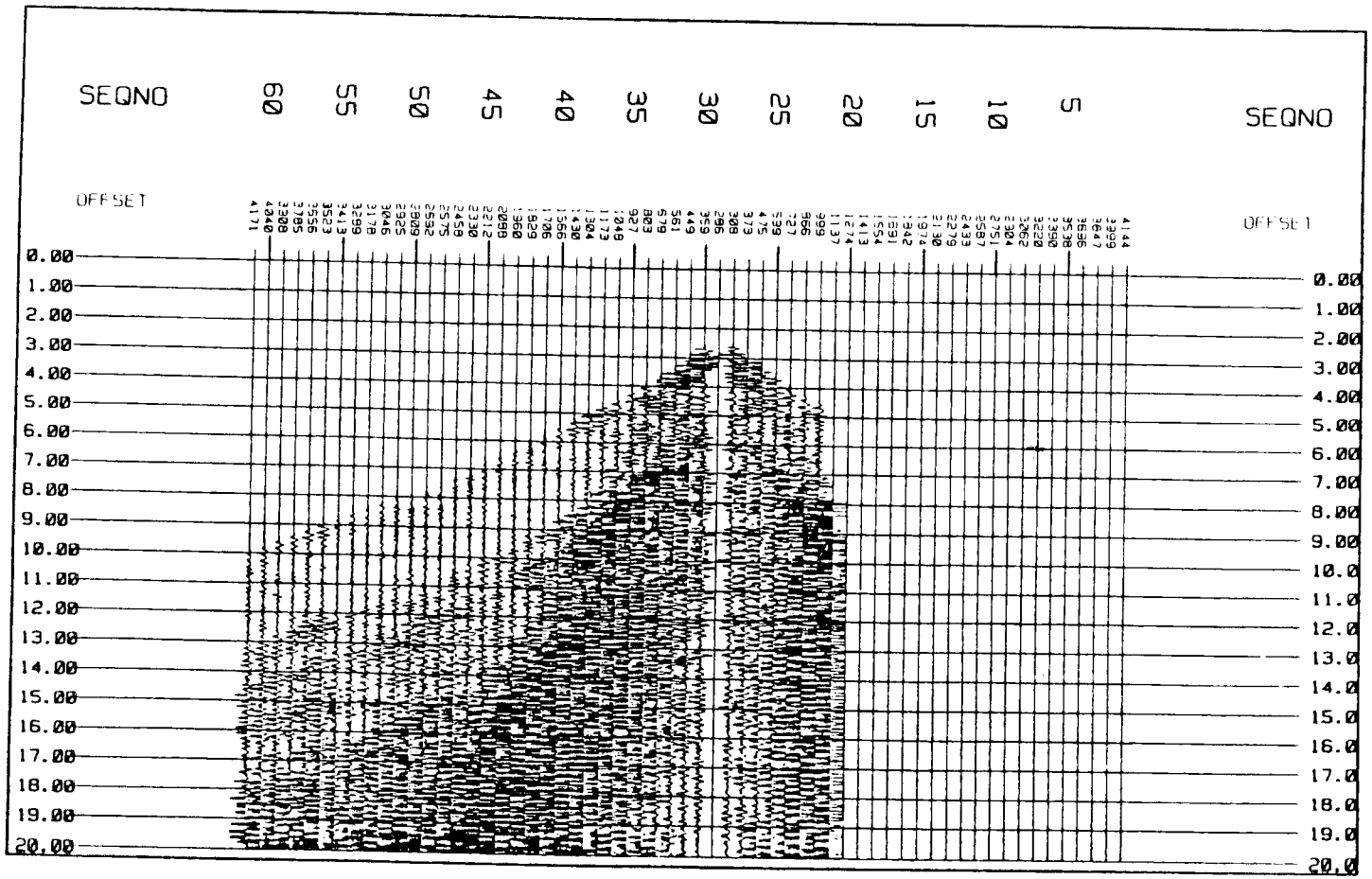

Figure B15. Amplitude gained and filtered data for Line 6, OBS 2.

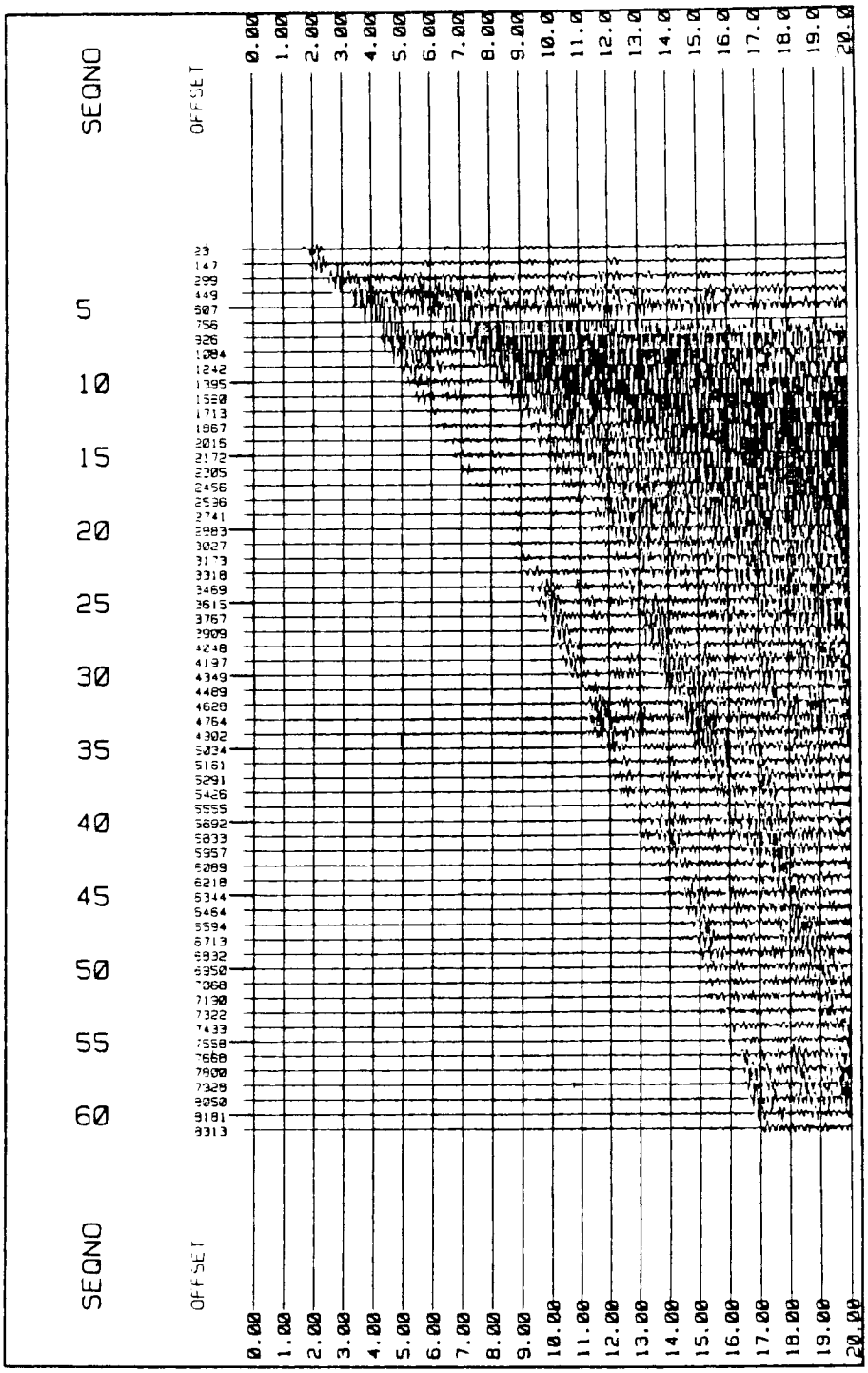

Figure B16. Amplitude gained and filtered data for Line 6, OBS 3.

APPENDIX C

Tables of Arrival Picks and Travel-time Curves

Line 1 69

Line 2 71

Line 3 73

Line 4 75

Line 5 77

Line 6 79

TABLE C1. Distance and time picks for Line 1.

OBS 1

OFFSET(KM)	ARRIVAL TIME(SEC)
0.97	0.52
2.19	1.03
3.55	1.47
5.00	1.92
6.34	2.33
7.72	2.80
5.00	1.97
6.34	2.28
7.72	2.57
9.14	2.88
10.54	3.17
13.64	3.75
19.59	5.00
21.12	5.28
22.16	5.58
9.14	3.00
13.64	3.75
15.19	3.97
18.06	4.63
19.59	4.77
21.12	5.07
22.16	5.28
25.47	5.75
26.95	6.10
28.32	6.43
31.19	6.98
25.47	5.87
26.95	6.09
28.32	6.33
29.76	6.58
31.19	6.80
32.66	7.02
34.14	7.22
35.56	7.42
36.92	7.64
38.40	7.91
39.79	8.09
41.23	8.31
42.59	8.58
44.05	8.80
45.49	9.02
47.00	9.24
48.37	9.47
52.60	10.18
55.49	10.67
56.96	10.87
58.38	11.11
59.68	11.27
61.13	11.56
59.68	11.58
65.11	12.07
66.40	12.29
67.72	12.49
69.03	12.71
70.36	12.89
71.59	13.07
72.90	13.28
74.12	13.50
75.35	13.63
76.59	13.83
77.79	14.00
80.12	14.40
81.37	14.60

OBS 3

OFFSET(KM)	ARRIVAL TIME(SEC)
1.67	0.77
2.82	1.23
4.08	1.68
6.65	2.60
1.67	0.83
2.82	1.28
4.08	1.63
5.37	1.92
6.65	2.21
5.37	1.97
6.65	2.17
10.61	3.00
13.35	3.50
14.76	3.77
17.69	4.27
19.12	4.53
20.54	5.03
23.35	5.35
24.72	5.63
26.23	5.87
27.68	6.17
29.14	6.37
30.50	6.60
33.34	7.05
37.61	7.93
40.58	8.40
42.02	8.70
46.31	9.33
49.65	10.00
10.61	3.08
13.35	3.60
14.76	3.77
17.69	4.23
19.12	4.50
23.35	5.23
24.72	5.47
26.23	5.70
27.68	5.97
29.14	6.20
30.50	6.43
31.94	6.67
33.34	6.90
34.82	7.13
36.19	7.38
37.61	7.58
39.10	7.82
40.58	8.07
42.02	8.32
43.46	8.57
46.31	9.06
49.65	9.57
52.24	9.97
40.58	8.46
42.02	8.67
43.46	8.93
46.31	9.37
49.65	9.77
50.69	10.00
52.24	10.18
56.68	10.87
58.26	11.10
61.46	11.57
62.85	11.78
64.26	12.00
65.63	12.27

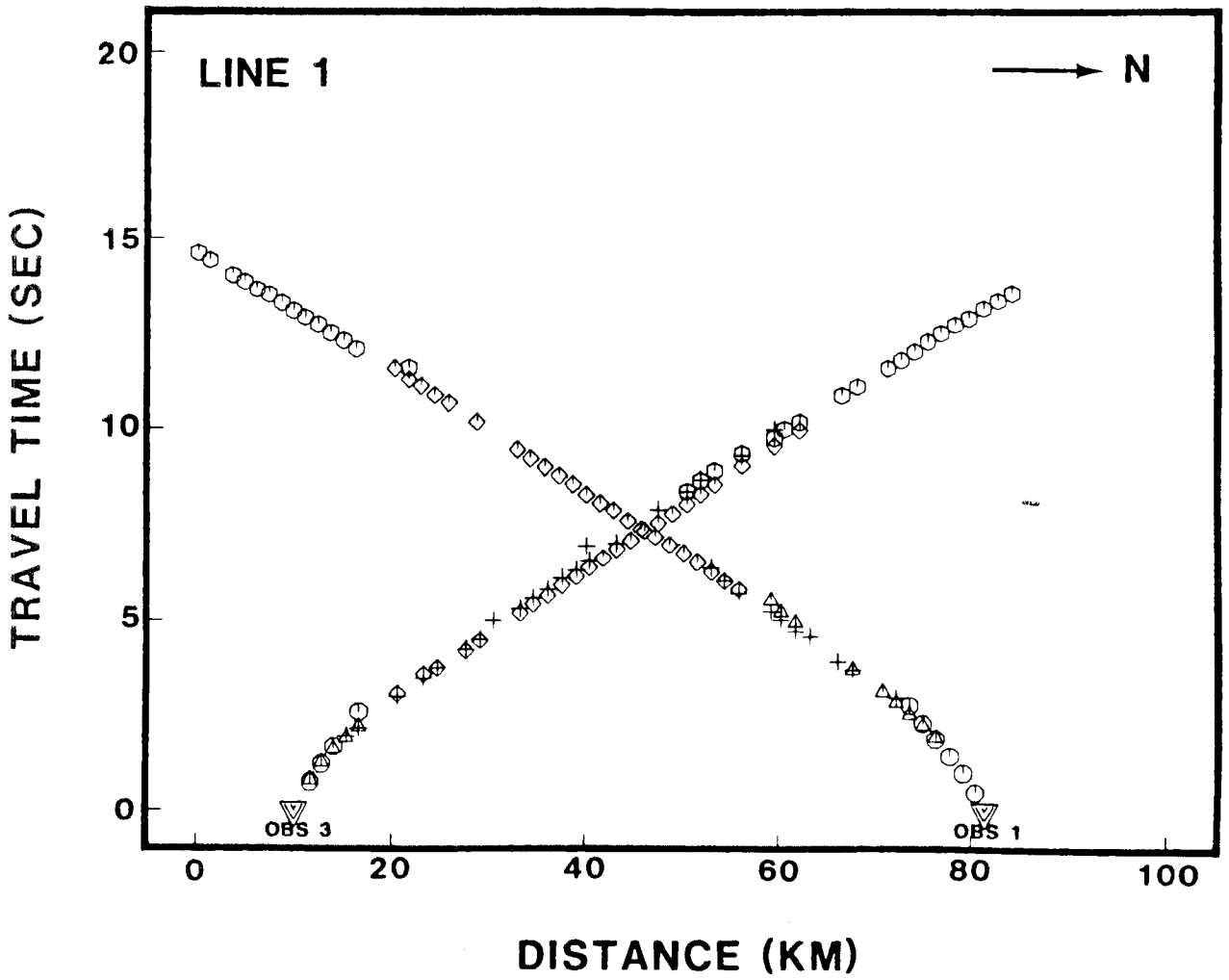

Figure C1. Composite travel time plots for Line 1 showing the picks made before bathymetric correction. Different symbols represent different straight line segments fitted using a least-squares method.

TABLE C2. Distance and time picks for Line 2.

OBS 1		OBS 2		OBS 3	
OFFSET(KM)	ARRIVAL TIME(SEC)	OFFSET(KM)	ARRIVAL TIME(SEC)	OFFSET(KM)	ARRIVAL TIME(SEC)
3.45	1.24	2.81	0.91	2.09	0.80
4.90	1.51	4.22	1.21	3.58	1.18
6.41	1.84	5.72	1.52	5.18	1.47
7.92	2.09	7.32	1.82		
9.46	2.38	8.79	2.07		
12.43	3.00	11.86	2.80		
14.23	3.29	13.27	3.07	10.05	2.56
15.65	3.56	14.82	3.31	11.65	2.89
		16.28	3.69	13.29	3.16
		17.81	3.92	14.86	3.42
				16.43	3.73
25.16	5.20			18.07	4.02
26.74	5.47				
28.33	5.69	19.33	4.22		
29.85	5.96	20.90	4.47		
31.45	6.22	22.44	4.71	18.07	4.09
32.97	6.44	23.96	5.00	19.61	4.38
34.48	6.71	25.55	5.29	21.20	4.62
36.00	7.02	27.09	5.56	22.72	4.87
37.47	7.27	28.72	5.84	24.27	5.16
38.94	7.51	30.29	6.09	25.85	5.42
		31.86	6.36	27.37	5.69
		33.51	6.62	28.89	5.96
		35.11	6.90	30.37	6.18
36.00	7.16	36.74	7.19	31.93	6.44
37.47	7.36	38.42	7.47	33.35	6.67
38.94	7.60	39.99	7.78	34.93	6.93
40.37	7.87	41.62	8.04	36.44	7.20
41.86	8.11	43.12	8.31	39.56	7.73
43.36	8.38	46.44	8.82	41.09	8.01
44.92	8.50			44.24	8.53
48.00	9.11			45.78	8.80
49.57	9.33			47.35	9.07
51.10	9.58	-1.64	0.67	50.35	9.60
52.65	9.86	-2.77	0.95	51.79	9.84
54.21	10.09	-3.95	1.12	53.25	10.04
55.72	10.33	-5.43	1.47	54.72	10.33
57.30	10.57	-8.22	1.98	56.23	10.60
60.28	11.09	-9.67	2.27	57.72	10.87
61.74	11.33	-11.16	2.58	59.23	11.11
		-12.61	2.84	60.81	11.39
				62.32	11.62
				63.90	11.93
48.00	9.96			65.46	12.13
49.57	10.18	-8.22	2.31		
51.10	10.42	-9.67	2.64		
52.65	10.64	-11.16	2.90		
54.21	10.84	-12.61	3.16	68.65	13.13
55.72	11.04	-14.11	3.44	70.23	13.36
57.30	11.33	-15.67	3.82	71.82	13.60
58.72	11.55	-17.17	3.91	74.96	14.07
60.28	11.78	-18.75	4.22	76.38	14.31
63.27	12.24	-20.31	4.49	78.19	14.47
64.79	12.44	-21.90	4.75	84.28	15.47
66.37	12.64	-23.49	5.00	85.84	15.62
69.42	13.13	-25.08	5.29	87.40	15.91
75.76	13.95	-26.67	5.56	88.96	16.09
77.33	14.20			90.53	16.36
80.57	14.60			92.08	16.60
82.20	14.84				
83.89	15.07	-21.90	6.10		
91.91	16.18	-23.49	6.20		
		-25.08	6.66		
		-26.67	6.95		
		-29.81	7.50		
		-33.05	7.90		
		-36.04	8.23		
		-37.60	8.53		
		-39.15	8.76		
		-40.72	9.04		
		-42.28	9.22		
		-43.84	9.51		
		-45.41	9.76		
		-46.96	10.04		

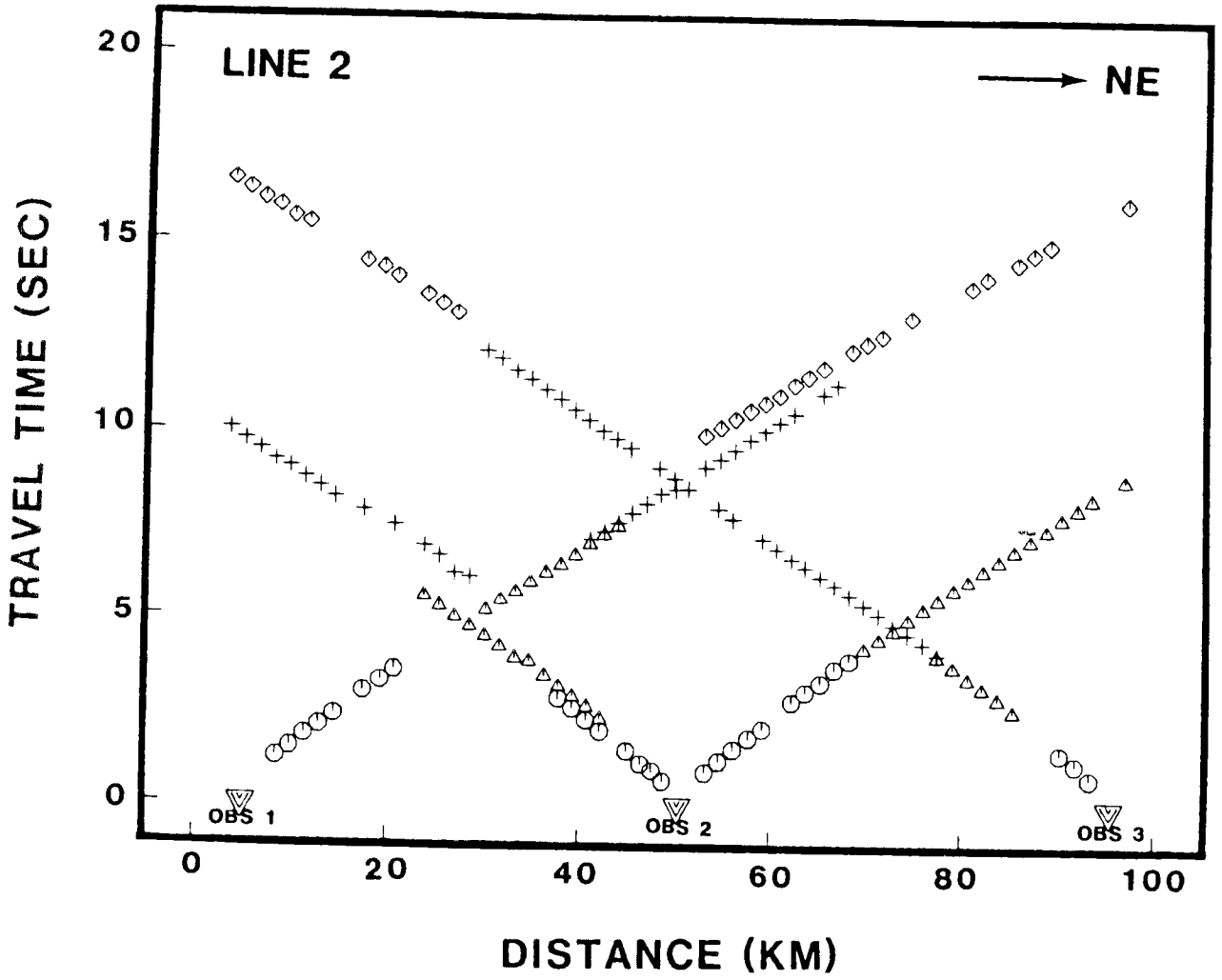

Figure C2. Composite travel time plots for Line 2 showing the picks made before bathymetric correction. Symbols are as defined in Figure C1 caption.

TABLE C3. Distance and time picks for Line 3.

OBS 1

OFFSET(KM)	ARRIVAL TIME(SEC)
17.10	4.09
18.11	4.24
19.35	4.44
20.25	4.67
21.29	4.84
22.40	5.02
23.48	5.19
24.41	5.38
25.30	5.52
26.43	5.69
27.45	5.89
28.59	6.04
29.43	6.21
30.40	6.40
31.40	6.53
33.37	6.89
34.39	7.07
35.36	7.24
36.40	7.42
37.43	7.60
38.45	7.80
40.45	8.13
41.55	8.31
42.60	8.49
43.65	8.67
44.62	8.89
45.77	9.02
46.84	9.20
48.02	9.42
49.14	9.64
50.26	9.82
51.60	10.02
52.73	10.22
54.04	10.47
55.17	10.67
56.53	10.87
57.83	11.04
58.96	11.24
60.24	11.47
61.53	11.69
62.88	11.91
64.02	12.12
65.25	12.31
66.55	12.53
67.88	12.71
66.55	12.82
67.88	12.95
69.05	13.13
70.35	13.31
71.74	13.47
72.99	13.60
74.31	13.82
75.56	13.99
76.89	14.18
79.31	14.64
80.55	14.82
81.85	15.01
83.12	15.20
84.50	15.42

OBS 3

OFFSET(KM)	ARRIVAL TIME(SEC)
1.26	0.62
2.19	0.87
3.38	1.18
4.58	1.42
5.70	1.73
6.96	2.00
8.28	2.22
8.28	2.33
9.52	2.53
10.84	2.76
12.09	3.00
13.48	3.27
14.78	3.49
15.96	3.69
17.29	3.96
18.61	4.18
19.84	4.36
22.35	4.84
23.65	5.02
24.94	5.27
22.35	4.95
23.65	5.14
24.94	5.37
26.07	5.57
27.37	5.79
29.86	6.23
31.16	6.43
32.28	6.61
33.61	6.84
35.83	7.23
37.03	7.43
40.20	8.03
31.16	6.92
32.28	7.04
33.61	7.29
34.72	7.40
35.83	7.56
37.03	7.69
38.06	7.87
39.23	8.05
40.20	8.20
41.25	8.36
42.30	8.58
43.41	8.76
44.36	8.93
45.43	9.07
46.45	9.27
47.49	9.33
48.54	9.56
50.56	9.82
53.52	10.31
54.50	10.44
55.33	10.62
56.46	10.81
57.51	10.96
58.65	11.18
59.55	11.30
60.49	11.47
61.57	11.65
62.70	11.85
63.75	12.01
64.69	12.15
66.94	12.47

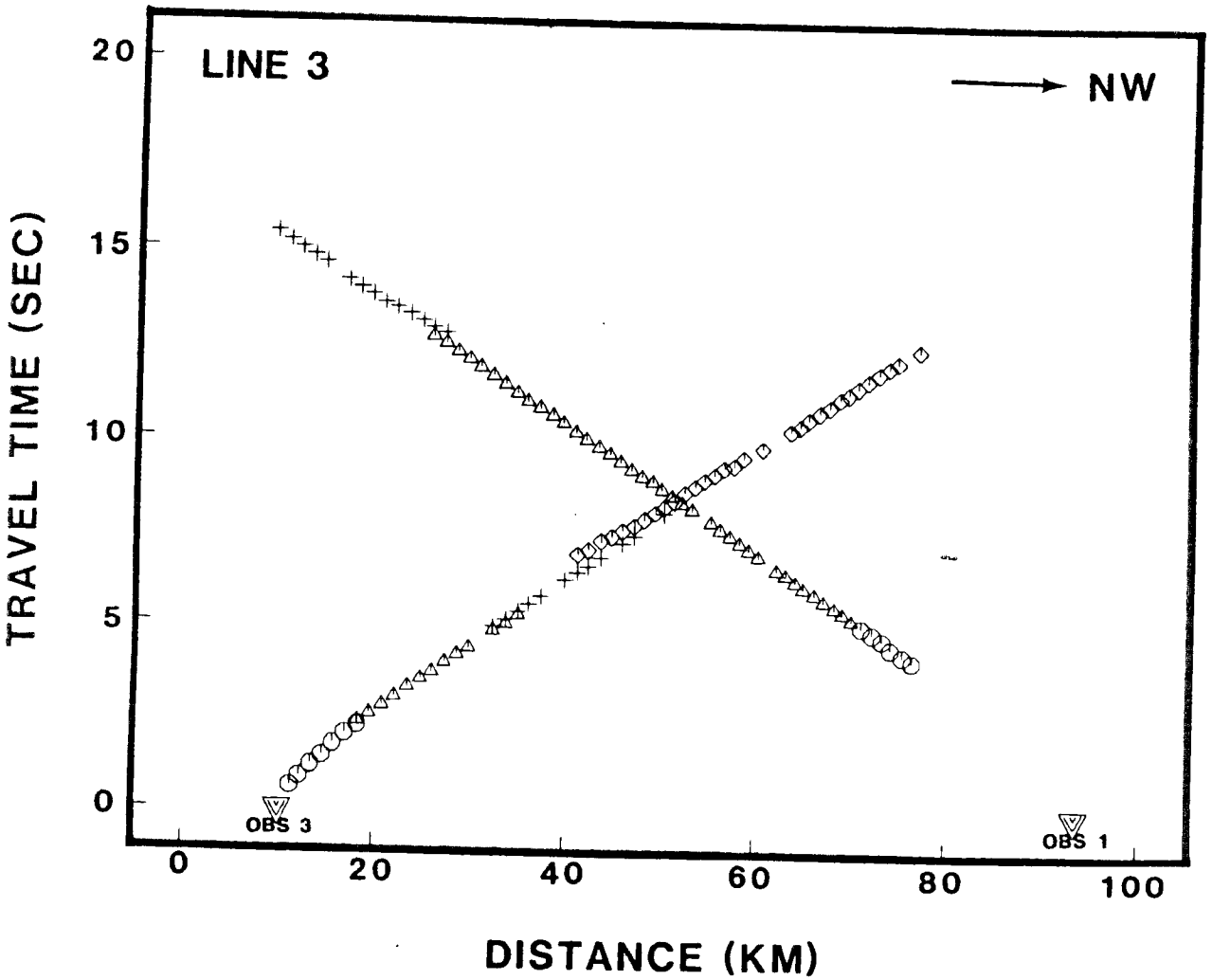

Figure C3. Composite travel time plots for Line 3 showing the picks made before bathymetric correction. Symbols are as defined in Figure C1 caption.

TABLE C4. Distance and time picks for Line 4.

OBS 1

OFFSET(KM)	ARRIVAL TIME(SEC)
1.83	0.83
2.84	1.11
4.10	1.51
5.50	1.78
6.79	2.18
8.02	2.55
9.49	2.77
9.49	2.78
10.91	3.04
12.20	3.24
13.63	3.47
15.02	3.69
16.40	3.91
17.78	4.16
19.21	4.40
20.66	4.62
22.05	4.87
23.42	5.08
24.78	5.37
26.19	5.62
29.09	6.04
30.47	6.24
31.87	6.49
33.22	6.84
34.73	7.13
36.03	7.33
37.45	7.53
38.80	7.73
40.14	8.00
42.95	8.47
44.29	8.64
52.79	10.40
54.11	10.56
55.54	10.82
56.86	11.07
58.25	11.24
59.65	11.47
61.04	11.64
62.41	11.87
63.79	12.11
66.57	12.56
67.98	12.79
70.77	13.27
72.17	13.42
76.40	14.06

OBS 2

OFFSET(KM)	ARRIVAL TIME(SEC)
1.88	0.58
2.86	0.89
3.85	1.13
5.21	1.38
6.62	1.69
9.32	2.31
14.81	3.51
16.11	3.73
17.50	3.96
18.89	4.22
20.28	4.44
21.62	4.67
23.01	4.90
24.29	5.13
25.76	5.37
27.16	5.57
28.52	5.83
29.92	6.03
31.32	6.26
32.68	6.57
34.16	6.80
35.53	7.03
-1.92	0.53
-2.72	0.84
-3.87	1.07
-5.11	1.35
-6.37	1.62
-6.37	1.71
-7.84	2.06
-9.18	2.20
-10.55	2.44
-11.92	2.71
-14.79	3.29
-16.20	3.56
-17.54	3.78
-14.79	3.43
-16.20	3.70
-17.54	3.93
-18.92	4.17
-20.30	4.40
-21.76	4.67
-23.20	4.90
-24.58	5.17
-25.98	5.37
-27.35	5.60
-28.79	5.80
-30.10	6.02
-31.53	6.42
-30.10	6.22
-31.53	6.49
-33.03	6.69
-34.32	6.91
-35.58	7.15
-37.12	7.27
-38.53	7.52
-39.93	7.78

OBS 3

OFFSET(KM)	ARRIVAL TIME(SEC)
5.29	1.90
6.36	2.15
7.62	2.41
8.94	2.67
10.19	2.95
11.48	3.18
10.19	2.81
11.48	3.05
12.88	3.13
14.18	3.53
15.54	3.77
17.00	4.00
18.26	4.25
19.58	4.45
20.94	4.70
22.30	4.93
23.65	5.17
26.32	5.60
27.73	5.83
29.03	6.03
31.81	6.47
34.55	6.96
35.96	7.16
42.85	8.53
44.20	8.76
46.90	9.24
48.40	9.56
49.76	9.82
51.15	10.20
55.41	10.71
58.18	11.27
59.55	11.56
60.93	11.82
62.93	12.11
63.83	12.44
66.60	12.93
69.42	13.23
74.94	14.19
79.15	14.84
80.55	15.00
26.32	7.27
31.81	8.12
34.55	8.37
37.40	8.90
38.75	9.16
44.20	10.17
46.20	10.47
49.76	10.90
51.15	11.13
52.52	11.35
56.82	11.92
58.18	12.17
59.55	12.37
62.93	12.87
63.83	13.17
66.60	13.60
67.98	13.78
69.42	13.93
70.72	14.20
52.52	12.73
56.82	13.23
59.55	13.65
60.93	13.87
62.93	13.93
67.98	14.67
69.42	14.90
72.15	15.33
73.66	15.50
74.94	15.70
76.20	15.90
77.74	16.05
79.15	16.25

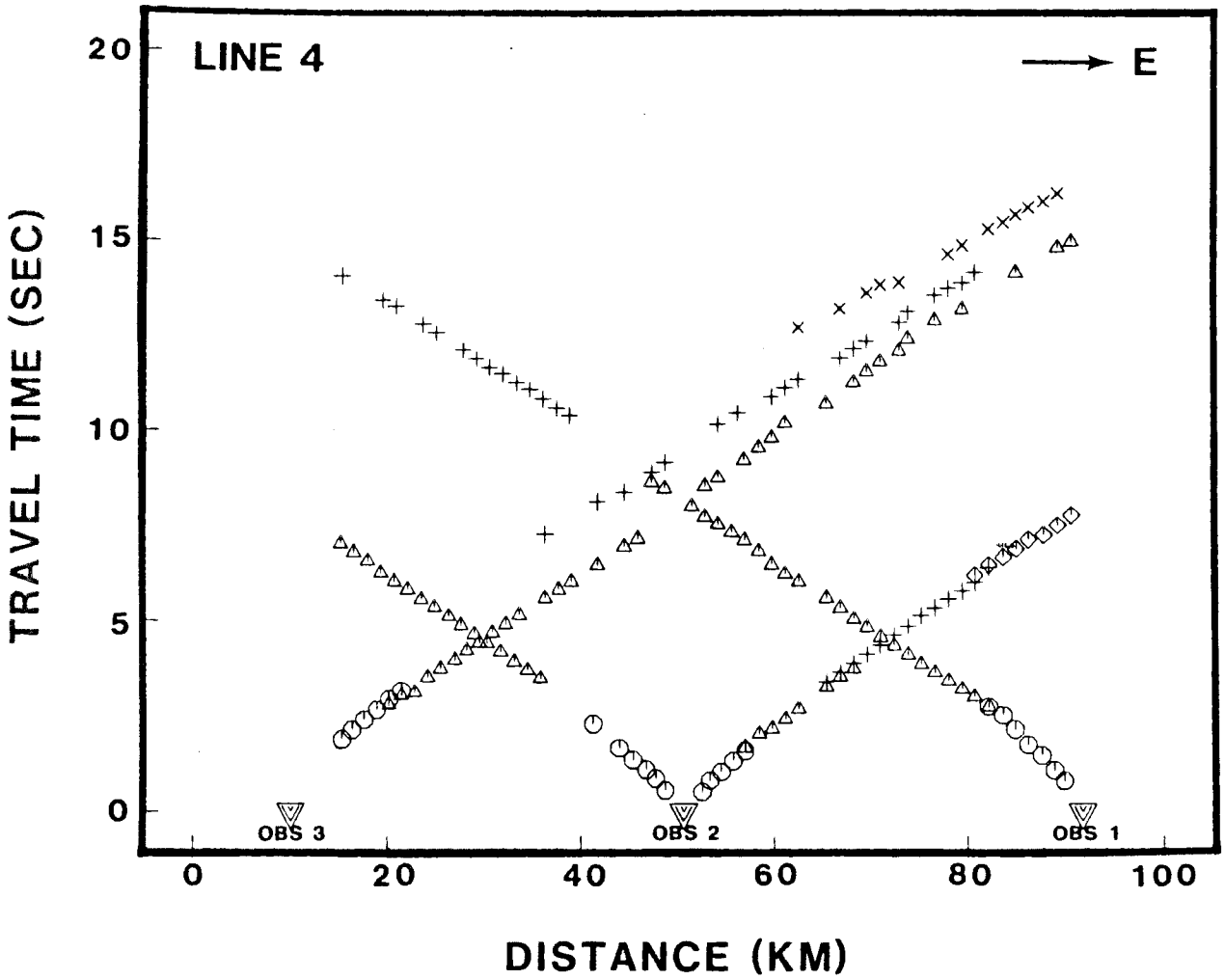

Figure C4. Composite travel time plots for Line 4 showing the picks made before bathymetric correction. Symbols are as defined in Figure C1 caption.

TABLE C5. Distance and time picks for Line 5.

OBS 1		OBS 2		OBS 3	
OFFSET(KM)	ARRIVAL TIME(SEC)	OFFSET(KM)	ARRIVAL TIME(SEC)	OFFSET(KM)	ARRIVAL TIME(SEC)
1.48	0.76	2.43	1.47	3.80	2.24
2.55	1.04	3.58	1.97	5.22	2.57
3.52	1.42	4.79	2.44	6.62	2.84
4.60	1.69			8.00	3.12
5.71	2.08				
8.01	2.89				
		4.79	2.44		
		6.07	2.72	5.22	2.62
		7.40	2.93	6.62	2.89
6.82	2.24	8.64	3.17	8.00	3.16
8.01	2.44			9.30	3.38
9.12	2.62			10.78	3.64
10.36	2.98			12.21	3.87
11.55	3.20	10.07	3.68	13.64	4.09
12.97	3.47	11.51	3.88	15.00	4.36
14.48	3.73	12.88	4.11	16.44	4.58
15.67	4.00	14.17	4.31	17.86	4.84
17.09	4.27	15.60	4.59	19.38	5.08
18.50	4.53	16.95	4.77	20.74	5.33
21.15	5.09	18.40	5.02	22.03	5.51
22.64	5.33	19.87	5.25	23.50	5.73
24.10	5.56	21.15	5.51	24.85	5.96
25.46	5.78	22.51	5.65	26.20	6.18
26.90	6.00	23.91	5.87	27.42	6.36
28.21	6.27	25.16	6.09		
		26.51	6.27		
		28.00	6.50		
25.46	5.91	29.41	6.67	19.38	5.17
26.90	6.09			20.74	5.42
28.21	6.32			22.03	5.62
29.61	6.58	30.61	6.96	23.50	5.84
31.10	6.82	31.84	7.11	24.87	6.09
32.53	7.07	32.95	7.29	26.20	6.27
33.83	7.30	34.13	7.43	27.42	6.44
36.58	7.73	35.24	7.60	28.86	6.66
37.90	7.96	36.35	7.79	30.23	6.89
39.33	8.18	37.41	7.88	31.57	7.02
40.69	8.40	38.37	8.08	32.90	7.20
42.10	8.67	39.44	8.25	35.71	7.64
43.46	8.89	40.58	8.40	37.15	7.87
		41.66	8.55	38.52	8.04
				41.27	8.53
36.58	9.22			42.64	8.71
37.90	9.44			45.41	9.02
39.33	9.67			46.77	9.22
44.83	10.45			48.16	9.47
46.28	10.67				
47.77	10.89				
49.09	11.09			68.96	14.04
59.89	12.78			70.38	14.20
61.17	13.04			71.58	14.38
62.52	13.27			72.81	14.56
64.04	13.44			73.92	14.69
65.45	13.67			75.10	14.80
66.89	13.84			76.21	15.04
68.25	14.04			77.32	15.18
71.11	14.47			78.38	15.33
72.61	14.70			79.34	15.47
73.92	14.93			80.42	15.58
75.33	15.13			82.63	15.93
76.78	15.33				
78.26	15.58				
79.68	15.80				

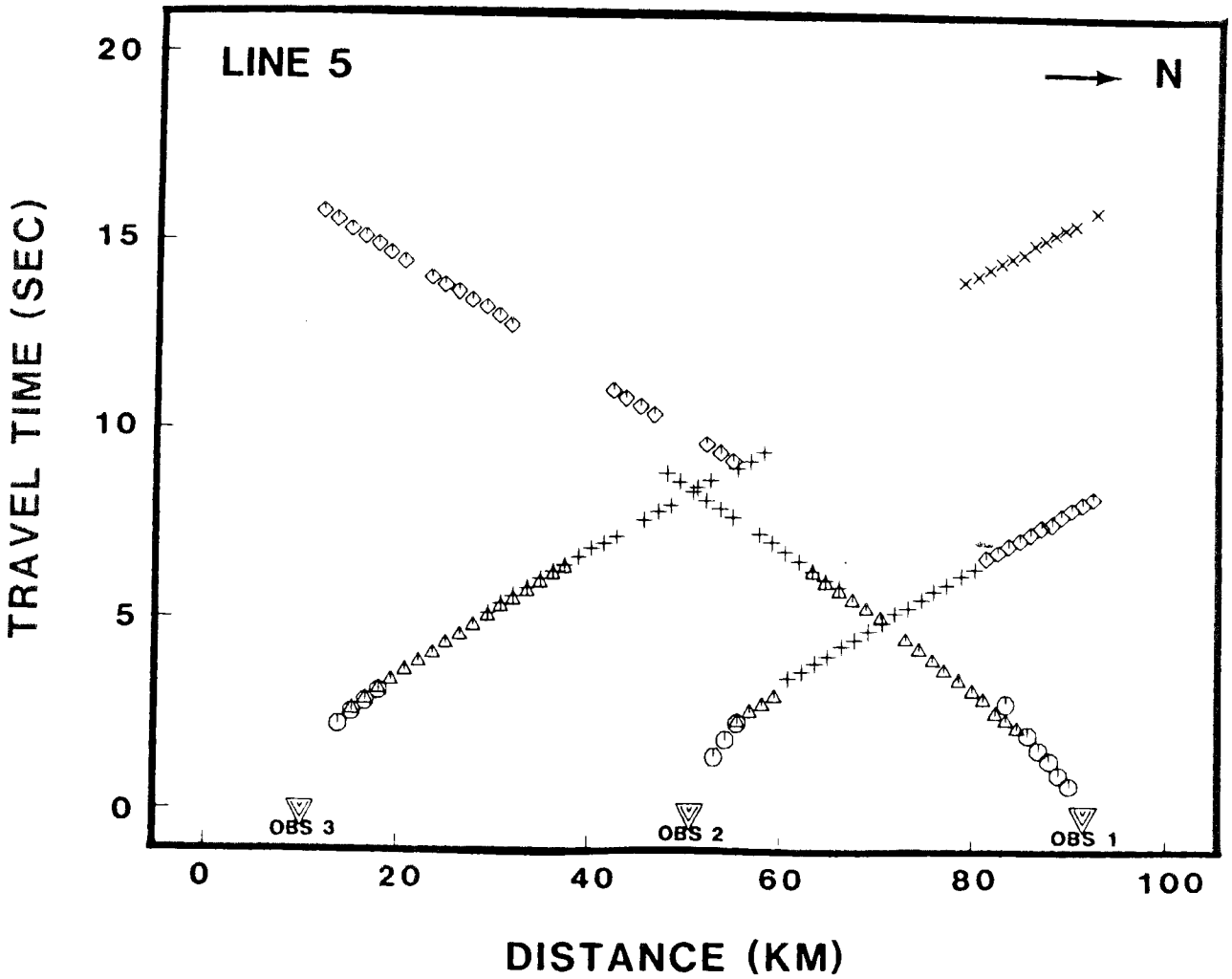

Figure C5. Composite travel time plots for Line 5 showing the picks made before bathymetric correction. Symbols are as defined in Figure C1 caption.

TABLE C6. Distance and time picks for Line 6.

OBS 1

OFFSET(KM)	ARRIVAL TIME(SEC)
5.01	3.38
6.25	3.69
7.56	3.96
8.66	4.20
9.90	4.43
12.34	4.84
13.57	5.07
14.76	5.29
15.96	5.47
17.17	5.69
18.37	5.91
19.68	6.11
22.17	6.49
23.45	6.71
24.77	6.96
26.00	7.17
27.39	7.40
24.77	7.20
26.00	7.41
27.39	7.58
28.76	7.82
30.05	8.02
31.40	8.20
32.70	8.44
33.98	8.67
35.31	8.84
36.69	9.07
38.05	9.29
39.44	9.51
51.11	13.53
52.55	13.71
53.99	13.89
55.42	14.07
56.83	14.20
58.28	14.42
59.67	14.68
61.18	14.82
64.08	15.11
65.57	15.29
67.12	15.49
68.66	15.71
70.30	15.82
71.83	16.04
73.40	16.20
74.98	16.44
78.16	16.73
79.74	16.92
81.24	17.15
82.76	17.31
84.21	17.53

OBS 2

OFFSET(KM)	ARRIVAL TIME(SEC)
4.49	3.16
5.61	3.38
6.79	3.64
8.03	3.93
9.27	4.16
10.48	4.44
11.73	4.67
13.04	4.93
14.30	5.16
15.66	5.38
17.06	5.61
15.66	5.47
17.06	5.69
18.29	5.89
19.60	6.13
20.88	6.31
22.12	6.53
23.30	6.71
24.58	6.93
25.75	7.13
26.92	7.33
28.09	7.51
29.25	7.82
30.46	8.04
31.78	8.22
32.89	8.44
34.13	8.67
26.92	7.62
28.09	7.78
30.46	8.22
31.78	8.40
32.89	8.58
34.13	8.77
35.23	8.93
36.56	9.11
37.85	9.29
39.08	9.47
40.40	9.68
41.71	9.91

OBS 3

OFFSET(KM)	ARRIVAL TIME(SEC)
1.47	1.90
2.99	2.53
4.49	3.22
6.07	3.62
9.26	4.32
10.84	4.59
12.42	4.91
13.95	5.24
15.60	5.53
17.13	5.85
18.67	6.18
20.16	6.44
21.72	6.71
23.05	6.98
24.56	7.24
25.96	7.51
27.41	7.78
30.27	8.60
31.73	8.80
33.18	9.07
34.69	9.24
36.15	9.47
37.67	9.69
39.09	9.93
40.48	10.18
41.97	10.37
43.49	10.58
44.89	10.84
46.28	11.04
47.64	11.29
49.02	11.47
50.34	11.67
51.61	11.87
52.91	12.09
54.26	12.27
55.55	12.49
56.92	12.67
58.33	12.91
59.57	13.09
59.57	13.89
60.89	14.07
62.18	14.22
63.44	14.36
64.64	14.55
65.94	14.71
67.13	14.84
68.32	15.00
69.50	15.16
70.68	15.30
71.90	15.47
73.22	15.64
74.33	15.83
75.58	15.96
76.68	16.13
79.28	16.47
80.50	16.62
81.81	16.78
83.13	16.96

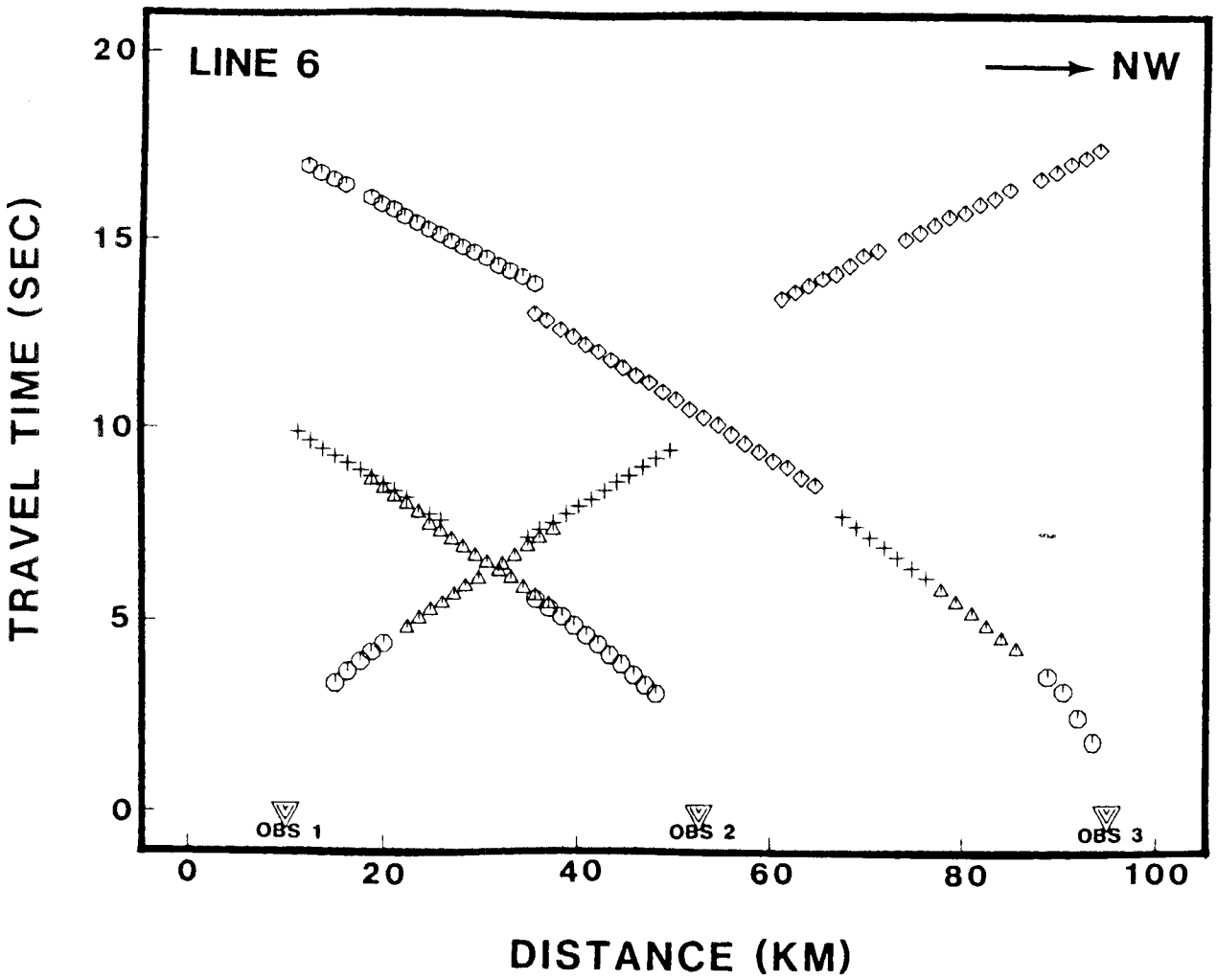

Figure C6. Composite travel time plots for Line 6 showing the picks made before bathymetric correction. Symbols are as defined in Figure C1 caption.

APPENDIX D

Interpreted Velocity-depth Profiles

Line 1 82

Line 2 83

Line 3 84

Line 4 85

Line 5 86

Line 6 87

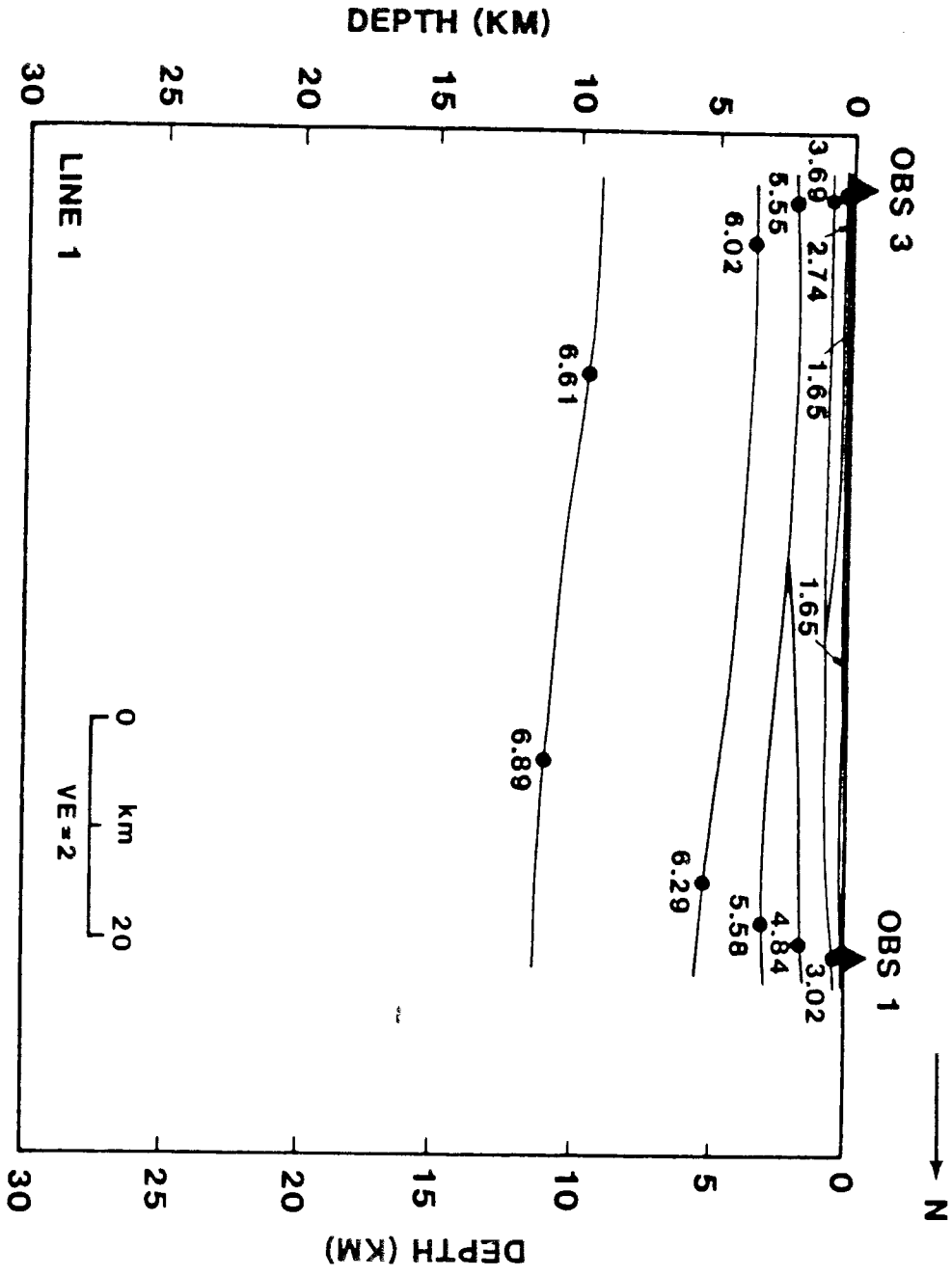

Figure D1. Interpreted layer model for Line 1 using the results from Figure 7.

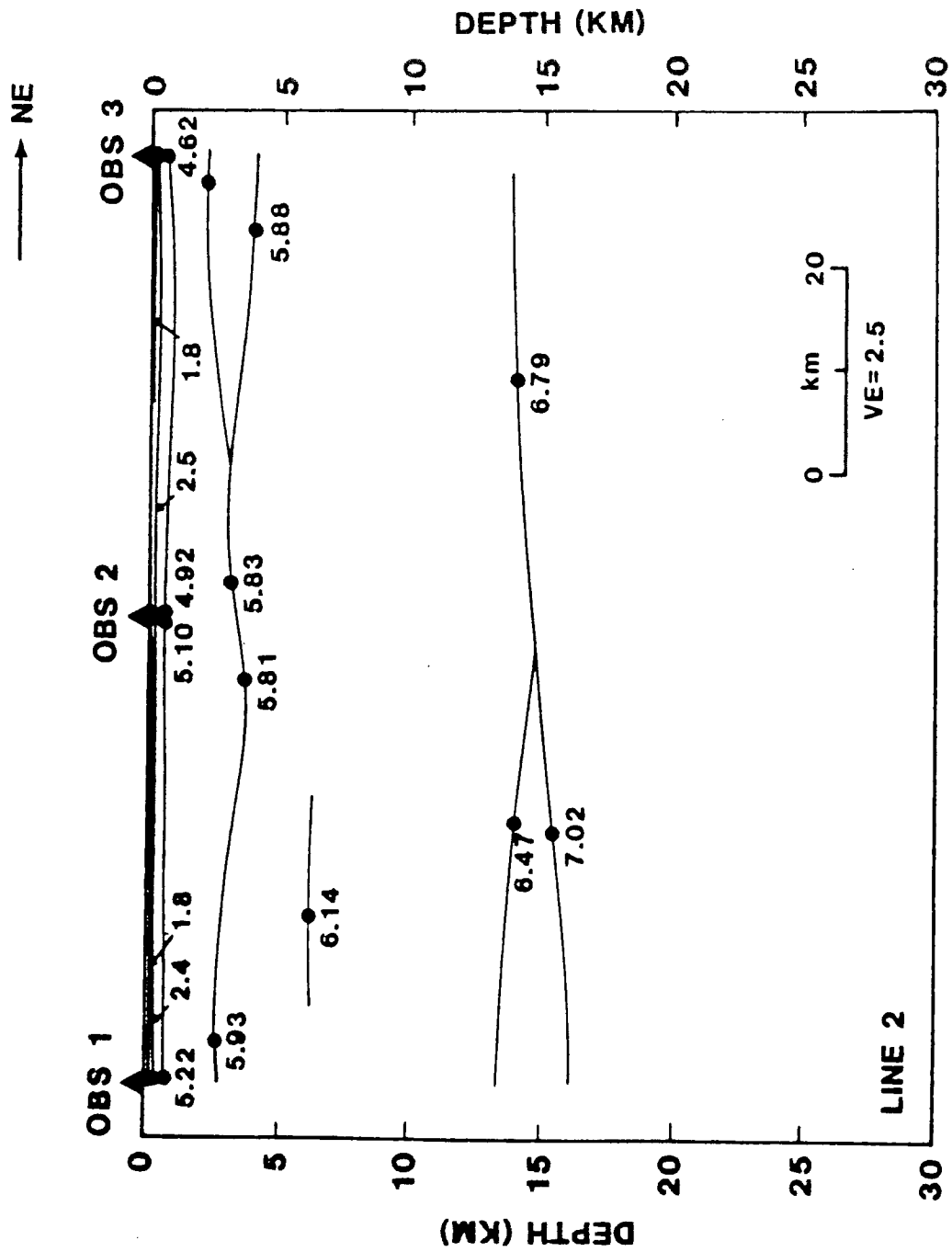

Figure D2. Interpreted layer model for Line 2 using the results from Figure 8.

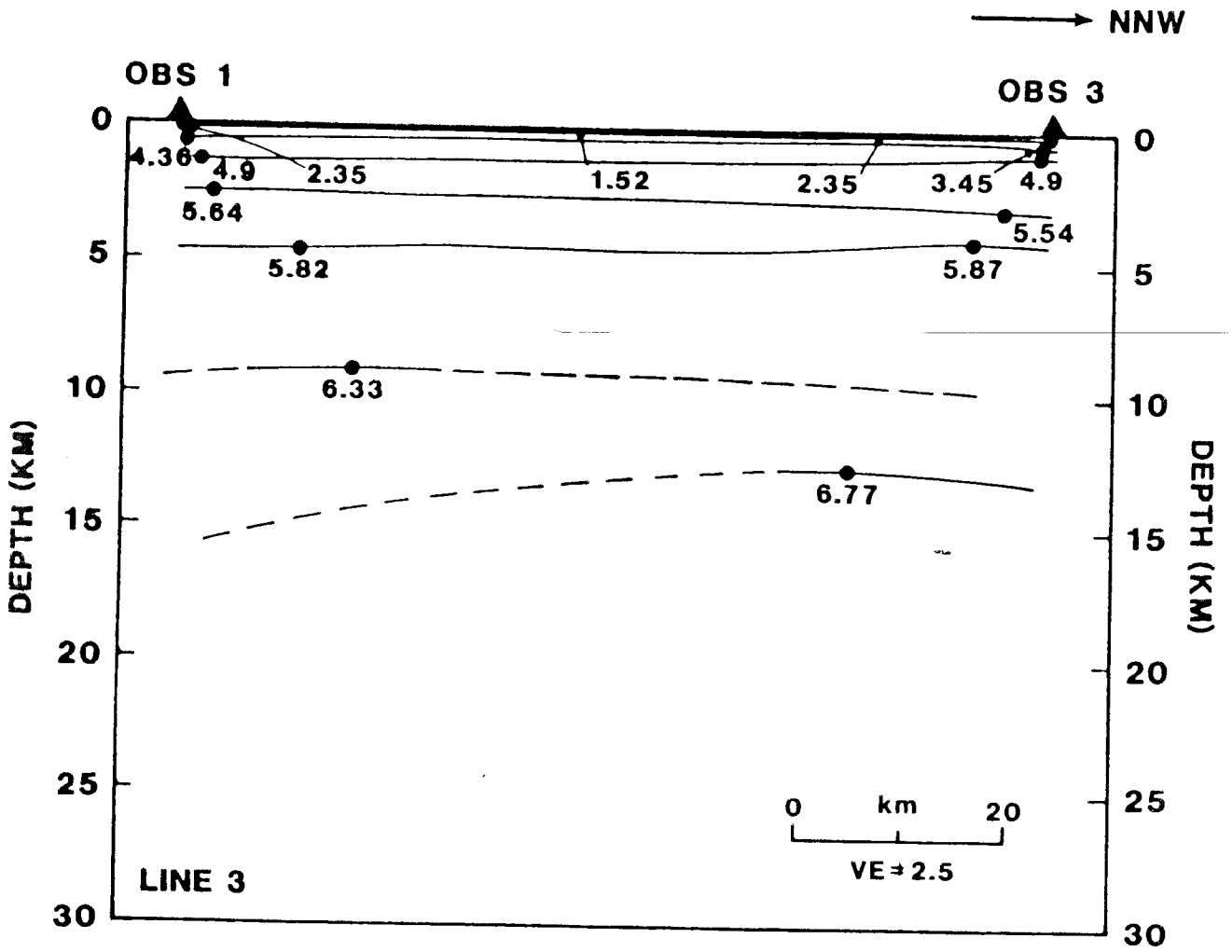

Figure D3. Interpreted layer model for Line 3 using the results from Figure 9.

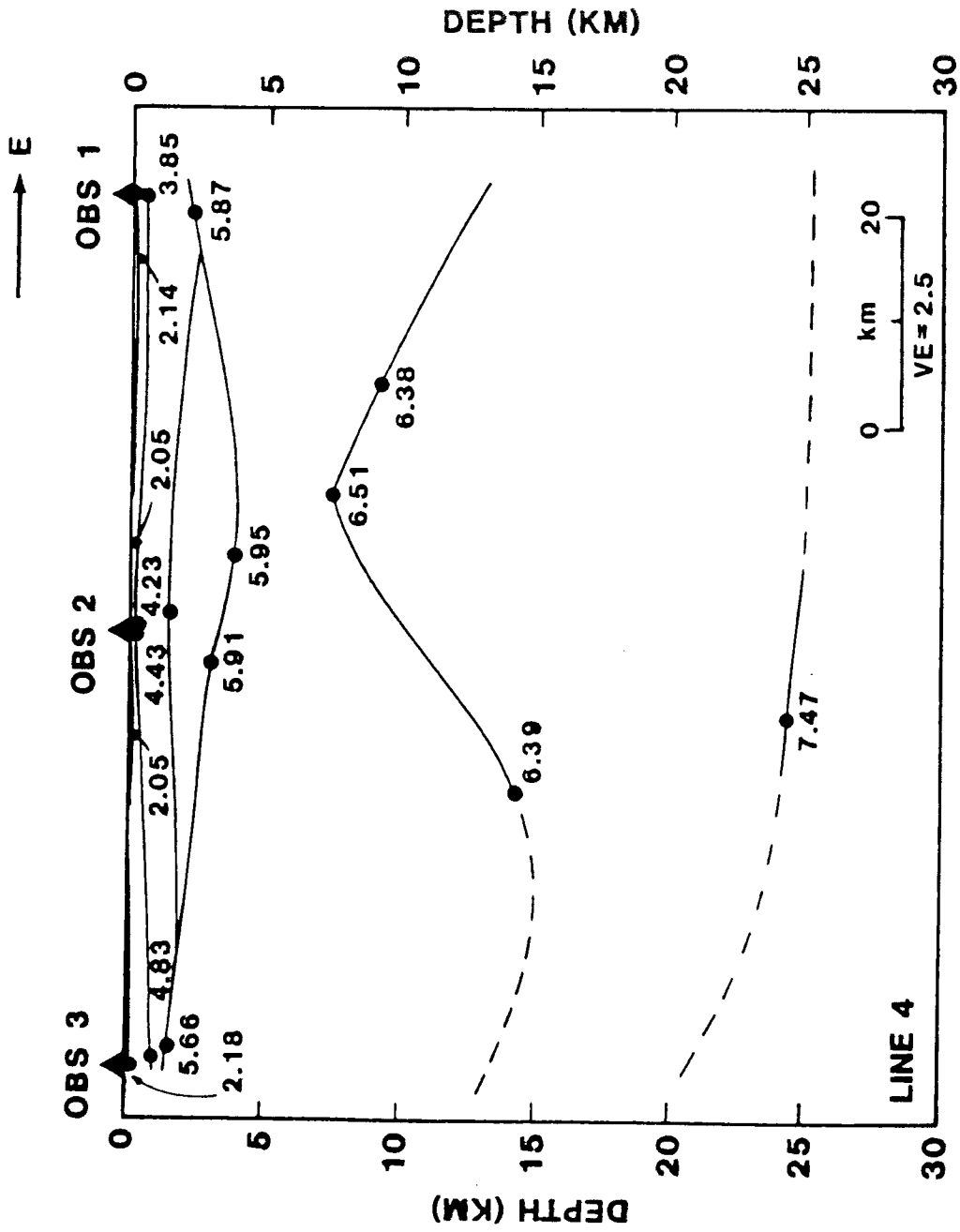

Figure D4. Interpreted layer model for Line 4 using the results from Figure 10.

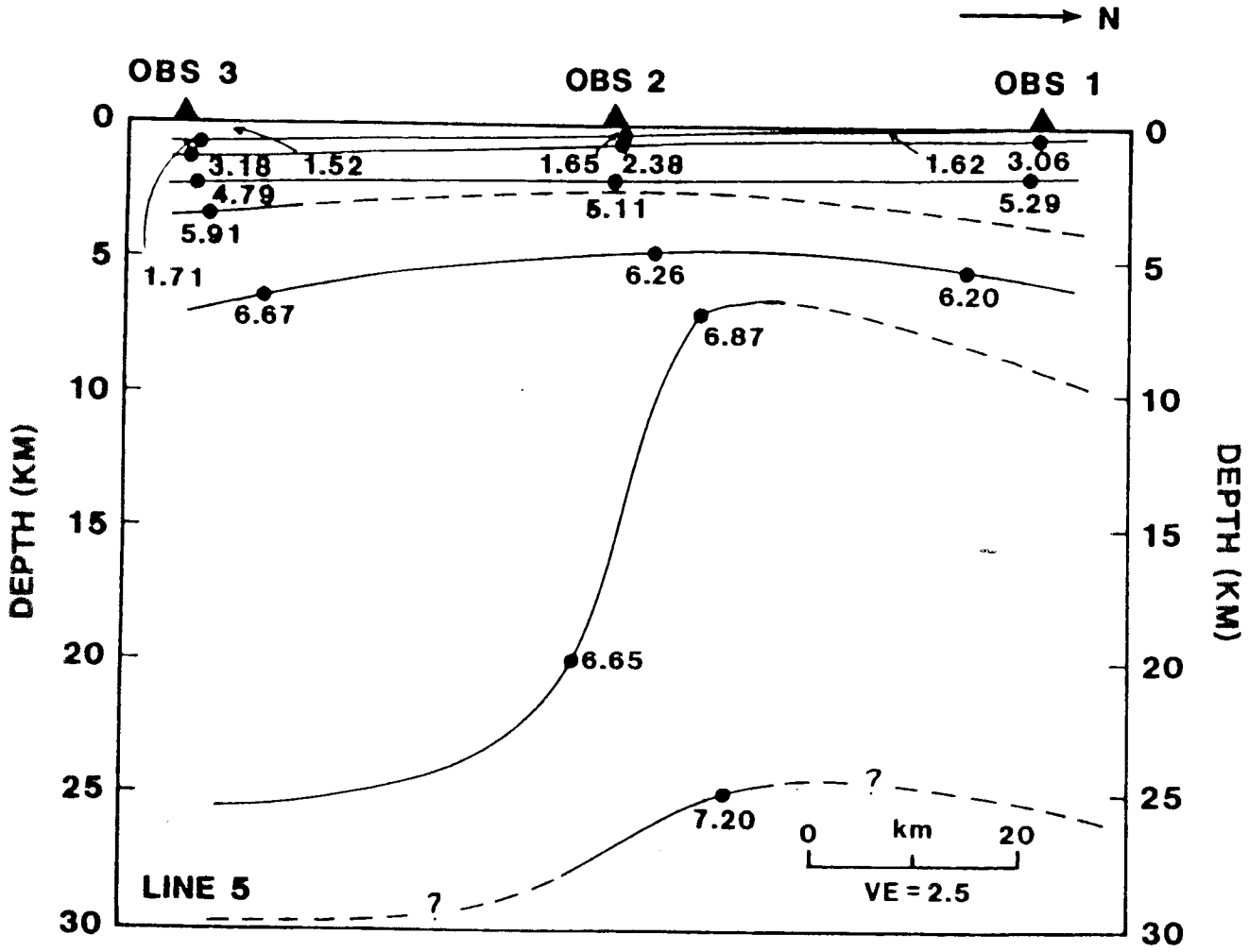

Figure D5. Interpreted layer model for Line 5 using the results from Figure 11.

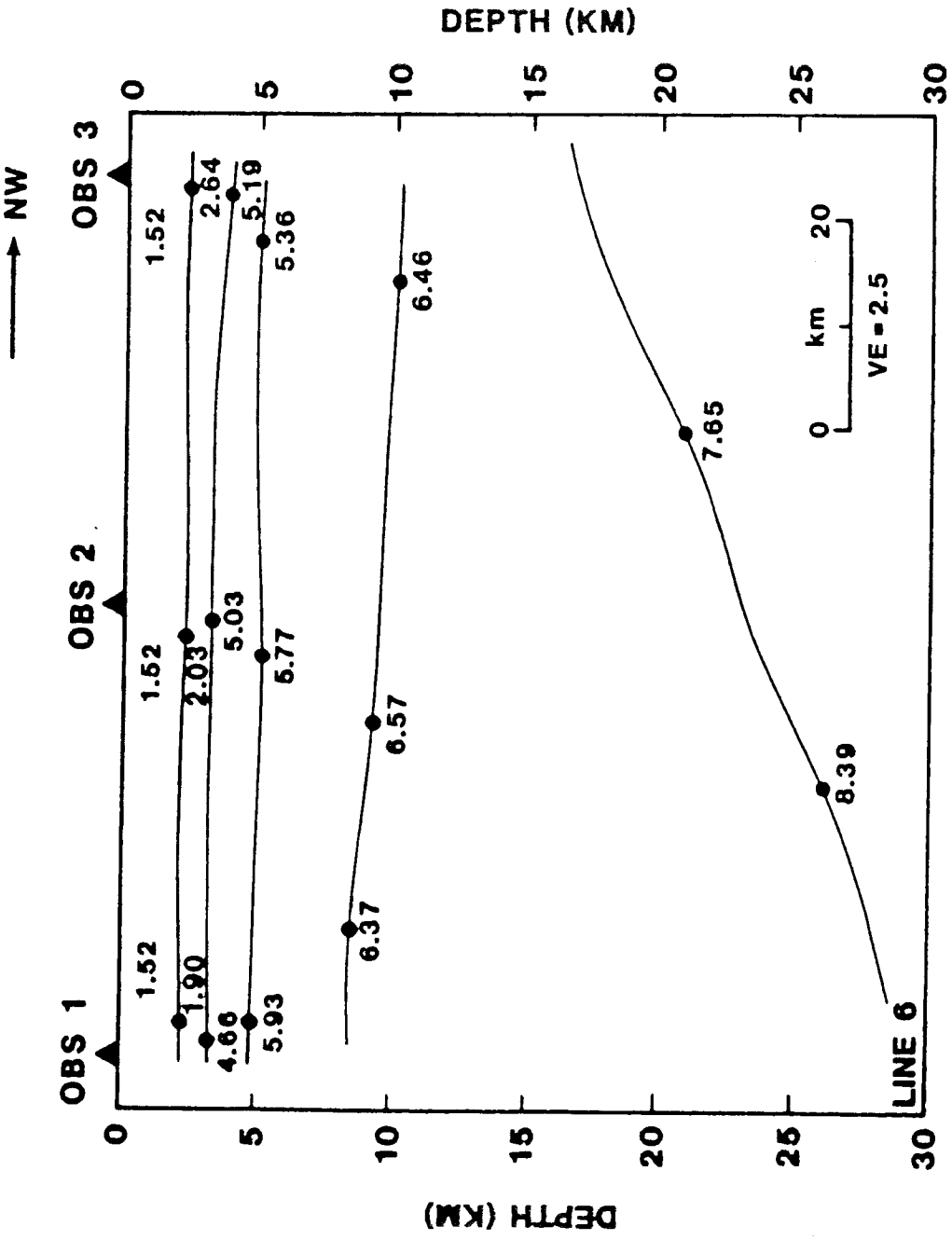

Figure D6. Interpreted layer model for Line 6 using the results from Figure 12.